Gold and Silver Nanolenses Self-Assembled by DNA Origami

Dissertation
zur Erlangung des akademischen Grades
Doctor rerum naturalium (Dr. rer. nat.)

vorgelegt der Mathematisch-Naturwissenschaftlichen
Fakultät der Universität Potsdam

von

Christian Heck

Eingereicht am 28. November 2017

Published online at the
Institutional Repository of the University of Potsdam:
URN urn:nbn:de:kobv:517-opus4-409002
http://nbn-resolving.de/urn:nbn:de:kobv:517-opus4-409002

Diese Arbeit ist vom Oktober 2013 bis November 2017 als kooperatives Projekt an der Universität Potsdam, der Bundesanstalt für Materialforschung und -prüfung und der Humboldt Universität zu Berlin im Rahmen der Graduiertenschule School of Analytical Sciences Adlershof entstanden.

Gutachter: JProf. Dr. Ilko Bald
Prof. Dr. Janina Kneipp
Prof. Dr. Ralf Seidel

Abstract

Nanolenses are linear chains of differently-sized metal nanoparticles, which can theoretically provide extremely high field enhancements. The complex structure renders their synthesis challenging and has hampered closer analyses so far. Here, the technique of DNA origami was used to self-assemble DNA-coated 10 nm, 20 nm, and 60 nm gold or silver nanoparticles into gold or silver nanolenses. Three different geometrical arrangements of gold nanolenses were assembled, and for each of the three, sets of single gold nanolenses were investigated in detail by atomic force microscopy, scanning electron microscopy, dark-field scattering and Raman spectroscopy. The surface-enhanced Raman scattering (SERS) capabilities of the single nanolenses were assessed by labelling the 10 nm gold nanoparticle selectively with dye molecules. The experimental data was complemented by finite-difference time-domain simulations. For those gold nanolenses which showed the strongest field enhancement, SERS signals from the two different internal gaps were compared by selectively placing probe dyes on the 20 nm or 60 nm gold particles. The highest enhancement was found for the gap between the 20 nm and 10 nm nanoparticle, which is indicative of a cascaded field enhancement. The protein streptavidin was labelled with alkyne groups and served as a biological model analyte, bound between the 20 nm and 10 nm particle of silver nanolenses. Thereby, a SERS signal from a single streptavidin could be detected. Background peaks observed in SERS measurements on single silver nanolenses could be attributed to amorphous carbon. It was shown that the amorphous carbon is generated *in situ*.

Zusammenfassung

Nanolinsen sind Strukturen aus linear angeordneten, unterschiedlich großen metallischen Nanopartikeln. Elektromagnetische Felder können durch sie theoretisch extrem verstärkt werden, aufgrund ihres komplexen Aufbaus sind sie bislang aber wenig erforscht. Im Rahmen dieser Dissertation wurden Nanolinsen mit Hilfe der DNA-Origami-Technik aus DNA-beschichteten 10 nm-, 20 nm- und 60 nm-Gold- oder Silbernanopartikeln hergestellt. Für Goldnanolinsen sind die Partikel dabei in drei unterschiedlichen Geometrien angeordnet worden. Einzelne Goldnanolinsen wurden mittels Rasterkraftmikroskopie, Rasterelektronenmikroskopie, Dunkelfeld- und Ramanspektroskopie untersucht. Um die Raman-Verstärkung quantifizieren zu können, trugen dabei jeweils die 10 nm-Goldpartikel Farbstoffmoleküle in ihrer Beschichtung. Die Interpretation der Messdaten wurde durch numerische Simulationen unterstützt. Nanolinsen zeichnen sich durch eine stufenweise Feldverstärkung aus. Dieser Effekt konnte experimentell bestätigt werden, indem selektiv die 20 nm- oder 60 nm-Partikel von Goldnanolinsen mit Farbstoffen markiert und die resultierenden Raman-Signale verglichen wurden. Ein mit Alkingruppen markiertes Protein ist ortsselektiv in Silbernanolinsen integriert worden. Es war möglich, das für das Alkin charakteristische oberflächenverstärkte Raman-Signal im Spektrum einer einzelnen Nanolinse und damit eines einzelnen Proteins zu beobachten. Bei den Messungen mit Silbernanolinsen sind für amorphe Kohlenstoffspezies charakterstische Hintergrundsignale beobachtet worden. Durch zeitabhängige Messungen konnte gezeigt werden, dass diese Spezies erst *in situ* gebildet werden.

Contents

Abbreviations and constants

AFM	atomic force microscopy
bp	base pairs
BSPP	bis(p-sulfonatophenyl)phenylphosphine
c	speed of light (2.998×10^{8} m s^{-1})
DNA	deoxyribonucleic acid
DTPA	dithiol-phosphoramidite
ε_0	permittivity of vacuum (8.854×10^{-12} F m^{-1})
EDTA	ethylenediaminetetraacetic acid
EMCCD	electron multiplying charge-coupled device
FDTD	finite-difference time-domain
h	Planck constant (6.626×10^{-34} J s)
kb	kilobases
LOESS	locally weighted scatterplot smoothing
LSP	localised surface plasmon
MALDI-TOF MS	matrix-assisted laser desorption/ionisation - time-of-flight mass spectrometry
MWCO	molecular weight cut-off
nt	nucleotides
P-NHS	propargyl-N-hydroxysuccinimidyl ester
SDS	sodium dodecyl sulfate
SEM	scanning electron microscopy
SERS	surface-enhanced Raman scattering
SERRS	surface-enhanced resonance Raman scattering
TAE	Tris-acetate-EDTA
TAMRA	5-carboxytetramethylrhodamine
TCEP	tris(2-carboxyethyl)phosphine
TO	transverse optical phonon
Tris	tris(hydroxymethyl)aminomethane
UV-Vis	ultraviolet - visible

Vectorial quantities will be represented in bold notation.

1. Introduction

Almost sixty years after Richard Feynman's often-quoted lecture about 'plenty of room at the bottom',[1] nanotechnology has become part of our everyday life. Electronic devices are built from nanoscale features, like transistors, that have now reached sizes as small as 5 nm.[2] Apart from such miniaturisation of existing technology, a lot of the attention nanoscale research has gained is due to new material properties that arise at the nanoscale. With feature sizes between 1 nm and 100 nm, nanomaterials are in a border region between bulk and atomic scale, and this hybrid nature enables properties that can be found in neither of the two. Often these new properties are size-dependent, like the tunable colour of semiconductor nanoparticles due to the quantum confinement effect,[4] which is already applied in new generation displays to improve colour depth.[5] The peculiar optical properties of *metal* nanoparticles have been used for centuries—in the form of colourants for glasses in church windows, or in the famous Roman Lycurgus cup (shown in Figure 1.1).[6] These optical properties arise from the spatial confinement of the surface-conducting electrons in the metal nanostructures. The collective oscillation of such electrons upon illumination is called a 'plasmon'. Today's applications reach far beyond a simple colouring of glasses. Plasmon-supporting nanostructures can guide light at scales much smaller than the diffraction limit,[7] nanoscale thin films can act as optical lenses,[8] and films with nanoscale holes can show extraordinarily high optical transmission.[9] Apart from such applications as strictly optical new materials, plasmon-driven (photo-)chemistry is a prodigious candidate for green chemistry.[10]

Figure 1.1.: The Lycurgus Cup, manufactured in the 4th century. Its red colour upon transmission and green colour upon reflection of light stem from nanoparticle colourants.[3]

One of the most remarkable features of plasmonic nanostructures is their ability to focus light in subwavelength-sized volumes.[11] The electric field is amplified in such foci and the high local fields can be exploited for the enhancement of signals in infrared,[12] fluorescence,[13] and Raman spectroscopy.[14–16] An especially close relationship exists between the development of plasmonic nanostructures and the latter, surface-enhanced Raman scattering (SERS). Both fields have co-evolved and mutually spurred new research interest.[17] Raman spectroscopy, with the complex vibrational data it provides, is a versatile analytical technique, yet it suffers from low sensitivity. SERS can increase the signal intensity to such a tremendous degree that even single-molecule Raman spectroscopy is possible.[18,19] The underlying electromagnetic field enhancement strongly depends on the shape of the plasmonic nanostructures that provide it. In general, two synthetic routes to nanostructures can be discriminated:

top-down Larger structures are processed, often etched, to create nanofeatures. Example: photolithography.[20]

bottom-up Nanostructures are assembled from smaller constituents. Example: Turkevich method for gold nanoparticle synthesis.[21]

The first single-molecule SERS studies used random aggregates of silver nanoparticles, leaving the formation of highly enhancing structures to chance.[18,19] In search for plasmonic nanostructures that provide high field enhancement in a more reproducible manner, both, top-down and bottom-up approaches have been used extensively to create a plethora of different plasmonic nanostructures.[22] Non-spherical nanoparticles like nanorods,[23] nanostars,[24] nanoflowers[25] or nanoprisms[26] were synthesised, dimers selectively assembled,[27] and surfaces regularly patterned with triangular features,[28] just to name a few. In 2003, a plasmonic nanostructure was proposed that consists of a linear chain of differently-sized particles and which was termed 'nanolens'.[29] Nanolenses have a self-similar, incremental architecture, for which a cascaded enhancement of the electromagnetic field was predicted that can potentially outperform other plasmonic structures. A more detailed introduction to the plasmonics of nanolenses will be given in Section 1.1.3; a schematic gold nanolens is displayed in Figure 1.2. In this thesis, the term nanolenses refers to structures with at least three differently-sized particles. In addition to the high

field enhancements, nanolenses are predicted to be efficient generators of second harmonic local fields,[30,31] and to effectively support surface plasmon amplification by stimulated emission (spaser).[32] A number of theoretical studies on nanolenses followed: The cascading effect was investigated for particle dimers[33,34] and the statistics of enhancement distributions in nanolenses were simulated.[35] Whereas the initial nanolenses were constituted from spherical particles, a cascaded enhancement was also predicted for self-similar chains of core-shell nanoparticles,[36] nanorods[37] and nanocrescents.[38] Upon publication, the efficiency of the cascade enhancement in nanolenses was controversially discussed,[39,40] but in a follow-up work, the initial authors could support their findings by including electrodynamics in the simulations.[41] Nanolenses are exciting plasmonic structures, but their complex shape so far hampered practical investigations. Only a moderate number of studies have examined the plasmonic properties of real nanolenses so far. These studies either suffered from limited control over particle arrangement and stoichiometry,[42] employed laborious top-down methods with large and rather flat features[43–48] or even built up single nanolenses particle by particle with a scanning near-field optical microscopy tip.[49] Recently, an electrostatic surface-assembly of spherical particles was presented that yields many well-defined nanolenses, yet this protocol has considerable inherent limitations and is restricted in its range of particle sizes.[50] In order to yield many structures at the same time, a bottom-up, self-assembly synthesis of nanolenses would be desirable. Yet, their structural complexity entails several parameters that have to be controlled: at least three particle types and relative positions. This set of spacial and qualitative information has to be encoded within the self-assembling system. DNA is an ideal material for this, as it can act as both, medium and read-out of structural information. This double-nature is at the foot of structural DNA nanotechnology.[51] It renders DNA a unique tool for self-assembling synthetic nanostructures with unmatched complexity. By hybridising complementary segments, DNA strands can fold into almost arbitrary three-dimensional shapes; non-DNA components can be integrated when they are linked to DNA strands.[52] One of the most popular tech-

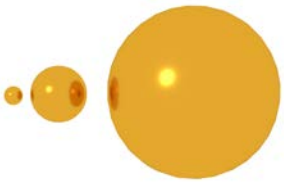

Figure 1.2.: Schematic nanolens consisting of three gold nanoparticles. It is self-similar in the sense that particle diameters and gaps decrease at a fixed ratio.

niques in the field is *DNA origami*, where scaffolds of about 100 nm in size are formed from one long DNA single strand and a set of about 200 short DNA single strands.[53] Thanks to their wide use in molecular biology, the required synthetic DNA strands are readily commercially available, as well as strands with a great variety of chemical modifications. In a typical synthesis, billions of DNA nanostructures are easily self-assembled in parallel.[54] Bidault *et al.* were the first to assemble nanolenses with the help of DNA. They did so by attaching one or two DNA single strands to gold nanoparticles of different sizes and hybridising them, respectively.[55] Thereby the particle stoichiometry was controlled, but the angle between the particles was left to chance because there was no control over where on the particle surface the DNA strands would attach. The advantage of this approach is that particles have no further DNA coating that would limit plasmon interaction or give signals that can interfere with those from potential analytes in spectroscopic applications. Only small particles ($\leq$ 18 nm) were used, as larger particles would not have been stable under these conditions.[56] After pursuing a similar approach on stiff DNA motifs,[57] Ding *et al.* immobilised a chain of six gold nanoparticles of three different sizes in a collinear fashion on DNA origami scaffolds.[58] Being an impressive proof-of-principle study, the applied DNA-coated gold nanoparticles were too small ($\leq$ 15 nm) and the interparticle gaps too large ($\approx$ 8 nm) to allow an efficient plasmon interaction. The extension of this work to an efficient nanolens is not trivial since larger metal nanoparticles are not as stable and easily aggregate in the high-ionic strength buffers that are used for DNA origami. This necessitates the development of new, more-efficient DNA coating procedures. Also, with decreasing interparticle gaps, steric confinement and electrostatic repulsion start to hinder the assembly.

In this thesis, optimised nanoparticle coating protocols and adjusted DNA origami scaffold designs are presented. They enable the assembly of nanolenses that indeed show the characteristic cascaded electromagnetic field enhancement and provide strong local fields. The DNA origami scaffold allows a free placement of the constituent metal nanoparticles, with a precision of ca. 5 nm (spacing between available attachment points). Leveraging this, 10 nm, 20 nm and 60 nm gold nanoparticles are assembled in three different geometric configurations to form gold nanolenses; silver nanolenses are prepared in one configuration. See Figure 1.3 for a schematic overview. Small structural variations can strongly influence the plasmonic properties

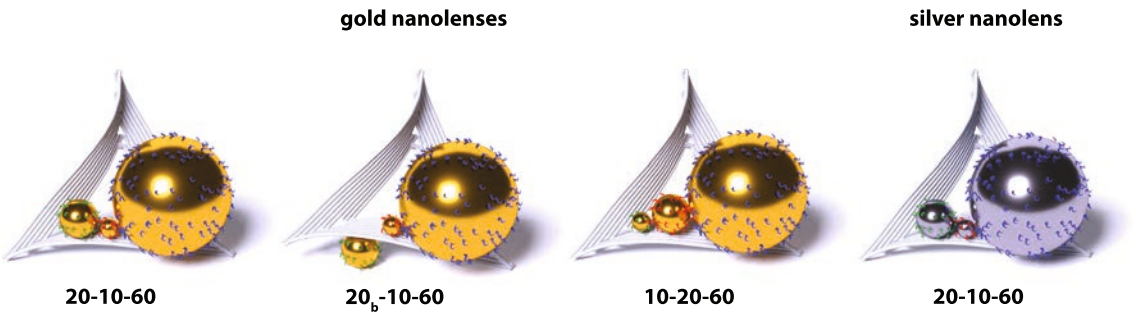

Figure 1.3.: Schematic illustrations of the assembled nanolenses. The numbers below give the diameters of the constituent nanoparticles in nm. The DNA origami scaffold is shown in grey.

of nanoparticle aggregates. These differences between individual plasmonic structures are missed out in ensemble measurements. For that reason, here, mostly single nanolenses are analysed. The three different gold nanolens designs are compared by atomic force microscopy (AFM), scanning electron microscopy (SEM), dark-field scattering and Raman spectroscopy. The silver nanolenses are characterised by AFM and Raman spectroscopy. DNA origami also enables a spatially-resolved characterisation of the assembled structures: Probe molecules can be selectively placed on certain particles, or on a position of choice on the DNA origami scaffold itself. In order to compare the Raman enhancement provided by the different gold nanolens designs, their respective 10 nm gold nanoparticles are labelled with a dye. The average numbers of dye molecules per particle can be determined by fluorescence spectroscopy. For the 20-10-60 gold nanolenses, the cascaded field enhancement is investigated by selectively labelling the 20 nm or 60 nm particles with Raman probes and comparing the SERS intensities of respective sets of single gold nanolenses. For the silver nanolenses, a single protein is immobilised on the DNA origami scaffold, between the 20 nm and 10 nm particle, and functions as a biological model analyte. This combination of controlled synthesis and probing enables an in-depth investigation on the plasmonic nanostructures. Yet, the DNA origami-based approach comes with its own inherent limitations, which to investigate will be also part of this thesis. It follows an introduction to the fundamental backgrounds of the presented work.

1.1. Plasmonics

The dielectric function $\varepsilon(\nu)$ describes the response of a medium to electromagnetic radiation of frequency ν. The value of $\varepsilon(\nu)$ at a defined ν is a complex number and referred to as dielectric constant ε. The dielectric function is linked to the index of refraction $n(\nu)$ by $n(\nu) = \sqrt{\varepsilon(\nu)}$. In this work, the *relative* dielectric function and constant are used. They can be transformed into the respective *absolute* quantities by multiplication with the permittivity of vacuum ε_0 (8.854×10^{-12} F m^{-1}). The coinage metals gold and silver have special dielectric functions, which are the reason for their use as optical materials:[59] (i) For both metals, the real part Re(ε) of the dielectric function is negative within the visible range, with high magnitude values for large wavelengths (see Figure 1.4). (ii) The imaginary parts Im(ε) are comparatively small, indicating low radiation losses caused by absorption in the material. However, gold shows an increased Im(ε) around 400 nm due to interband electronic transitions, which are also the reason for its yellow colour.[60] With its near-zero Im(ε) over the whole visible range, silver outperforms gold in many plasmonic applications. Still in many cases gold is preferred because of its high chemical stability.[61] Such materials with negative Re(ε) and small Im(ε) are able to support

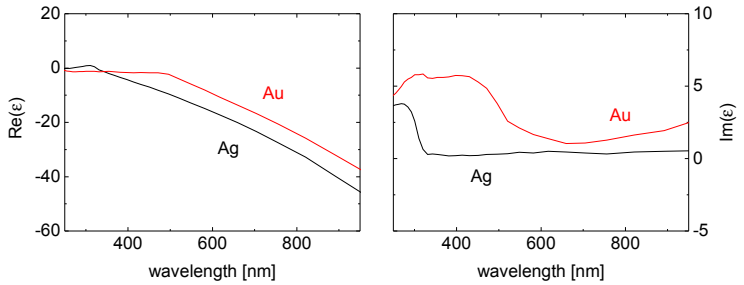

Figure 1.4.: Real and imaginary part of the dielectric function of bulk silver and gold, as determined by Johnson and Christy.[62]

surface plasmons, which are collective oscillations of the surface conduction electrons under electromagnetic radiation. On planar metal surfaces these plasmons spread over large distances (10-100 µm), which is why they are called propagating plasmons (or surface plasmon polaritons).[63] In finite nanostructures like nanoparticles, however, plasmons are spatially confined and thus termed localised surface plasmons (LSPs). While special conditions have to be met for the excitation of propagating plasmons, LSPs can be excited by direct light illumination.[59] Due to

the charge separation induced between electrons and positively charged nuclei, the particle supporting an LSP can be described as an oscillating dipole, as is schematically illustrated in Figure 1.5. The electric field around the particle results from

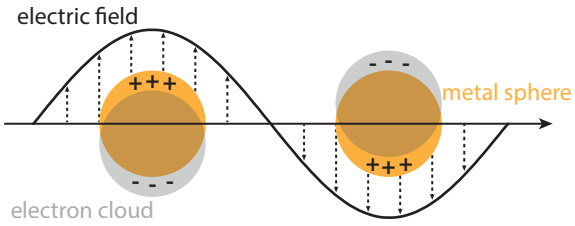

Figure 1.5.: Illustration of a localised surface plasmon.

the superposition of incident field and the field induced by the oscillating dipole. The spatial distribution of the incident field is determined by the diffraction limit and in the order of the wavelength, whereas the field created around the particle is extremely localized and dependent on the nanoscopic structure of the particle. The resulting extreme spatial confinement of the amplified electric field is an important characteristic, relevant e.g. for SERS (see Section 1.3). The so-called quality factor Q is a measure how quickly an LSP decays and also, how strongly the electric field on the surface of a plasmonic particle is amplified.[64] It can be approximated by:

$$Q \approx \frac{-\mathrm{Re}(\varepsilon(\nu))}{\mathrm{Im}(\varepsilon(\nu))}. \tag{1.1}$$

The nanolenses discussed in this thesis are intricate plasmonic nanostructures, consisting of several differently-sized metal nanoparticles. The following three subsections will attempt a basic theoretical description of the fundamental effects at play: First the simplest case, the electromagnetic enhancement around an isolated metal sphere will be discussed (Section 1.1.1), followed by the theory of plasmon hybridisation between multiple spheres (Section 1.1.2). Finally, the nanolensing effect in self-similar chains of nanoparticles will be explained (Section 1.1.3).

1.1.1. Electric field enhancement of isolated, spherical nanoparticles

For an irradiated spherical particle of radius a that is sufficiently smaller than the wavelength λ of the incident wave ($a/\lambda < 0.1$), the magnitude of the incident electro-

magnetic field can be considered to be constant around the particle. This so-called electrostatic approximation enables to analytically solve Maxwell's equations, hence to calculate the electric field **E** around the particle. **E** at the Cartesian coordinates x, y, z, with the distance r to the particle's centre, then is described by:[63]

$$\mathbf{E} = E_{in}\hat{\mathbf{z}} - \left[\frac{\varepsilon - \varepsilon_{out}}{\varepsilon + 2\varepsilon_{out}}\right] a^3 E_{in} \left[\frac{\hat{\mathbf{z}}}{r^3} - \frac{3z}{r^5}(x\hat{\mathbf{x}} + y\hat{\mathbf{y}} + z\hat{\mathbf{z}})\right], \tag{1.2}$$

with ε as dielectric constant of the particle material, ε_{out} as dielectric constant of the surrounding medium, $\hat{\mathbf{x}}, \hat{\mathbf{y}}, \hat{\mathbf{z}}$ as the Cartesian unit vectors, and assuming a z-polarised incident wave of magnitude E_{in}. The centre of the sphere is located at the origin of the coordinate system. As explained in the previous section, ε is a material property and strongly wavelength-dependent. The resonance condition for the term $\frac{\varepsilon-\varepsilon_{out}}{\varepsilon+2\varepsilon_{out}}$ is $\varepsilon = -2\varepsilon_{out}$, upon which the magnitude of the electric field $|\mathbf{E}|$ becomes very large. However, with the imaginary part of ε being non-zero, this condition cannot be reached exactly. The highest values of $|\mathbf{E}|$ are observed along the z-axis. For a molecule located there (with $x = y = 0$, $z = r$), equation 1.2 only has a component in the z-direction and the magnitude of the electric field is given as:

$$|\mathbf{E}| = E_{in} + \left[\frac{\varepsilon - \varepsilon_{out}}{\varepsilon + 2\varepsilon_{out}}\right] 2E_{in} \left(\frac{a}{r}\right)^3. \tag{1.3}$$

The overall maximum field thus is observed on the particle surface (for $r = a$), at the z-apex, with an intensity approximated by $|\mathbf{E}|^2 \approx 4\,E_{in}^2\,|\frac{\varepsilon-\varepsilon_{out}}{\varepsilon+2\varepsilon_{out}}|^2$. Note that this maximal intensity is independent of a. The term $\left(\frac{a}{r}\right)^3$ in equation 1.3 illustrates that $|\mathbf{E}|$ decays rapidly with increasing r. It also shows that the decay is slower for particles with large radii a. Consequently, for $r > a$, large metal particles yield higher field enhancements at a defined distance to the sphere's surface than smaller metal particles do. Though, with increasing particle size, radiation losses damp the LSP and, eventually, the electrostatic approximation is not applicable any more.[59] For non-spherical particles or particle assemblies, no exact solutions of the respective Maxwell equations are available and the respective fields have to be approximated by numerical simulations. These can be carried out by the finite-difference time-domain (FDTD) method,[65] as for example used by the software Lumerical FDTD Solutions (see Methods Section 2.13). In a FDTD simulation, the simulation space is split up into many discrete units for which the Maxwell equations are solved numerically.

1.1.2. Electric field enhancement of nanoparticle dimers

LSPs of particles in close proximity influence each other: In analogy to molecular orbital theory, the dipole modes of the particles split into lower- and higher-energy modes.[66,67] Which of these modes is excited depends upon the orientation of the particle dimer relative to the incident wave polarization. For polarization along the dimer axis, a lower-energy mode with red-shifted resonance wavelength is excited. The enhanced electric field is highly localized to the area between the particles, with the field intensity by far exceeding that of isolated particles if the gap is small enough (see Figure 1.6 A vs. C). For polarization perpendicular to the dimer axis, a higher-energy mode with blue-shifted resonance wavelength is excited. The resonance shift for this transversal mode is smaller in magnitude than the one for the longitudinal mode; the maximal field intensity is similar to that of isolated particles (see Figure 1.6 A vs. B).[68]

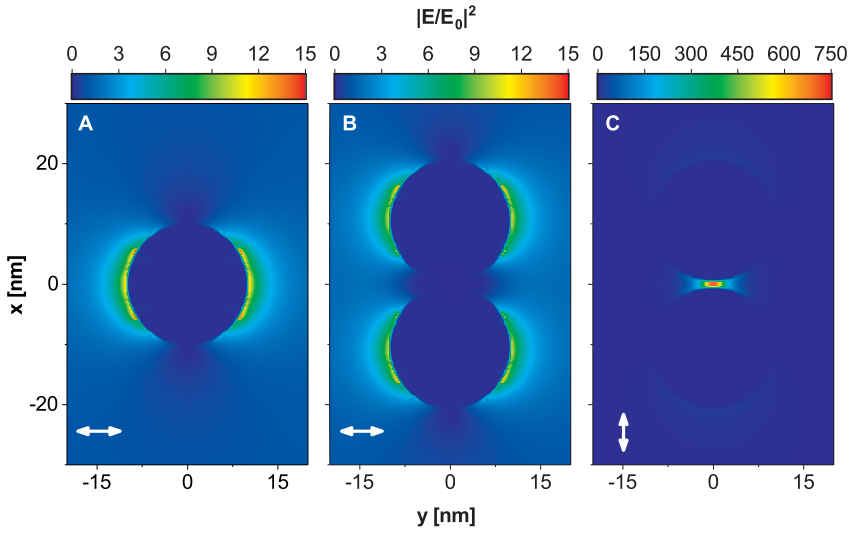

Figure 1.6.: Electromagnetic field intensity enhancement, simulated for a single 20 nm gold nanoparticle (A) and a 20 nm gold nanoparticle dimer with 1 nm gap (B, C). Incident wave polarisation is indicated by arrows at the bottom left of each plot. Excitation wavelength is 633 nm. Please note the different enhancement scale for (C).

1.1.3. Nanolenses

In 2003, Stockman *et al.* described plasmonic nanostructures termed nanolenses, for which they proposed a *cascaded* field enhancement mechanism.[29] The concept was inspired by the giant field enhancements and enhancement fluctuations observed for fractal nanoparticle assemblies.[69,70] The cascaded field enhancement follows a different rationale than the plasmon hybridisation between particles of similar size described in the previous subsection: When a large metal nanoparticle is close to a smaller one, the small particle will be exposed to the enhanced electric field of the larger particle without perturbing it significantly. The LSP of the smaller particle is excited by the enhanced field and will itself enhance the field in its immediate surroundings. If an even smaller particle is placed within that already doubly-enhanced field, it will again support an LSP, and thus introduce another enhancement step.The resulting magnitude of field at the smallest particle in such a self-similar chain depends on the number of iterations n and the resonance quality factor Q of the metal:

$$|\mathbf{E}| \approx |\mathbf{E_{in}}|\, Q^n. \tag{1.4}$$

With a typical value of 10 for the Q of silver, and with three particles involved, this would already result in a field enhancement of 1000.[29] The highest enhancement is predicted to be located in the gap between the two smallest particles. Figure 1.7 shows an FDTD simulation result that illustrates this principle. The number of possible iterations in such a system is limited by the size of the largest particle (with damping, excitation of multipolar modes) and of the smallest particle (Landau damping).[64] Furthermore, the difference in radii should not be too small, otherwise the LSPs of the individual particles cannot be considered independent any more. Simulations taking electrodynamic effects into account have shown that with size ratios as low as 1.5, still high field enhancements can be achieved, with the optimum being a ratio of 2.6 for a system with three spheres.[41] The highest enhancements were predicted for systems with six spherical particles, following a symmetrical geometry, similar to: ◯ ○ ○ ○ ○ ◯.[29]

In a recent study, Pellegrini *et al.* claimed to show that nanolenses provide lower enhancement than respective homodimers of spherical particles.[71] The inter-particle gap of the dimer in their simulations was chosen such that it equals the smallest

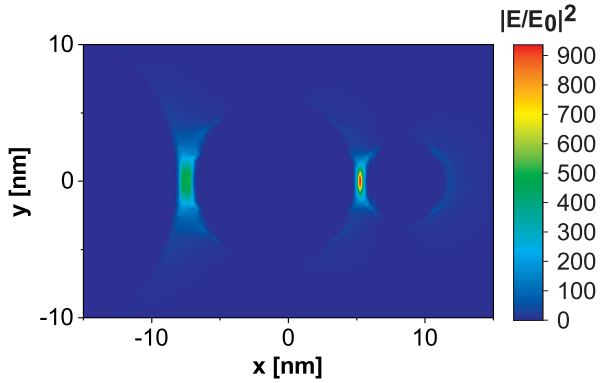

Figure 1.7.: Electromagnetic field intensity enhancement, simulated for a nanolens with 6, 12, and 24 nm gold nanoparticles with 0.5 nm and 1.0 nm gaps. The incident wave is polarised along the symmetry axis. Excitation wavelength is 633 nm.

gap in the compared three-particle nanolens, which cannot be seen as an appropriate comparison. The maximal field enhancement in a plasmonic nanostructure is strictly determined by the ratio between particle size and gap size (within certain boundary conditions such as the electrostatic approximation).[72] Therefore, for an accurate comparison, the gap in the dimer would need to be adjusted relative to the constituent particles' diameters, adopting the same ratio as in the compared nanolens. The field enhancement provided by the respective dimer would drop accordingly.

Apart from delivering high field intensities for surface-enhanced spectroscopy, a potential application for nanolenses lies in surface plasmon amplification by stimulated emission of radiation ('spaser').[73] It was predicted that nanolenses embedded in a host medium of quantum dots could act as efficient spasers, generating intense local fields under the excitation of dark modes.[32] Another interesting phenomenon that was predicted for nanolenses is the enhanced generation of second harmonics.[30] Such intense, highly confined second harmonic local fields could provide new avenues for spectroscopic applications. They could be used for surface-enhanced resonance Raman scattering (SERRS) (*vide infra*) or fluorescence measurements of molecules with resonances in the UV.

1.2. Raman scattering

Classically, the molecule involved in a scattering process can be described as an oscillating dipole which is induced by an incident electromagnetic wave.[74] In an approximation, the induced dipole moment $\boldsymbol{\mu}'$ is proportional to the incident electromagnetic field $\mathbf{E}$ of (angular) frequency ω_0 and amplitude $\mathbf{E_0}$:

$$\boldsymbol{\mu}' = \boldsymbol{\alpha}\mathbf{E} = \boldsymbol{\alpha}\mathbf{E_0}\, cos(\omega_0\, t), \tag{1.5}$$

with $\boldsymbol{\alpha}$ being the polarizability tensor. This tensor is modulated by certain molecular vibrations. Its dependence on the normal coordinate $\mathbf{q}$ of a vibration can be approximated by the first two terms of a Taylor series:

$$\boldsymbol{\alpha} = \boldsymbol{\alpha}_0 + \left(\frac{\partial \boldsymbol{\alpha}}{\partial \mathbf{q}}\right)_0 \mathbf{q}, \tag{1.6}$$

where the subscript 0 of the derivative refers to the equilibrium position of the vibration. During a vibration, $\mathbf{q}$ changes periodically at frequency ω_{vib}:

$$\mathbf{q} = \mathbf{q_0}\, cos(\omega_{vib}\, t). \tag{1.7}$$

Combining equations 1.5, 1.6, and 1.7 yields the periodic change of the induced dipole moment $\boldsymbol{\mu}'$ over time:

$$\boldsymbol{\mu}' = \left[\boldsymbol{\alpha}_0 + \left(\frac{\partial \boldsymbol{\alpha}}{\partial \mathbf{q}}\right)_0 \mathbf{q_0}\, cos(\omega_{vib}\, t)\right] \mathbf{E_0}\, cos(\omega_0\, t). \tag{1.8}$$

Considering the rule for multiplication of cosine functions, $cos(A)\, cos(B) = \frac{1}{2}[cos(A+B) + cos(A-B)]$, equation 1.8 can be rewritten as:

$$\begin{aligned} \boldsymbol{\mu}' = \quad & \boldsymbol{\alpha}_0\, \mathbf{E_0}\, cos(\omega_0\, t) && \} \text{ Rayleigh} \\ & + \frac{1}{2}\left(\frac{\partial \boldsymbol{\alpha}}{\partial \mathbf{q}}\right)_0 \mathbf{q_0}\mathbf{E_0}\, cos((\omega_0 - \omega_{vib})\, t) && \} \text{ Stokes} \\ & + \frac{1}{2}\left(\frac{\partial \boldsymbol{\alpha}}{\partial \mathbf{q}}\right)_0 \mathbf{q_0}\mathbf{E_0}\, cos((\omega_0 + \omega_{vib})\, t) && \} \text{ anti-Stokes.} \end{aligned} \tag{1.9}$$

It becomes clear that the induced dipole moment $\boldsymbol{\mu}'$ has three components, each oscillating at a distinct frequency. The first term of equation 1.9 describes the source of Rayleigh-scattered light, which has the same frequency ω_0 as the incident light.[75] The following terms describe the induced dipole moments responsible for Raman-scattered light, which is characterized either by a loss (Stokes Raman scattering) or gain in frequency (anti-Stokes Raman scattering).[76–78] The term $\left(\frac{\partial \boldsymbol{\alpha}}{\partial \mathbf{q}}\right)_0$ illustrates how a vibration is only Raman-active when the molecule's polarisability $\boldsymbol{\alpha}$ changes at the zero-point of the vibration.

The described classical approach does not explain all observed aspects of Raman scattering, for instance the intensity differences between Stokes and anti-Stokes Raman scattering. They can be rationalized by adopting a quantum-mechanical viewpoint:[79] From there, a scattering process can be understood as the excitation to a virtual state, followed immediately by the transition back to a vibrational level of the electronic ground state S_0 (Figure 1.8). In contrast to fluorescence, it is not

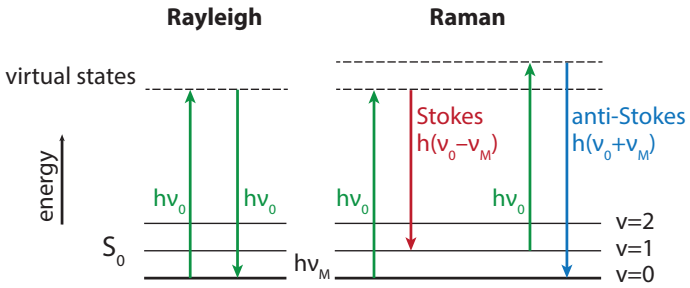

Figure 1.8.: Schematic Jablonski diagrams illustrating the processes of Rayleigh and Raman scattering. Both are instantaneous processes that can be seen as interactions of incoming photons with a virtual state (dotted line). For Raman scattering, Stokes (loss in photon energy) and anti-Stokes (gain in photon energy) processes are shown.

required that the energy of the incident photon matches the energy of an electronic transition in the molecule. For Rayleigh scattering, energies of incident and emitted photon are identical; the molecule returns to the same vibrational state it initially occupied. For Raman scattering on the other hand, the energy of the emitted photon is shifted and a vibrational transition is observed. Two cases can be discriminated: Stokes Raman scattering is the process where the energy of the scattered photon ($h\nu_S$) is lower than that of the incident photon ($h\nu_0$), while the molecule is excited to a higher vibrational level. If the molecule is in an excited vibrational state in the

first place, anti-Stokes Raman scattering can occur: the vibrational energy $h\nu_M$ is transferred to the scattered photon ($h\nu_S = h(\nu_0 + \nu_M)$) and the molecule is left in a lower vibrational state. Consequently, the intensity ratio between Stokes and anti-Stokes scattering depends on the initial population distribution of vibrational states and thus on temperature. Due to its higher intensity at room temperature, in most applications only Stokes-scattered light is detected. The energy difference between incident and scattered photon is defined as the Raman shift and typically expressed as wavenumber: $\Delta\tilde{\nu} = (\nu_0 - \nu_S)/c$, with the unit cm^{-1}. Large molecules can support many different vibrations, each with a different energy, resulting in complex Raman spectra with many molecule-characteristic bands. This high specificity is one of the great strengths of Raman scattering.

The Raman cross section σ_{free} is a measure of the likelihood of a Raman scattering event to occur for an isolated, single scatterer. It is given as the ratio between the power of the Raman scattered light P_S and the power density of the incoming light I_0:

$$\sigma_{free} = \frac{P_S}{I_0}. \tag{1.10}$$

This means that in a measurement with several molecules, the total power of a Raman signal P_S is given as:

$$P_S = I_0 \, N \, \sigma_{free}, \tag{1.11}$$

with N being the number of scattering molecules in the probed volume. Raman cross sections typically are in the range of 10^{-30} cm^2– 10^{-25} cm^2 and thus many orders of magnitude below fluorescence cross sections (ca. 10^{-16} cm^2).[80] When the virtual state coincides with an electronic state of the molecule, resonance Raman scattering is observed. This can increase the Raman cross section and thus the Raman signal by several orders of magnitude, but it is accompanied by background fluorescence, which will obscure the Raman signal if not quenched.

1.3. Surface-enhanced Raman scattering

Raman spectroscopy can identify many different molecules due to their individual vibrational fingerprints. Yet its sensitivity is limited by the extremely low Raman cross sections. SERS is a phenomenon that can help circumvent this disadvantage.

It was first observed by Fleischmann in 1974, who found that molecules adsorbed to rough silver surfaces show increased Raman signal intensities.[15] In the course of later research, while using silver nanoparticle aggregates, extremely increased Raman cross sections were measured that were up to 10^{14}[81] times larger than those of the surrounding solvent molecules. This enabled even the observation of single-molecule Raman scattering.[18,19] SERS is observed for molecules in close vicinity of nanoscopic metal structures, where a variety of effects influence the Raman signal intensity. As discussed in Section 1.1, metal nanoparticles can support LSPs which locally enhance the electric field. The magnitude of this enhancement at a certain frequency is quantified by the factor $A(\nu)$, with $A(\nu) = \frac{|\mathbf{E}(\nu)|}{|\mathbf{E_{in}}(\nu)|}$. The exciting incident field intensity thus is locally enhanced by a factor of $(A(\nu_0))^2$. Likewise, the Raman scattered light can couple to the LSP, upon which its intensity is enhanced by a factor of $(A(\nu_S))^2$. The product of both factors is referred to as the *electromagnetic enhancement*. If the difference in frequencies between incident and scattered light, ν_0 and ν_S, is neglected, $(A(\nu_0))^2$ and $(A(\nu_S))^2$ become equivalent and the intensity of scattered light becomes proportional to $(A(\nu_0))^4 = \frac{|\mathbf{E}(\nu)|^4}{|\mathbf{E_{in}}(\nu)|^4}$, which is often referred to as the E^4-approximation.

When a molecule is close to, or even adsorbed on a surface, its polarizability can be affected and thus also its Raman cross section. This is referred to as *chemical enhancement*. Hence, σ_{free} is substituted by σ_{ads}. The combined effects of electromagnetic and chemical enhancement are summarised in the enhancement factor EF, which then is defined as $EF = \frac{\sigma_{ads}}{\sigma_{free}} (A(\nu_0))^2 (A(\nu_S))^2$. Furthermore, the number of molecules with enhanced scattering N' can differ from the total number of molecules in the probed volume N. Equation 1.11 is modified accordingly overall and the SERS signal P_{SERS} is described by:

$$P_{SERS} = I_0 N' \sigma_{ads} (A(\nu_0))^2 (A(\nu_S))^2 = I_0 N' \sigma_{free} EF. \tag{1.12}$$

SERS spectra can differ from respective un-enhanced Raman spectra in both, peak position and relative peak intensity. Orientation and distance of the scattering molecule relative to the surface of the plasmonic nanostructure greatly influence which vibrations are enhanced. Also, the chemical enhancement will act differently on different molecular vibrations. Such variations have a great impact since SERS spectra typically are dominated by the strongly enhanced signals from only a few

molecules, those which are located in the small foci of highest field enhancement.[82] SERS under resonant conditions is referred to as SERRS. While the overall Raman signal typically increases through the resonance, the electromagnetic enhancement itself can be negatively affected.[83] Conveniently, accompanying fluorescence is quenched in close proximity to metal surfaces.

1.4. The structure of DNA and a historical overview on structural DNA nanotechnology

In nature, deoxyribonucleic acid (DNA) developed as a highly compressed storage for genetic information, able to code the blueprint of a whole organism. Watson and Crick discovered its structure to be a double helix of two antiparallel polynucleotide strands (Figure 1.9 A).[84] The right-handed double helix of B-DNA (which is the most common form) was determined to be 2 nm in diameter[84] and to have a helical twist of approximately 10.5 nucleotides per turn,[85] with 0.34 nm rise per nucleotide.[86] The nucleotides constituting the two strands consist of a phosphate group, the sugar 2-deoxyribose and one of the four nucleobases adenine (A), cytosine (C), guanine (G) and thymine (T). Genetic information is encoded in the sequence of nucleobases and the genetic code is used to translate it into amino acid sequences.[87] The nucleobases of two single strands selectively interact by forming pairs ('Watson-Crick basepairing'): adenine binds thymine via two hydrogen bonds, cytosine forms three hydrogen bonds with guanine. The enthalpic gain from these specific interactions enables double helix formation if the nucleotide sequences of two single strands are complimentary. Further factors driving the double helix assembly are the hydrophobicity of nucleobases, nucleobase stacking interactions and the polarity of the phosphate groups.

Structural DNA nanotechnology exploits the principle of sequence-dependent DNA hybridisation for construction purposes, with DNA strands being the building material and nucleobases understood as a programmable glue. One of the simplest assembly units is the Holliday junction,[90] a motive found in nature with two crossing double helices (Figure 1.9 B).[91] Natural Holliday junctions are not stable since sequence symmetry causes the branching point to migrate along the strands. By introducing asymmetric sequences, stable four-arm junctions can be received.[92]

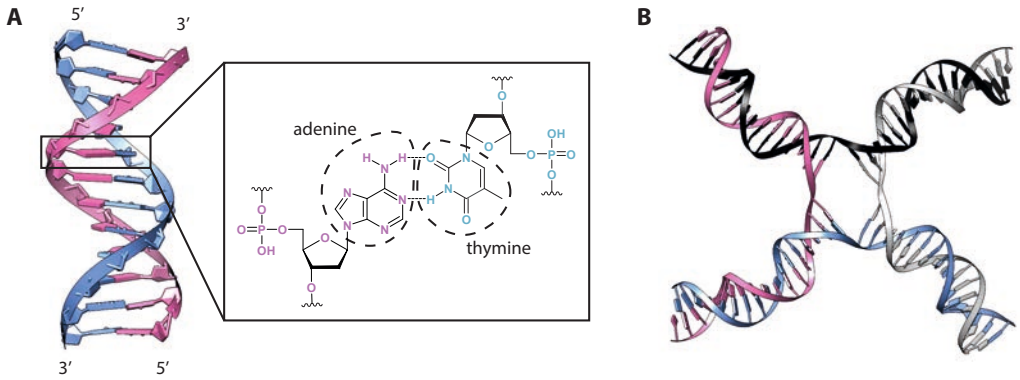

Figure 1.9.: (A) Structural model of a DNA double helix[88] and chemical structure of a Watson-Crick base pair of deoxyadenosine monophosphate (pink) and deoxythymidine monophosphate (blue). (B) Structural model of a Holliday junction.[89]

Similarly, branched points with more than four arms can be produced as further topological elements.[93] In 1982, Ned Seeman conceived the idea that many Holliday junctions could be joined by sticky end hybridisation[94] to form periodic nucleic acid networks.[95] Those, he reasoned, could be used as programmable scaffolds for protein attachment in crystallography. Some years later it was his laboratory that used the principle of interconnected DNA branches to construct the first artificial DNA nano-object, a cube with double helices as edges (Figure 1.10 A).[96] By introducing two crossovers between antiparallel DNA helices, stiffer units (so-called DX molecules, Figure 1.10 B) were achieved that could form larger networks.[104] In his seminal publication from 2006, Rothemund showed how to improve the yield of large and complex DNA structures by using a technique he termed 'scaffolded DNA origami' (Figure 1.10 C).[53] DNA origami—in the scientific community it has become common to omit the 'scaffolded'—spurred the development of DNA nanotechnology and due to its simple and robust synthesis protocol it is now used as a tool in many laboratories world-wide.[98] Soon, three-dimensional DNA origami scaffolds were presented[100] (Figure 1.10 D-F), together with a CAD software for custom-designed shapes of DNA origami scaffolds.[105] Further notable developments in DNA nanotechnology include DNA bricks[102] (Figure 1.10 G), which are modular three-dimensional structures exclusively made of oligonucleotides, and origami-like three-dimensional polyhedral meshes (Figure 1.10 H).[103,106]

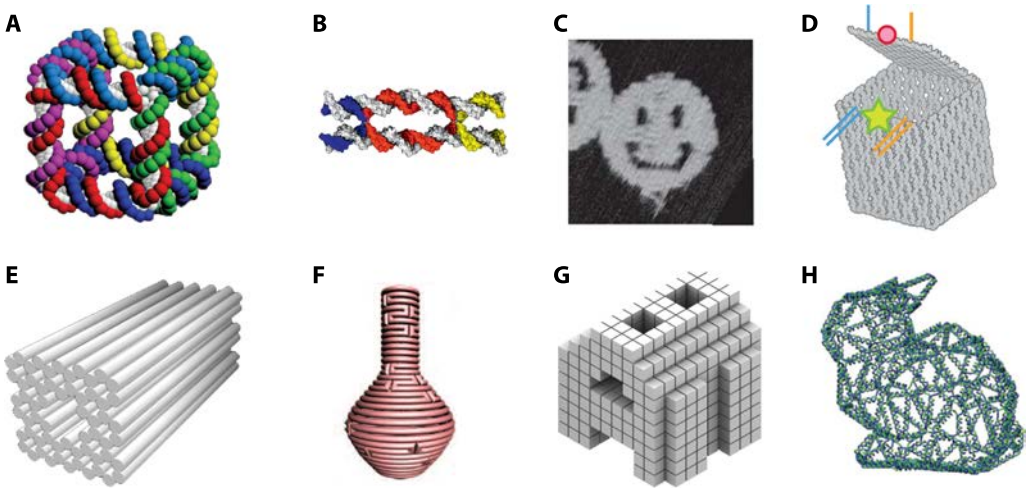

Figure 1.10.: Structures representing important steps in the development of DNA nanotechnology. (A) DNA cube, 1991;[97] (B) DX molecule, 1993;[98] (C) 2D DNA origami, 2006 (AFM image size: 165 nm×165 nm);[53] (D) single-layer 3D DNA origami, 2009;[99] (E) multilayer 3D DNA origami, 2009;[100] (F) curved 3D origami, 2011;[101] (G) DNA bricks, 2012;[102] (H) 3D polyhedral mesh, 2015.[103] Images modified from annotated references, sizes scaled.

1.5. DNA origami

In DNA origami, a large set of short, artificial, single-stranded DNA molecules ('staple strands') directs the route of a very long, natural, single-stranded DNA molecule ('scaffold strand') by hybridizing at defined positions on that scaffold strand. The resulting structure's shape is defined by the staple sequences and held together by the many crossovers between staple strands and scaffold strand. For an assembly schematic see Figure 1.11. A key property of DNA origami and other DNA nanostructures is that each nucleotide's position is defined by the input DNA sequence and thus known and modifiable. By placing different modifications at defined positions on the DNA origami scaffold, self-assembly of even more-complex nanostructures is enabled. Although DNA is a relatively inert material, it is easy to introduce functionality to selected positions on a DNA origami scaffold: Staple strands with a great variety of chemical modifications (thiols, biotin, aldehydes, amines, fluorescent dyes, ...) are commercially available. Furthermore, staple strands can be extended so that single-stranded overhangs of defined sequence protrude from the DNA origami

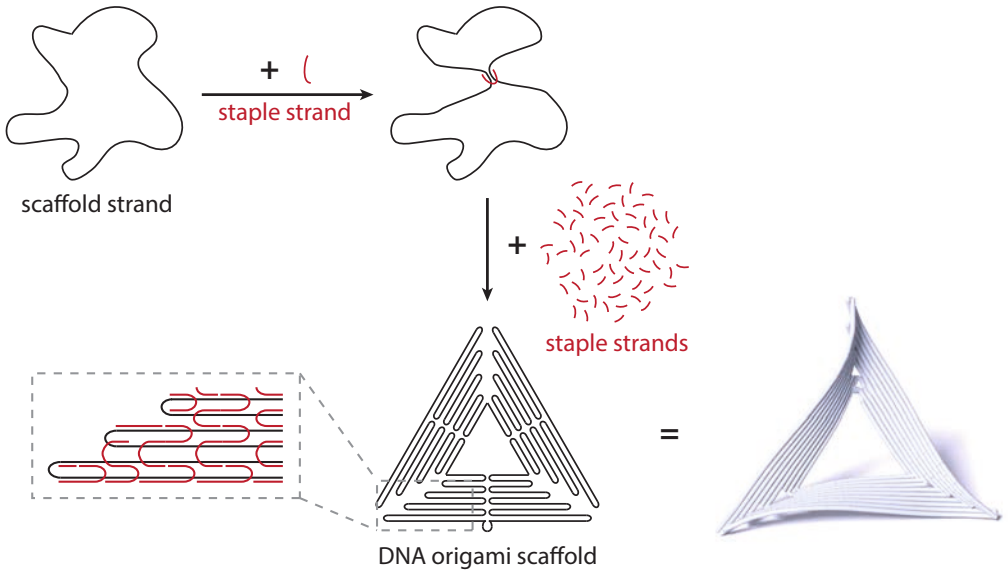

Figure 1.11.: Illustration of the folding process in DNA origami. Each staple strand has a different nucleotide sequence and thus binds at another position of the scaffold strand. As a consequence, the scaffold strand is routed along the target shape, in this case a triangle with a central hole. The 3D model of the folded DNA origami scaffold is based on simulations carried out by CanDo.[54]

scaffold ('capture strands'). Those capture strands can be used as attachment points for nanocomponents that carry DNA single strands of a complementary sequence, such as other DNA origami scaffolds[107] or DNA-coated nanoparticles;[108] as aptamers they can directly bind molecules.[109] For a more detailed view on nanoparticle binding refer to Section 1.6, subsequent to this one. The protrusion angle of a capture strand is determined by the intrinsic twist of DNA double-helices. The capture strand will protrude at an angle depending on its location within the helical turn of the double strand. In the case of two-dimensional DNA origami, this can be exploited to determine the face on which a capture strand protrudes and respective nanocomponents are bound. As an interfering phenomenon, 'molecular threading' can occur: It was observed that long capture strands can wind though the holes between crossovers in the DNA origami scaffold in order to overcome the steric confinement imposed by a surface.[110]

The applicability of the standard DNA origami used by most research groups is limited by the requirement of high ionic strength buffers. Typically, magnesium

chloride at concentrations of at least 10 mM is used;[54] assembly in sodium chloride is also possible, but there, high concentrations (>1 M) are required.[111] The cations shield the negative charges of the phosphate backbone, which are densely packed in classical DNA origami and would otherwise drive the structures apart. Recently presented DNA origami scaffolds constructed from polyhedral meshes overcome this limitation: Since helices are not so closely routed, these structures are stable even in PBS buffer.[103] (An exemplary structure design was displayed in Figure 1.10 H.) Another viable strategy is to stabilise existing DNA origami scaffolds against low salt conditions, either by (i) linking staples after assembly with click chemistry, forming a 'chain-armor',[112] or by (ii) enveloping them in a cationic block copolymer layer.[113] Another limitation of DNA origami is the size restriction imposed by the available scaffold strands. This was partially overcome by using longer scaffold strands (51 kb vs. 7 kb),[114] or by joining DNA origami scaffolds either via sticky end hybridisation[107] or shape complementarity.[115]

The custom structure design with placement of non-DNA objects at defined positions renders DNA origami a versatile toolbox with countless applications. Amongst others, DNA origami helped create lipid membrane channels,[116] nanocarriers for drug delivery,[117] nanowires,[118] enzymatic nanoreactors,[119] and functional scaffolds for fundamental biophysical investigations.[120–122] Alone in the Bald group it was used for as different purposes as to build selective potassium sensors,[123] photonic wires,[124] light harvesting systems,[125] plasmonic nanostructures,[27] and to determine cross sections of DNA damage towards electron[126] or UV radiation.[127] The following section will illustrate the application of DNA origami in plasmonics.

1.6. DNA-coated metal nanoparticles and DNA origami-based plasmonics

DNA-coated gold nanoparticles were developed already ten years before the invention of DNA origami, in parallel by Mirkin and Alivisatos, to serve as versatile tools in DNA analytics.[128,129] Thiolated DNA single-strands were used to form a coating layer on the gold nanoparticles, taking advantage of the strong sulfur-gold bond.[130] Analogous silver nanoparticles followed later.[131] Such DNA-coated metal nanoparticles can be bound on DNA origami scaffolds by capture strands

of complementary sequence, for illustration see Figure 1.12 A. A recent review by Seeman and Mirkin describes the synergistic co-evolution of the fields of DNA nanotechnology and DNA-coated gold nanoparticles.[132] The high ionic strength buffer

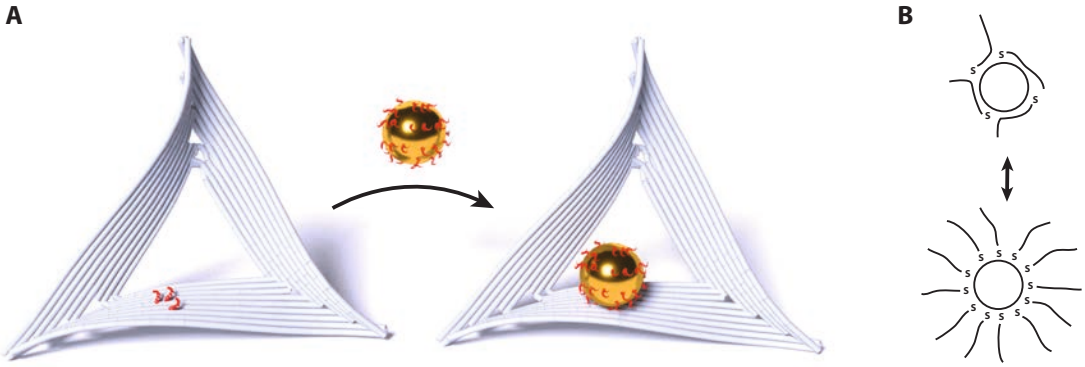

Figure 1.12.: (A) A single DNA-coated gold nanoparticle is immobilised by three capture strands on a triangular DNA origami scaffold. (B) Schematic of a Nanoparticle with a low DNA coating density due to unspecific strand adsorption vs. one with a high coating density.

that stabilizes DNA origami scaffolds is a challenging environment for DNA-coated metal nanoparticles. Only high coating densities are able to provide the electrostatic shielding that is necessary to prevent particle aggregation in the magnesium-containing buffer. Generally, such high coating strand densities are achieved by the so-called salt ageing procedure, where the sodium chloride concentration is elevated in a step-wise manner.[133] The salt shields the mutual repulsion between the negatively charged coating strands, so that more and more coating strands bind on the particle. The particles' stability against salt rises concomitantly.[134] The process can be aided by lowering the pH, which partially protonates the phosphate groups in the DNA backbone and thus further decreases electrostatic repulsion.[135] Modifying the chemical structure of the coating strands by incorporating ethyleneglycol moieties is another strategy to increase particle stability,[134] though synthesis costs rise considerably for such doubly-modified DNA strands. Also, small molecules that adsorb to the particle surface—such as nonionic fluorosurfactants—can aid the coating procedure by blocking unspecific adsorption of nucleobases.[136] Such unspecific adsorption (as illustrated in Figure 1.12 B) can severely limit the DNA loading.[137] It strongly depends on the base composition of the coating strands since the four

nucleobases differ in their affinity to metal surfaces: Adenine shows the highest affinity to gold, followed by cytosine, guanine and thymine.[138] For that reason, coating strands with exclusively thymine are usually preferred for gold nanoparticles.[139] For silver nanoparticles, the opposite trend was reported: particles coated with adenine strands were more stable than those coated with thymine strands.[140] Since the thiol-silver bond is comparably weak,[130] it is advantageous to use DNA strands with multiple thiols for silver nanoparticles to prevent an early strand detachment after the coating procedure.[131] In most plasmonics applications, an efficient plasmon coupling between the individual particles is desired, which necessitates small interparticle gaps. For DNA-coated nanoparticles, the minimal possible gap size is set by the coating thickness. It can be decreased by short coating strands, but if too short ($\lesssim$ 13 nt), their stabilisation efficiency drops considerably.[137] Thus, for an efficient plasmon coupling and high field enhancements, the *relative* gap size has to be decreased, so large plasmonic nanoparticles have to be used. Since DNA coating density decreases with increasing nanoparticle size (which can be rationalized by the lower curvature of these particles), and large particles generally are not as stable, this poses an additional challenge when coating the particles.[134]

With several capture strand groups, DNA origami scaffolds can control the relative geometry of multiple DNA-coated metal nanoparticles. The precision of this placement is restricted by the routing of staple strands in the scaffold, i.e., by the density of potential capture strand positions. For a typical DNA origami, this relates to a resolution of a few nanometres. Depending on capture strand placement and particle size, the flexibility of the respective DNA structures can add some additional uncertainty. After proof-of-principle experiments demonstrating the conjugation of gold[108] or silver nanoparticles[141] with DNA origami scaffolds, such plasmonic conjugates have been used in many different studies.[142] The directed placement of spherical gold nanoparticles[143] or gold nanorods[144] for example can be exploited to create nanostructures with designed chirality and strong circular dichroism. Implemented in a switchable DNA origami scaffold,[145] these can sense the pH.[146] Long chains of plasmonic nanoparticles can act as waveguides[7] which 'transport' the excitation from one point in space to another. In the future such structures might be used in nano-optoelectronics. Efforts to build waveguides with DNA origami comprise the improvement of the particle binding yield,[147] extension over several scaffolds[148] and the implementation of a switch.[149] These systems suf-

fer from the inherent losses due to damping in excited plasmonic systems. In an attempt to overcome this limitation, a recent study investigated a non-dissipative excitation transfer between two gold nanoparticles, mediated by an off-resonant silver nanoparticle.[150] The intense near-fields provided by plasmonic nanostructures can also be used for fluorescence enhancement. Since here two processes—quenching by the metal surface and the enhancement of the exciting light—compete, exact control over the placement of the fluorophore is crucial.[151] As for the metal nanoparticles, this can be ensured by the DNA nanostructures. Fluorescence enhancement on DNA origami scaffolds has been demonstrated using dimers of gold[152] and silver nanoparticles,[153] as well as gold nanorods.[154]

A prime application for plasmonic nanoparticle aggregates is SERS. The first study that used DNA origami to create SERS substrates was conducted in the Bald group,[27] with similar reports from other groups following *en suite*. (See Table 1.1 for details.) More refined approaches, enabling single-molecule SERS, were published recently.[155–157] The improved signal intensities were achieved by silver-coating,[155] heat-tuning,[156] or nanostars,[157] respectively. Prinz *et al.* furthermore investigated the influence of a graphene coating on such a SERRS system and found that it is able to decrease the photobleaching rate significantly.[158] Most of the mentioned studies of SERS on DNA origami substrates actually used SERRS, exploiting the stronger Raman scattering of resonant dye molecules.

Table 1.1.: SERS studies with DNA origami substrates. Except Pilo-Pais *et al.*, all used fluorescent dyes under resonant excitation as reporter molecules. 'Gold-' and 'silver-growth' indicate a post-assembly deposition of the respective metal.

	plasmonic aggregate	**Raman reporter**
Prinz *et al.*, 2013[27]	gold dimer, gold-growth	few dyes on DNA origami
Kühler *et al.*, 2014[159]	gold dimer	intercalating dyes
Pilo-Pais *et al.*, 2014[160]	gold tetramer, silver-growth	4-aminobenzenethiol adsorbed on particles
Thacker *et al.*, 2014[161]	gold dimer	unspecifically adsorbed dye
Prinz *et al.*, 2016[155]	gold dimer, silver-growth	single dye
Simoncelli *et al.*, 2016[156]	gold dimer	single dye
Tanwar *et al.*, 2017[157]	gold nanostar dimer	single dye

2. Methods and sample preparation

The general workflow for the preparation of nanolenses is shown in Figure 2.1. Gold or silver nanoparticles are coated with thiol-modified DNA single strands (Section 2.2) and DNA origami scaffolds are self-assembled (Section 2.3). For those samples where the protein streptavidin is to be detected, streptavidin is bound on the assembled scaffolds (Section 2.4). The DNA-coated particles are bound via DNA-DNA hybridisation onto the DNA origami scaffold (Section 2.5). Nanolenses are separated from unbound nanoparticles by gel electrophoresis (Section 2.6) and for single-nanolens characterisation, samples are deposited on silicon wafers (Section 2.7). The nanolenses are characterised by Raman spectroscopy (Section 2.8), AFM (Section 2.9), SEM (Section 2.10), dark-field spectroscopy (Section 2.11) and UV/Vis extinction spectroscopy (Section 2.12). Furthermore, FDTD simulations are carried out (Section 2.13).

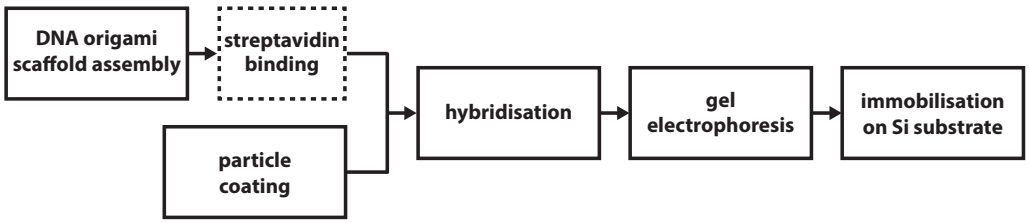

Figure 2.1.: Workflow chart for nanolens sample preparation.

2.1. Buffers and reagents

1xTAE 40 mM tris(hydroxymethyl)aminomethane (Tris), 20 mM acetic acid, 1 mM ethylenediaminetetraacetic acid (EDTA)

TAE-Mg 1xTAE with 11 mM $MgCl_2$

TAE-Mg-SDS TAE-Mg with 0.02 % sodium dodecyl sulfate (SDS)

6x loading buffer 30 % glycerol, 11 mM $MgCl_2$

DNA is purchased from IDT technologies (unmodified staple strands), FRIZ Biochem (DTPA-modified coating strands), metabion (thiol-, dye- or biotin-modified strands), or Eurofins (M13mp18 scaffold strand), and all other chemicals from Sigma-Aldrich if not stated otherwise. Gold nanoparticles and 20 nm silver nanoparticles are purchased from BBI Solutions. DNA sequences are given in 5'-to-3' direction. Nanoparticle size is noted as diameter.

2.2. Nanoparticle coating

Nanoparticles are coated with thiol-modified single stranded DNA. The coating has three purposes: (i) enabling the selective hybridization to complementary capture strands on DNA origami scaffolds, (ii) the stabilization against aggregation in the high ionic strength buffer that is required for the integrity of the DNA origami, and (iii) the labelling of selected nanoparticles with the fluorescent dye 5-carboxytetramethylrhodamine (TAMRA, see Figure 2.2 A for structure). TAMRA serves as a reporter molecule for the characterization of the nanolenses regarding their ability to enhance Raman scattering signals. Its absorption maximum is at 542 nm (emission maximum: 568 nm),[162] so that under 532 nm laser excitation, resonant Raman scattering is expected, which renders TAMRA a potent Raman reporter with high signal intensity. Fluorescence is efficiently quenched since the dye is close to gold surfaces. The TAMRA molecules are attached at the solution-facing 5'-end of the DNA coating strands. The resulting lack of direct interaction with the gold nanoparticle surface should lead to very small or negligible contributions of

chemical enhancement, and a main contribution to potential SERS enhancement by electromagnetic enhancement. The average number of TAMRA molecules on a certain batch of nanoparticles is determined by the fluorescence method described in Section 2.2.3.

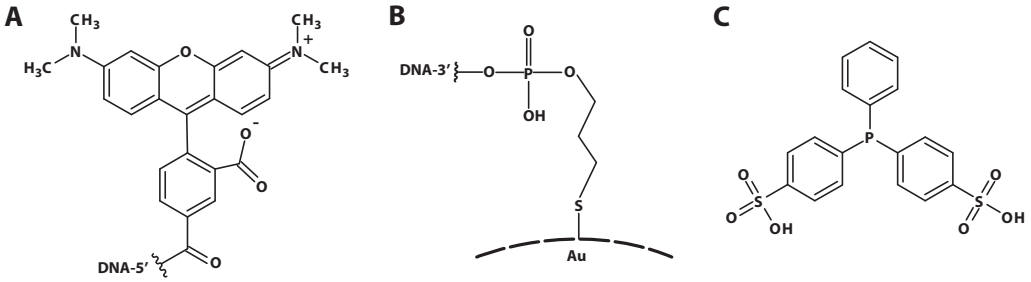

Figure 2.2.: (A) Molecular structure of TAMRA. (B) 3'-thiol-modified DNA single strand bound to a gold surface. (C) Molecular structure of bis(p-sulfonatophenyl)phenylphosphine (BSPP).

2.2.1. Gold nanoparticle coating

Figure 2.2 B illustrates how a thiol-modified DNA strand is coupled to the surface of a gold nanoparticle. Two methods were developed to coat gold nanoparticles with single-stranded DNA: a fast one at pH 3 and a slow salt ageing protocol, where the ionic strength is increased in small steps. The coating protocol from the first, preliminary studies is also shown.

pH 3 method

Most gold nanoparticles are coated with a rapid protocol at pH 3, modified from Zhang *et al.*[163] Citrate-stabilized gold nanoparticle suspension (1 nM (60 nm particles), 10 nM (20 nm particles), 5 nM (10 nm particles)) is mixed with DNA coating strands (15 µM (60 nm particles), 22.5 µM (20 nm particles), 2.5 µM (10 nm particles)) in 0.02 % SDS and incubated for 30 min. 0.5 M citrate buffer (pH 3) is added to a final concentration of 10 mM and the solution is incubated for another 45 min. It is important to note that the citrate buffer is prepared from trisodium citrate, with pH adjustment by HCl, so that there are three equivalents of sodium for each citrate molecule in the buffer stock solution. 2.5 M NaCl is added to a final concentration of 300 mM and after shaking for 3 h, more 2.5 M NaCl is added, to a final concentration

of 600 mM. After overnight incubation, 400 µl TAE-Mg-SDS are added. In order to remove unbound DNA, gold nanoparticles are either sedimented by centrifugation (60 nm / 20 nm particles) or separated off by centrifugal filters (10 nm particles, Amicon Ultra 100 kDa molecular weight cut-off (MWCO), Millipore) and the respective supernatant or filtrate is removed. After four more cycles of TAE-Mg-SDS addition, centrifugation and supernatant or filtrate removal, the particle suspension is stored at 4 °C. The thorough purification is essential for high hybridisation yields because otherwise, unbound coating strands will compete for hybridisation on the capture strands of the DNA origami scaffold. The DNA coating should allow optimum plasmon coupling between the gold nanoparticles. Thus the length of coating strands is set to 13 bases, with 9 base recognition sequences. For shorter lengths, a rapid loss in stability has been reported.[137] The coating strands are 3'-thiol-modified and have the sequence $(XTT)_3$-T_4-SH, with X representing A, G, or T, respectively. The explicit combinations of sequences and particles sizes used in the different nanolens assemblies are given in Table 2.1. For the experiments with TAMRA-labelled 60 nm gold nanoparticles, a 1:1 mix of 5'-TAMRA-labelled / unlabelled $(TTT)_3$-T_4-SH coating strands is used. 60 nm gold nanoparticles with a pure TAMRA-$(TTT)_3$-T_4-SH coating do not withstand the high ionic strength buffers. Generally, particle stability decreases when TAMRA-modified coating strands are used.

Table 2.1.: DNA strands coating the respective nanoparticles for assembling different nanolenses. The individual nanolens designs will be introduced in the following Section 2.3. As mentioned explicitly in the text, some experiments used coating strands that carried 5'-TAMRA modifications as Raman probes. In these cases, the TAMRA-labelled nanoparticle in the respective nanolens will be marked by an asterisk.

		nanoparticle size		
	design	10 nm	20 nm	60 nm
gold nanolens	20-10-60	$(ATT)_3$-T_4-SH	$(GTT)_3$-T_4-SH	$(TTT)_3$-T_4-SH
	20_b-10-60	$(ATT)_3$-T_4-SH	$(GTT)_3$-T_4-SH	$(TTT)_3$-T_4-SH
	10-20-60	$(GTT)_3$-T_4-SH	$(ATT)_3$-T_4-SH	$(TTT)_3$-T_4-SH
silver nanolens	20-10-60	$(ATT)_3$-T_4-SH	$(GTT)_3$-T_4-SH	$(TTT)_3$-T_4-DTPA

Salt ageing

The pH 3 method does not yield stable 20 nm nanoparticles with TAMRA-$(GTT)_3$-T_4-SH DNA. Therefore, a small-step salt ageing protocol at pH 7 is applied. For stabilisation during the initial salt ageing steps, gold particles are firstly coated with bis(p-sulfonatophenyl)phenylphosphine (BSPP, see Figure 2.2 C for structure).[58] 5 mg of BSPP (sensitive to oxygen, to be stored under nitrogen) are added to 15 ml of citrate-stabilized 20 nm gold nanoparticles (1 nM) and stirred in the dark over night. NaCl is added to the suspension until the colour turns deep blue. The sample is centrifuged at 500 rcf for 30 min and the supernatant is removed. 0.3 ml of 2.5 mM BSPP are added to resuspend the particles. 0.5 ml of methanol are added and the sample is centrifuged again at 500 rcf for 30 min. The supernatant is discarded and 0.2 ml of 2.5 mM BSPP are used for resuspension. The thus BSPP-coated particles are stored at 4 °C and can be used for several months.

A mixture of 6 nM BSPP-coated 20 nm gold nanoparticles and 13.5 µM thiol-modified DNA (1:1 TAMRA-$(GTT)_3$-T_4-SH / $(GTT)_3$-T_4-SH) in 0.02 % SDS, 50 mM NaCl and 0.5x TAE is incubated for 1 h, then the NaCl concentration is increased to 100 mM and the solution is left shaking over night. The NaCl concentration is further increased, to 700 mM, in 50 mM steps every 40 min. After another overnight incubation, particles are purified by five cycles of buffer addition (400 µl TAE-Mg-SDS), centrifugation and supernatant removal.

Preliminary coating protocol

The following protocol was applied to coat gold nanoparticles for preliminary studies. As it proved to work only for small particles, the more advanced protocols from above were applied in the later experiments. 15 ml of citrate-stabilised gold nanoparticles ($OD_{520nm} = 0.1$) are BSPP-coated as described above. 25 µl of the BSPP-coated particles are mixed with 22 µl thiolated coating strand (100 µM), 1 µl of 5 M NaCl, 5 µl of 10x TAE and 47 µl of water. After one day of shaking at room temperature, 2 µl of 2.5 M NaCl are added, increasing the NaCl concentration from 50 mM to 100 mM. 2 µl of 2.5 M NaCl are added again after one to five days, then three more times, each after over night incubation, until a NaCl concentration of ca. 300 mM is reached. For work-up, 100 µl TAE-Mg are added, the sample is transferred to 100 kDa MWCO Amicon centrifugal filters (30 kDa for 5 nm gold nanoparticles) and

exposed to five cycles of centrifugation, flow through removal and buffer addition. Circa 30 µl of deep red particle solution are recovered.

2.2.2. Silver nanoparticle coating

Coating silver nanoparticles is complicated by the fact that the bond between sulfur and silver is weaker than the one between sulfur and gold.[130] For this reason, a modified salt ageing protocol is used here. Citrate-stabilised silver nanoparticles (0.4 nM (60 nm particles), 4 nM (20 nm particles), 5.6 nM (10 nm particles)) are mixed with a fresh 2.5 mM BSPP solution, yielding a final BSPP concentration of 0.5 mM. The suspension is kept at 40 °C whilst shaken for 30 min to 60 min. SDS is added to a final concentration of 0.02 % and DNA coating strands are added at a molar excess of 30,000x (60 nm particles), 2000x (20 nm particles) or 150x (10 nm particles), respectively. Samples are incubated at 40 °C for 10 min and then the NaCl concentration is elevated in a stepwise manner, with 20 min of shaking at 40 °C between each step. First, 1 M NaCl is added in 20 mM steps until a concentration of 100 mM is reached. Then, the NaCl concentration is increased to 150 mM, 200 mM, 300 mM, 400 mM, 600 mM and 750 mM, in the last four steps by adding 2.5 M NaCl. The suspension is mixed 1:1 with TAE-Mg-SDS and kept at 40 °C for another 30 min.[164] 60 nm and 20 nm particles are purified by five cycles of centrifugation, supernatant removal and pellet resuspension in 400 µl TAE-Mg-SDS. 10 nm particles are purified with centrifugal filters (Amicon Ultra 100 kDa MWCO, Millipore), also with five cycles of centrifugation and buffer addition. Due to the weaker surface binding, the coating strands detach much faster from the silver nanoparticles, especially in the case of large nanoparticles. Therefore it is critical to execute at least three additional purification steps immediately before applying the coated silver nanoparticles in a hybridisation reaction. In order to decrease strand detachment from the 60 nm particles, these are coated with dithiol-phosphoramidite-modified strands (DTPA, see Figure 2.3).[165] DTPA-modified strands are reported to show a considerably lower dissociation rate on gold nanoparticles.[166] The

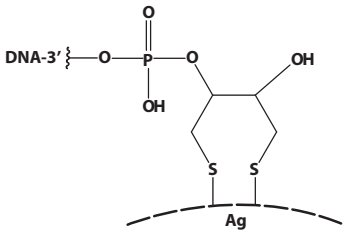

Figure 2.3.: DTPA-modified DNA strand, bound to a silver surface by its two thiol moieties.

same is to be expected for silver particles.[131] Before use, the DTPA-modified strands are deprotected for 1 h by addition of 9.1 mM tris(2-carboxyethyl)phosphine (TCEP) to 91 µM DNA. The reaction mixture is used without further purification. The sequences of the DNA strands applied to coat the respective silver nanoparticles are displayed in Table 2.1. Citrate-stabilized silver nanoparticle stock solutions are stored at 4 °C under argon to prevent oxidation. Once coated with DNA, the silver nanoparticles were found to be effectively protected against oxidation.[167,168] Interestingly, adenine-containing strands are reported to be more suitable for coating and to show less unspecific adsorption on silver than respective thymine strands, a behaviour opposite to what is observed on gold.[140] Nevertheless, with the robust coating protocol presented here, even 60 nm silver particles can be coated with DNA strands exclusively built with thymine.

2.2.3. Determination of coating strand density

In order to determine the number of TAMRA-modified DNA strands on gold nanoparticles, a protocol introduced by Hurst *et al.*[134] is applied: During overnight incubation, the DNA strands on the gold nanoparticle surface are replaced by an excess of dithiothreitol (0.5 M). After removing the gold nanoparticles by centrifugation, the supernatant is diluted and the concentration of TAMRA-modified DNA is determined with a HORIBA Jobin Yvon FluoroMax-P fluorescence spectrometer. A calibration curve is created from a blank sample and nine known concentrations of TAMRA-modified DNA between 0.5 nM and 15 nM. The TAMRA concentration is multiplied by the dilution factor and divided by the initial gold nanoparticle concentration to yield the number of TAMRA strands per particle.

2.3. Assembly of DNA origami scaffold

The sharp triangle introduced by Rothemund is used as the scaffold for the nanolenses; it has a side length of 127 nm and consists of a single layer of double-stranded DNA.[53] A schematic of the folding process was shown in Figure 1.11 on page 19. Compared to other DNA origami scaffolds, the sharp triangle features high folding yields and low susceptibility to oligomerisation, the latter because all double helix ends are contained within the scaffold itself. It self-assembles when

208 short DNA single strands (termed staple strands) and the long, single-stranded scaffold strand M13mp18 are subjected to a temperature program. 200 nM of each staple strand are mixed with 5 nM scaffold strand in TAE-Mg, in a total volume of 100 µl. The sample anneals during the following programme in an advanced primus 25 thermocycler (PEQLAB): rapid heating to 80 °C, then cooling down from 80 °C to 66 °C at 2 °C/min, from 65 °C to 25 °C at 0.5 °C/min and from 24 °C to 8 °C at 1 °C/min. The sample is transferred to an Amicon Ultra 100 kDa MWCO centrifugal filter from Millipore, and excess staples are removed by five successive cycles of 400 µl TAE-Mg buffer addition and centrifugation at 5200 rcf for 7 min. Typically, this procedure yields 20 µl of 15 nM DNA origami scaffold. Staple strand sequences can be found in Table A.1 on page 115 of the Appendix, together with a full map of the DNA origami scaffold (Figure A.1, page 99). In order to form capture strands, selected staple strands are extended at their 5'-end, typically by 28 nucleotides. Groups of capture strands with orthogonal sequence are positioned on the DNA origami scaffold in three different configurations, enabling three different nanolens designs. The position of the modified staple strand determines which face of the DNA origami scaffold the extension will protrude on. The number of capture strands on the DNA origami scaffold is adjusted with respect to the nanoparticle size: 60 nm particles are bound by four to five capture strands, 20 nm particles by four, and 10 nm particles by three. The capture strand sequences and positions that realise the different nanolenses are displayed in the following subsections.

Design 20-10-60

In this design, all capture strands protrude on the same face of the DNA origami scaffold (i.e., *downwards* in Figure 2.4). Capture strands are spaced at approximately 11 nm in helix direction, so that the distance between the centres of capture strand groups is circa 22 nm. After hybridisation of nanoparticles coated with the respective complementary DNA strands, this DNA origami scaffold yields nanolenses with nanoparticles in the order: 20 nm, 10 nm, and 60 nm.

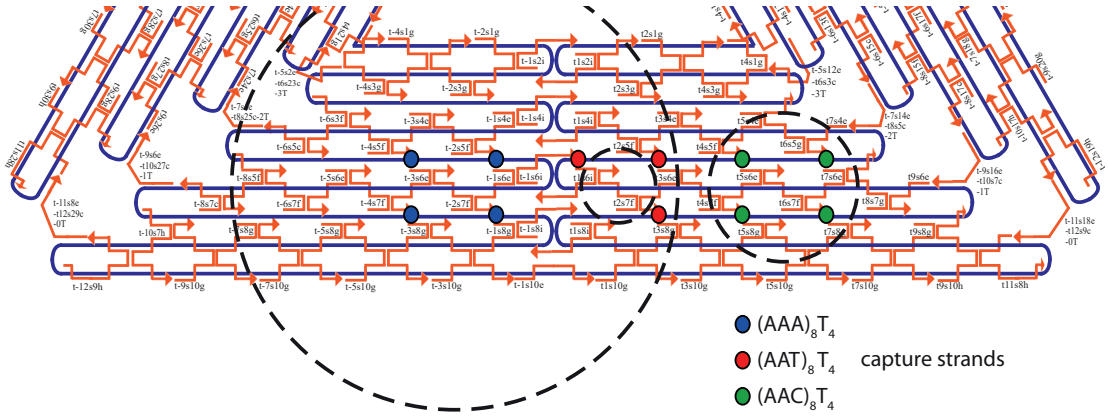

Figure 2.4.: Map showing the modified staple strands for design 20-10-60. Dashed lines indicate size and position of the nanoparticles to be bound. The scaffold strand is depicted as a blue line, staple strands as red arrows.

Design 20_b-10-60

This DNA origami scaffold design differs from the previous one only in the capture strands for the 20 nm nanoparticle (green in Figure 2.5). Here they are designed to protrude from the opposing face of the scaffold (i.e., *upwards* in Figure 2.5). Consequently, the 20 nm particle will not be bound on the same side as the 10 nm and 60 nm nanoparticle. This specificity is enabled by the intrinsic twist of the DNA helix: every 16 base pairs, the helix undergoes a one-and-a-half turn. Conveniently, staple strand ends are spaced at exactly 16 base pairs in the sharp triangle DNA origami scaffold, resulting in an alternating pattern of up- and down-pointing nicks and potential staple end modifications. This design principle can be disturbed by the occurrence of 'molecular threading', where a capture strand winds through holes in the DNA origami scaffold and protrudes on the opposite side.[110] This phenomenon is especially pronounced for DNA origami scaffolds adsorbed to a surface, with a high steric confinement on one side. For the nanostructures described in this thesis, two measures were taken to minimise threading effects: (i) nanolenses were assembled in solution, and (ii) for each nanoparticle at least three capture strands were placed on the DNA origami scaffold, making it more probable that a nanoparticle binds on the intended scaffold side even if one of the capture strands threads through to the other side. In design 20_b-10-60, slightly shorter recognition sequences ($(AAC)_5$ instead of $(AAC)_8$) are used for the capture strands binding the 20 nm particle, with the aim

to achieve a more precise localisation of those particles. Disadvantages in binding yield are not expected since no other particles that could impose steric stress are bound on this side of the DNA origami scaffold.

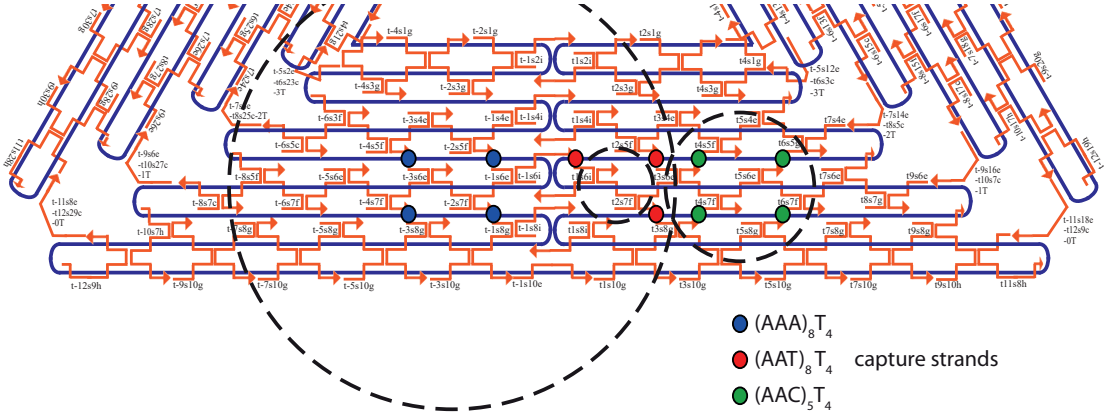

Figure 2.5.: Staple map with the modified staple strands for design 20_b-10-60. Dashed lines indicate size and position of the nanoparticles to be bound. The scaffold strand is depicted as a blue line, staple strands as red arrows.

Design 10-20-60

In this DNA origami scaffold design, the number of capture strands for binding the 60 nm particle is increased to five in order to raise binding yields and to account for the higher steric stress imposed by the adjacent 20 nm particle. For the same reason, the distance between the capture strand groups binding those particles (60 nm and 20 nm) is increased by 16 nm (see Figure 2.6, blue and red dots). As in the other designs, the capture strand group supposed to bind the 10 nm gold nanoparticle consists only of three strands. Here they are located at the end of the DNA origami scaffold (green dots in Figure 2.6). After addition of nanoparticles with the respective coating, this design will enable an overall arrangement in the order: 10 nm, 20 nm, 60 nm particle. All capture strands are designed to protrude on the same face of the DNA origami scaffold (i.e., *downwards* from the paper plane in Figure 2.6).

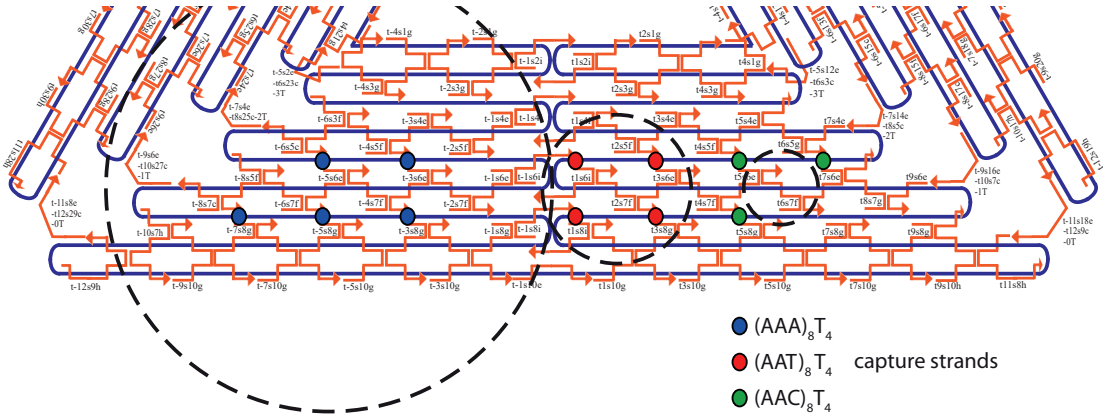

Figure 2.6.: Staple map with the modified staple strands for design 10-20-60. Dashed lines indicate size and position of the nanoparticles to be bound. The scaffold strand is depicted as a blue line, staple strands as red arrows.

Design 20-10-60 with biotin modification

The DNA origami scaffold can control the position of analyte molecules when respective binding functionalities are incorporated. To model such a case, a biotin-modified staple strand is included in design 20-10-60. See Figure 2.7 for a schematic. Biotin binds non-covalenty to the subunits of the tetrameric protein streptavidin (structural model in Figure 2.7, inset; mass ca. 52 kDa). Due to its very low dissociation constant ($K_d \approx 10^{-14}$ M)[169] the biotin-streptavidin interaction is a robust molecular recognition system that is widely used in molecular sciences.[170]

2.4. Streptavidin immobilisation

A solution of 2 nM biotin-modified DNA origami scaffolds and 20 nM streptavidin in 15 µl TAE-Mg is incubated for 2 h at room temperature. For process control by AFM, 1 µl of the resulting solution is deposited on a silicon chip (procedure described in Section 2.7 on page 41). Figure 2.8 shows AFM images of scaffolds before (A) and after (B) streptavidin addition. The DNA origami scaffolds with biotin-modified staples immobilise streptavidin with high binding yields. The conjugate solution is used for nanoparticle hybridisation without further purification, as described in the following Section 2.5.

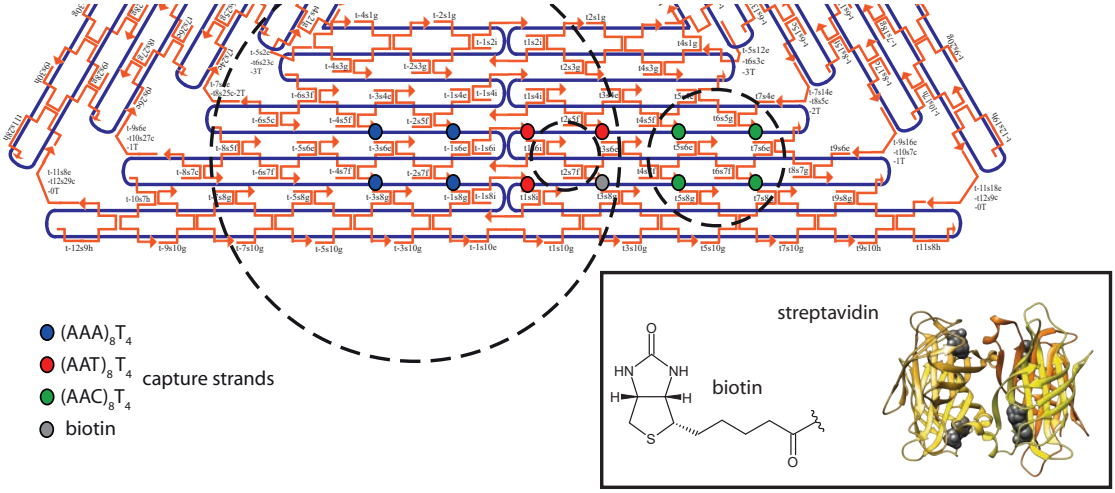

Figure 2.7.: Modified staple strands for design 20-10-60 with a single biotin modification. The scaffold strand is depicted as a blue line, staple strands as red arrows. The inset at the bottom right shows the structure of biotin and a ribbon representation of tetrameric core-streptavidin (yellow), binding four biotin molecules (grey).[171]

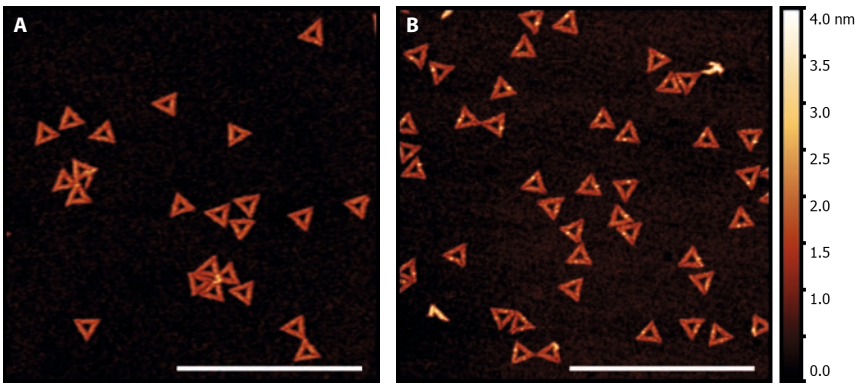

Figure 2.8.: DNA origami scaffold of design 20-10-60 with biotin, without (A) and with (B) one streptavidin bound per scaffold. Scale bars: 1 µm.

Streptavidin modification

Because of background signals observed in the SERS experiments, a modified variant of streptavidin is bound on the DNA origami scaffold. Streptavidin is reacted with propargyl-N-hydroxysuccinimidyl ester (P-NHS) in order to label its lysine side chains with alkyne moieties which give strong Raman signals that do not overlap with many others.[172] All of streptavidin's side chains face the solution and are easily accessible (Figure 2.9 A, red); for a reaction scheme see Figure 2.9 B. Monomeric streptavidin contains eight lysines and the full, tetrameric form 32, respectively. The modification procedure is as follows: 5 µM streptavidin is reacted with 2.5 mM P-NHS in 50 µl of 5 mM phosphate-buffered saline for 4 h. The solution is transferred to a 30 kDa MWCO centrifugal filter (Amicon Ultra, Millipore) and the buffer is exchanged by three successive cycles of TAE-Mg addition, centrifugation and filtrate removal. The residual is diluted to 100 nM and respective aliquots are stored at -20 °C.

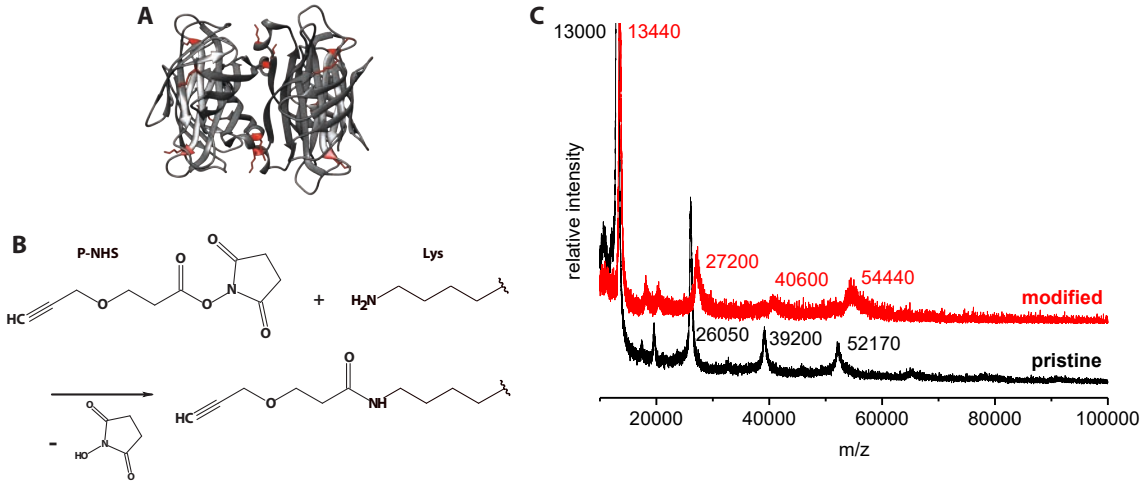

Figure 2.9.: (A) Structural model of the tetrameric core-streptavidin.[171] Side-chains only of lysine (red) are displayed. The unstructured terminal parts of the protein subunits are not included in the crystallographic data and thus are not shown. They contain four more lysines per monomer. (B) Reaction scheme of the alkyne modification of streptavidin's lysine residues. (C) MALDI-TOF MS data of the pristine and alkyne-modified protein. Spectra are normalised towards the tetramer peak and offset for clarity.

Matrix-assisted laser desorption/ionisation - time-of-flight mass spectrometry

The alkyne modification of streptavidin is confirmed by matrix-assisted laser desorption/ionisation - time-of-flight mass spectrometry (MALDI-TOF MS, conducted by Timm Schwaar and Ioana Abbas). For that purpose, the modified streptavidin solution is desalted by repeated centrifugation and water addition in a 10 kDa MWCO centrifugal filter (Amicon Ultra, Millipore). α-cyano-4-hydroxycinnamic acid matrix is freshly prepared (10 g/l in water/acetonitrile/trifluoroacetic acid, 33 %/66 %/0.1 %) and 0.75 µl of the matrix are spotted on a stainless steel MALDI target. 0.75 µl of the desalted, modified streptavidin solution (0.4 µM) and 0.75 µl of unmodified streptavidin in water (10 µM), respectively, are spotted on the matrix and dried with it. Samples are analysed in a Bruker Reflex III MALDI mass spectrometer (Bruker-Daltonik) with a nitrogen laser and 20 kV acceleration voltage in linear positive mode. Upon exposure to the MALDI laser, the tetrameric streptavidin is partly decomposed into its subunits, which is a known phenomenon for this protein ('first shot phenomenon').[173,174] The resulting spectra are displayed in Figure 2.9. The average m/z-shift per subunit observed for the modified protein is 512. Since one alkyne modification increases the molecular weight by 110, this shift relates to an average of 4.7 alkyne groups per streptavidin subunit and to ca. 19 alkyne groups on the full streptavidin, respectively. The overall labelling efficiency thus is 59 %.

2.5. Nanolens assembly

Figure 2.10 gives an overview of the nanolenses realised with the three different DNA origami scaffold designs. Silver nanoparticles are assembled only in the 20-10-60 geometry. Nanoparticles are bound to the DNA origami scaffold in several steps: The 10 nm particle is always immobilized first. In the second step, for 20-10-60 and 20_b-10-60 nanolenses, the 20 nm and 60 nm particles are added together, for 10-20-60 nanolenses they are added in consecutive steps, in that order. Table 2.1 on page 28 showed which nanoparticles with which DNA coating combinations are used for assembling the respective nanolens designs. For gold nanolenses, the first hybridization step is facilitated by a temperature ramp from 45 °C to 25 °C over a

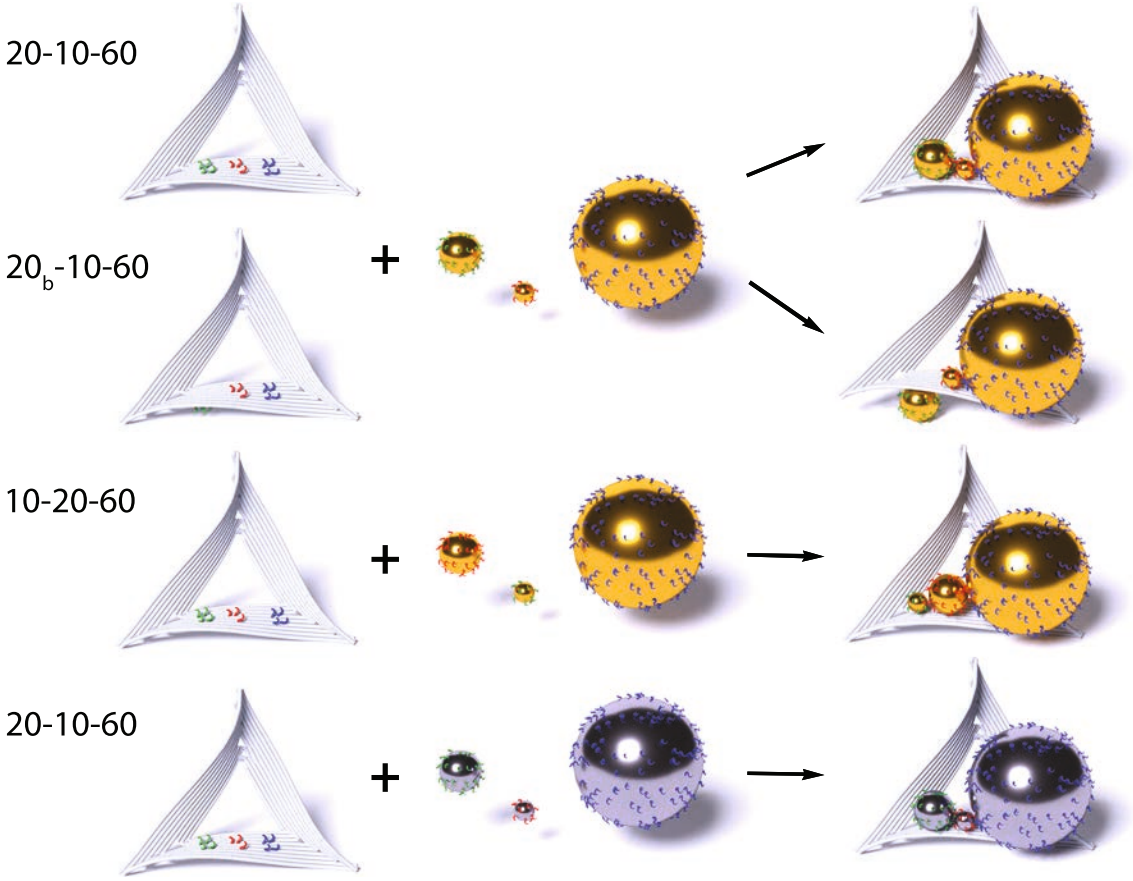

Figure 2.10.: Scheme illustrating which combinations of DNA-coated gold and silver nanoparticles and DNA origami scaffolds yield the respective nanolenses. Colour code for recognition sequences in the particle coating: **(GTT)$_3$**, **(ATT)$_3$**, **(TTT)$_3$**. The full coating strand sequences were given in Table 2.1 on page 28.

course of 71 min. In order to prevent the detachment of already bound nanoparticles, subsequent hybridization steps are performed by incubation at room temperature (90 min). For silver nanolenses, all steps are carried out at room temperature, with 90 min (first step) and 3 h (second step) incubation time, respectively. A ratio of 1:1 between DNA origami scaffold and the respective nanoparticles was found to show the best assembly yield. The stepwise hybridization enables process control by AFM. With binding yields of almost 100 % in the first hybridisation step, it is ensured that each nanolens includes one 10 nm nanoparticle, even if the particle cannot be visualised in the fully assembled nanolens anymore.

2.6. Gel electrophoresis

Unbound nanoparticles are removed by agarose gel electrophoresis in a Biorad Mini-Sub Cell GT electrophoresis chamber. For gold nanolenses, a two-layered agarose gel is applied, consisting of a bottom layer of 4 % agarose (20 ml) and a top layer of 1 % agarose (40 ml). Before injection into the freshly cast gel, 6x loading buffer is added to the sample so that the loading buffer is diluted by a factor of six. The gel is run at 60 V for ca. 1 h, with TAE-Mg as running buffer and cooling by an ice bath. Gold nanolenses are extracted from the gel by electroelution:[175] A pocket is cut in the top layer in running direction, just in front of the band containing the gold nanolenses. The pocket is filled with 20 % sucrose in TAE-Mg to slow down band migration. The bottom layer of the gel has the purpose to seal the pocket from one side. Voltage is applied again until the band of interest has migrated into the pocket and the thick solution is removed with a pipette. The sucrose-content is reduced by three cycles of TAE-Mg addition, centrifugation for 10 min at 400 rcf and supernatant removal. For silver nanolenses, a simpler extraction method, which does not require a two-layered gel, is applied. Here, samples are separated by a 1 % agarose gel (60 ml). The band of interest is cut out and placed onto a microscope slide wrapped in Parafilm M. A second Parafilm M-wrapped microscopy-slide is then used to squeeze the yellow nanolens solution out of the agarose slab. Two examples of gels run with gold and silver nanolenses are shown in Figure 2.11. Each sample was run in two parallel lanes to prevent smear associated with overloading.

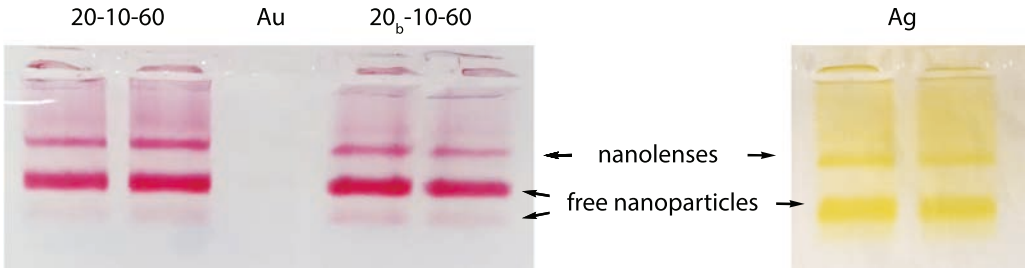

Figure 2.11.: Exemplary agarose gels with gold (left, 12.5 fmol loaded per well) and silver nanolenses (right, 8.2 fmol loaded per well). The major bands contain nanolenses and unbound nanoparticles, respectively. The nanolens designs are indicated in the superscript.

2.7. Deposition on silicon wafer

A polished silicon wafer (CrysTec, (100)-orientation, p-doped with boron) is cut into ca. 0.5 cm^2 squares and exposed to air plasma (Diener electronic Zepto ONE) for 5 min. In a subsequent cleaning step, substrates are washed with 4 ml of ethanol-water 1:1 solution and blow-dried with compressed air. 1 µl to 6 µl of sample solution are placed onto the silicon substrate and 30 µl 110 mM $MgCl_2$ 10x TAE buffer are added. The substrate is incubated for 1 h in a wet chamber, then washed with 4 ml ethanol-water 1:1 and blow-dried. The substrate is gently scratched at several positions with a diamond cutter. Since the scratches are visible in both, AFM and Raman mapping, they can be used as orientation points for spatially correlating the data from both techniques. Silicon is used for sample deposition and characterisation since it provides several advantages over mica, which is the more common substrate for AFM imaging: (i) Silicon gives few, sharp background signals in Raman imaging. (ii) DNA origami scaffolds adsorb more regularly on silicon, fewer artefacts and deformed DNA origami scaffolds are observed. (iii) Since the doped silicon surface is conductive, the same samples can also be analysed by SEM. (iv) Silicon is not as brittle as mica so that scratches can easily be placed, to be used as orientation marks for AFM-Raman correlation. A disadvantage of silicon compared to mica is that the sample incubation time for adsorption is 1 h instead of 5 min. Also, high magnesium concentrations are required (110 mM Mg^{2+} on silicon compared to 11 mM Mg^{2+} on mica), which can pose a problem for colloid stability and lead to aggregation during the adsorption process. Aliquots from all consecutive nanolens assembly steps are deposited on silicon substrates, thereby, an effective process control is

enabled. Exemplary AFM images for the assembly of 20-10-60 gold nanolenses are displayed in Figure 2.12.

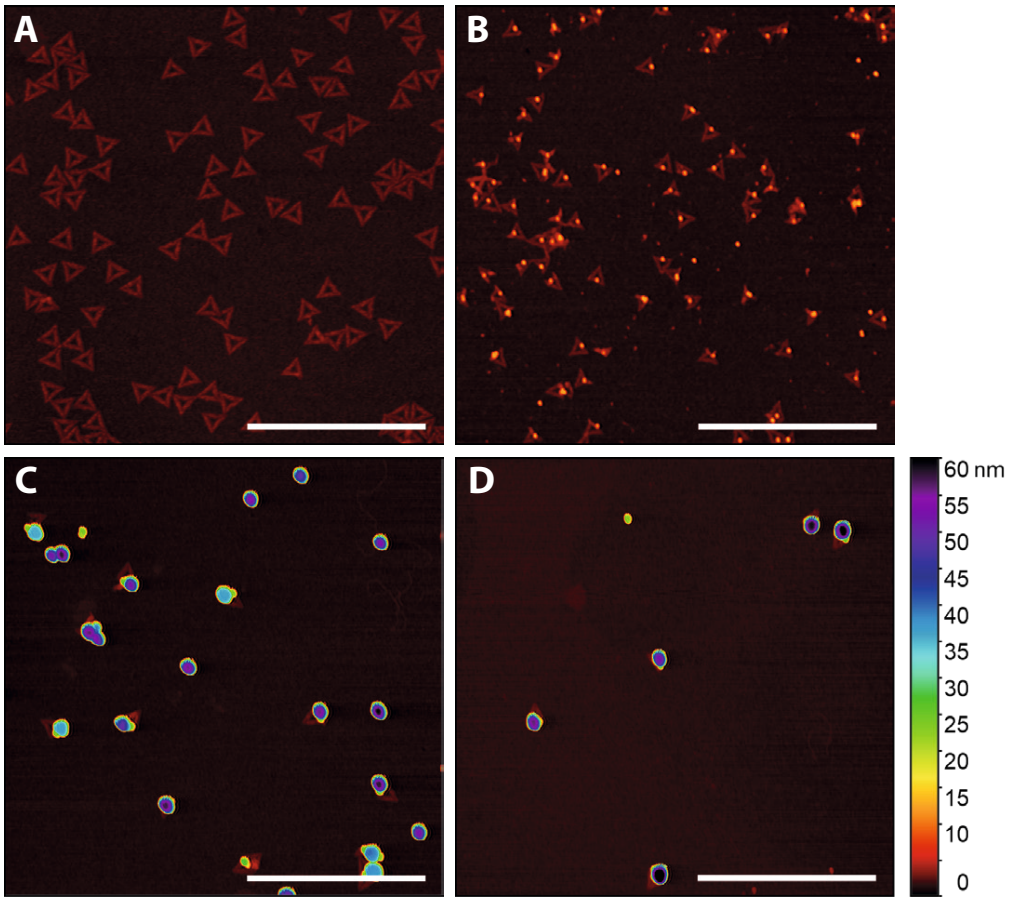

Figure 2.12.: AFM images illustrating the assembly steps for 20-10-60 gold nanolenses. (A) DNA origami scaffolds as synthesised. (B) DNA origami scaffolds after the first hybridisation step, with 10 nm gold nanoparticles. (C) 20-10-60 gold nanolenses as assembled, with unbound particles. (D) 20-10-60 gold nanolenses after gel purification. Scale bars: 1 µm.

2.8. Raman spectroscopy

Raman measurements are carried out on a WITec alpha300 confocal Raman microscope with a 100x Olympus MPlanFL N objective (numerical aperture 0.9) or a 10x Nikon EPlan objective (numerical aperture 0.25), with a 50 µm pinhole, 600 gr/mm grating and 532 nm excitation laser. For Raman scans with the 100x objective, typ-

ically, areas of $25\times25\,\mu m^2$ around the end of a scratch are scanned with 0.5 µm step size, 4 s integration time and 0.4 mW power at the sample, if not stated otherwise. The laser spot was estimated to be 1.3 µm wide.[1] For Raman scans with the 10x objective, areas of $170\times190\,\mu m^2$ are scanned with a 5 µm step size. These scans were carried out together with Yuya Kanehira. Silver nanolenses were measured after a system calibration, so that the absolute signal intensities should not be compared with the measurements from before. At an even later date, a new camera with an optional electron multiplying charge-coupled device (EMCCD) mode was implemented. It will be mentioned explicitly in the text if this camera mode was used instead of the conventional one. The laser spot of the 10x objective is estimated to be 10 µm wide. For single nanolens analysis, AFM and Raman mapping data are correlated in order to ensure that only SERS data from single nanolenses is obtained (*vide infra*). Table 2.2 gives an overview on eventually observed background signals; Table 2.3 translates the respective laser powers at the sample to power densities.

Table 2.2.: Background bands observed in Raman spectra.

Raman shift	**assignment**
$520\,cm^{-1}$	transverse optical phonon (TO) of silicon[176]
$930\,cm^{-1}$ – $1030\,cm^{-1}$	second-order TO of silicon[176]
ca. $1445\,cm^{-1}$	third-order TO of silicon[176]
$2330\,cm^{-1}$	gaseous N_2[177]

Table 2.3.: Conversion of power at the sample to power density.

objective	**power at the sample**	**power density**
10x	24 mW	$24\,kWcm^{-2}$
100x	0.4 mW	$24\,kWcm^{-2}$
100x	1.6 mW	$96\,kWcm^{-2}$
100x	2.8 mW	$168\,kWcm^{-2}$

[1] determined by Dr. Julia Prinz.

Estimation of enhancement factors

Enhancement factors for gold nanolenses (EF_{AuNL}) are determined with TAMRA as Raman reporter, placed in the coating of the 10 nm gold nanoparticles. TAMRA's fluorescence under 532 nm illumination prevents bulk Raman measurements of the non-enhanced dye, the estimation of EF_{AuNL} therefore is not straight forward. However, since enhancement factors for single 60 nm gold nanoparticles (EF_{AuNP}) are known from literature, EF_{AuNL} can be determined indirectly when gold nanolenses and TAMRA-coated, single 60 nm gold nanoparticles are measured under the same conditions. EF_{AuNL} then can be defined as:

$$EF_{AuNL} = \frac{I_{AuNL}}{I_{AuNP}} \frac{N_{AuNP}}{N_{AuNL}} EF_{AuNP}, \tag{2.1}$$

with I_{AuNL} – SERS intensity of strongest TAMRA band from a single gold nanolens, I_{AuNP} – average SERS intensity from single, TAMRA-labelled 60 nm gold nanoparticles (13.9 cts, $n = 14$), N_{AuNP} – number of TAMRA molecules on single 60 nm gold nanoparticles, N_{AuNL} – number of TAMRA molecules on single 10 nm gold nanoparticles (these are incorporated in the nanolenses), EF_{AuNP} – enhancement factor of single 60 nm gold nanoparticles (7.5×10^3).[178] It has to be noted that this value for EF_{AuNP} is only a rough estimate under the conditions used here: Zhu *et al.* reported it for 60 nm gold particles under 633 nm illumination. Under the conditions used here (closer to the plasmonic resonance, with 532 nm illumination), an increased EF_{AuNP} would be expected, according to calculations by Wang and Kerker larger by a factor of almost 10.[179] On the other hand, the enhancement factor determined by Zhu *et al.* is expected to contain contributions from chemical enhancement, which can account for a factor of 10 to 100.[180] For the TAMRA-coated particles, no chemical enhancement is expected since the dye molecules are bound on the solution-facing 5'-end of the coating strands, so the effective EF_{AuNP} in the measured system will be smaller. Weighing both influences, EF_{AuNP} is rather overthan underestimated. The electromagnetic enhancement of 10^3 predicted by Wang and Kerker for 60 nm particles under 532 nm excitation fits into this picture.[179] The resonance Raman contribution from TAMRA is not accounted for in the estimated EF_{AuNL} since it contributes to both, I_{AuNL} and I_{AuNP}. Assuming a similar influence in both systems, it cancels down in equation 2.1. The corresponding SERS spectra

from single TAMRA-labelled 60 nm gold nanoparticles that were used to extract I_{AuNP} can be found in Figure A.10 on page 108 of the Appendix. The observation of the latter was apparently enabled by TAMRA's resonance Raman contribution, without which the signal would have been too weak to be recorded.[181] In Section 2.2.3 it was described how N_{AuNP} and N_{AuNL} were determined by fluorescence spectroscopy.

Error estimation for enhancement factors

The error ΔEF_{AuNL} of EF_{AuNL} is determined by error propagation and reads as follows:

$$\begin{aligned}
\Delta EF_{AuNL} &= \left|\frac{dEF_{AuNL}}{dI_{AuNP}}\right| \Delta I_{AuNP} + \left|\frac{dEF_{AuNL}}{dN_{AuNP}}\right| \Delta N_{AuNP} + \left|\frac{dEF_{AuNL}}{dN_{AuNL}}\right| \Delta N_{AuNL} \\
&= \pm EF_{AuNL} \left(\left|\frac{\Delta I_{AuNP}}{I_{AuNP}}\right| + \left|\frac{\Delta N_{AuNP}}{N_{AuNP}}\right| + \left|\frac{\Delta N_{AuNL}}{N_{AuNL}}\right| \right) \\
&= \pm EF_{AuNL} \left(\left|\frac{12.8 \text{ cts}}{13.9 \text{ cts}}\right| + \left|\frac{264}{2988}\right| + \left|\frac{\Delta N_{AuNL}}{N_{AuNL}}\right| \right),
\end{aligned}$$

with ΔI_{AuNP} being the standard deviation of the SERS intensity measured for single TAMRA-coated 60 nm particles ($n = 14$). The errors for the number of TAMRA molecules on single 60 nm particles (ΔN_{AuNP}) and on the 10 nm particles of the gold nanolenses (ΔN_{AuNL}) are derived from error propagation calculations based on the linear regression data from the fluorescence measurements (Section 3.1). For 20-10*-60 and 20_b-10*-60 gold nanolenses this yields:

$$\Delta EF_{AuNL} = \pm EF_{AuNL} \left(\frac{12.8 \text{ cts}}{13.9 \text{ cts}} + \frac{264}{2988} + \frac{14.7}{99} \right) = \pm 1.16 \; EF_{AuNL},$$

and for 10*-20-60 gold nanolenses, respectively:

$$\Delta EF_{AuNL} = \pm EF_{AuNL} \left(\frac{12.8 \text{ cts}}{13.9 \text{ cts}} + \frac{264}{2988} + \frac{11.6}{39} \right) = \pm 1.31 \; EF_{AuNL}.$$

ΔI_{AuNP} is the main error contributor, its high variance is a typical phenomenon for SERS. ΔN_{AuNP} and ΔN_{AuNL} have a small, but not negligible influence on the overall error. Considering the large contributions of the other terms, the instrumental

error for the measurement of SERS intensity of a single gold nanolens (ΔI_{AuNL}) is neglected.

2.9. Atomic force microscopy

For AFM imaging, a Keysight Technologies AFM 5500 and a Nanosurf FlexAFM scanning probe microscope with a Nanosurf C3000 controller are used. The instruments are operated in tapping mode with Tap150Al-G cantilevers (BudgetSensors) with a force constant of 5 N/m and a resonance frequency of approximately 150 kHz. AFM data is processed with Gwyddion 2.48. Typical measurement parameters are a scan speed of 0.5 lines per second, a setpoint of 60 %, 512×512 pixels, and a P- and I-gain of 800. Since the maximal scan size of both microscopes is 10 µm×10 µm, many AFM images have to be combined in order to cover the area around the scratch where a Raman scan was carried out. An example of such correlation data is displayed in Figure 2.13. The Raman-AFM correlation on silver nanolenses for the streptavidin detection was measured together with Yuya Kanehira.

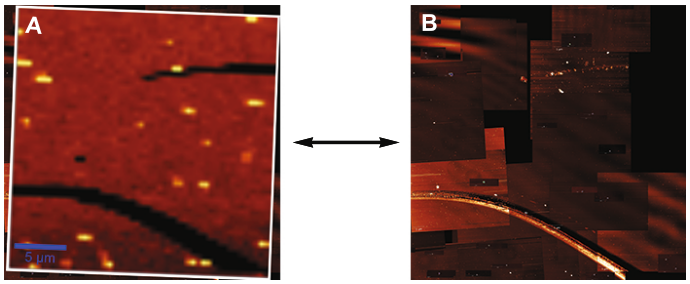

Figure 2.13.: (A) Map of Raman scan data collected around a scratch. The integrated signal intensity from 1150 to 2000 cm^{-1} is plotted, with bright colours indicating high intensities. (B) Combined AFM images around the scratch area.

2.10. Scanning electron microscopy

SEM measurements were carried out by Franka Jahn at the Leibniz Institute of Photonic Technology in Jena, on a Jeol JSM-6700F, with an accelerating voltage of 15.0 kV and a working distance of 7.1–7.2 mm.

2.11. Dark-field spectroscopy

Dark-field spectroscopy was conducted by André Dathe at the Leibniz Institute of Photonic Technology in Jena, on a Carl-Zeiss AxioImager.Z1 microscope in upright dark-field configuration. A 100x Carl-Zeiss LD EC Epiplan-Neofluar HD DIC objective with a numerical aperture of 0.75 and a 100 W halogen light source are used. Spectra from individual nanostructures are obtained with an optical fiber that is placed into the image plane of the microscope beam path. For detection, an external Princeton Instruments SpectraPro 2300i spectrometer with 150 gr/mm is used. Signals are integrated over 10 s and averaged over six acquisitions. The spectra are corrected by:

$$s_{corr} = \frac{s_{raw} - s_{bg}}{s_{lamp} - s_{dark}},$$

with s_{corr} – corrected spectrum, s_{raw} – raw spectrum, s_{bg} – background spectrum, collected from a position next to the respective nanolens, s_{lamp} – lamp spectrum and s_{dark} – dark spectrum. Spectra are further treated by a moving-average smoothing algorithm.

2.12. UV-Vis extinction spectroscopy

DNA and nanoparticle concentrations are determined with a Thermo Fisher Scientific Nanodrop200c spectrophotometer with an optical path of 1 mm. The respective extinction coefficients ε_λ used are listed in Table 2.4. Extinction spectra of nanolenses are measured directly after purification by gel electrophoresis. Measurements are done at least in triplicate and spectra are treated by a locally-weighted scatterplot smoothing (LOESS) algorithm.[182]

Table 2.4.: Extinction coefficients ε_λ at the wavelengths λ used in UV-Vis extinction measurements. The value for DNA origami scaffolds is based on an ε_{260nm} of 0.02 µl ng^{-1} cm^{-1} for double strand DNA[183] and a molar mass of 4.69 MDa for the DNA origami scaffold.

	gold nanoparticles[184]			**silver nanoparticles**[185]			**DNA origami**
	10 nm	20 nm	60 nm	10 nm	20 nm	60 nm	**scaffolds**
ε_λ in nM^{-1}cm^{-1}	0.103	1.031	39.63	0.556	4.18	73.9	0.0939
λ in nm	520	520	535	410	410	420	260

2.13. Finite-difference time-domain simulations

FDTD simulations are carried out with Lumerical FDTD Solutions 8.6.3. For gold nanoparticles with 19 nt-long coating strands, Thacker *et al.* have determined a coating thickness of 2.5 nm.[161] Assuming proportionality between layer thickness and strand length, for the 13 nt-long coating strands used here, a 1.7 nm coating thickness is modelled. The refractive index of the single-stranded DNA coating (1.7) is adopted from the same reference.[161] Since in Raman scattering, exciting and emitted light are wavelength-shifted and thus experience different enhancement, the electric field intensity enhancements at 532 nm (laser) and 583 nm (wavelength of the usually strongest TAMRA band, at 1650 cm^{-1}) are computed and multiplied. To achieve more accurate results for Rayleigh scattering simulations, substrate layers are included in those simulations. The surface layers are modelled with thicknesses of 2 nm (DNA origami scaffold), 2 nm (SiO_2 in silicon chip surface, as communicated by supplier) and an infinite layer of silicon below. Scattering cross sections from s- and p-polarized light are added incoherently to account for the unpolarised illumination of the dark-field setup. The materials' refractive indices are: DNA origami scaffold: 2.1, gold: as determined by Johnson and Christy,[62] silver, silicon and SiO_2: as determined by Palik,[186] surrounding medium: 1.0. The simulation volume is surrounded by a perfectly matched layer absorbing boundary, the mesh size is 0.25 nm in the plotted area. 3D models of the simulated systems are depicted in Figure 2.14.

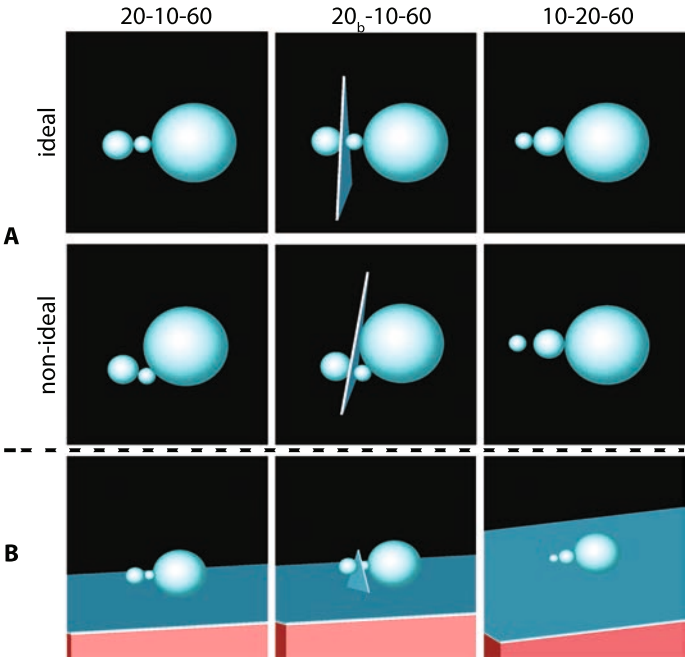

Figure 2.14.: 3D models used for simulations estimating: (A) electromagnetic enhancement, and (B) scattering cross sections. Colour code: blue – DNA, white – SiO_2, red – silicon.

3. Results

3.1. Nanoparticle coating

Coating protocols were developed that yield stable, DNA-coated gold and silver nanoparticles of a broad size range (10 nm–60 nm), within one to two days. In all protocols, the NaCl concentration is gradually increased. It was observed that the concentration range until 100 mM NaCl is most critical: Particle suspensions that showed no aggregation until this threshold concentration typically remained stable throughout the whole procedure. The following factors had the greatest influence on the success of a *gold* nanoparticle coating:

particle size Small particles will be more stable than large ones.

coating strand sequence $(TTT)_3$-T_4-SH strands yield the most stable gold nanoparticles, followed by $(GTT)_3$-T_4-SH and $(ATT)_3$-T_4-SH coating strands.

TAMRA modification of coating strands decreases particle stability significantly. Mixtures of TAMRA-modified and -unmodified strands can mitigate this effect.

The coating method that was used for most gold nanoparticles featured a steep increase of NaCl concentration in citrate buffer at pH 3. For one particle and coating strand combination (20 nm gold particles with TAMRA-$(GTT)_3$-T_4-SH), however, this method led to aggregation. Possibly the NaCl concentration raise (from 30 mM to 300 mM in one step) was too rapid for this system that has several of the restrictions indicated as critical above. Furthermore, it has to be considered that at reduced pH not just the inter-strand repulsion is attenuated, but also the surface adsorption of the nucleobases is affected. In the case of adenine, a reduced binding to gold was reported for low pH values,[187] what would result in less unspecific strand adsorption and actually be auxiliary for coating procedures with adenine-containing

strands. Meanwhile, it is unclear how the surface-adsorption of other nucleobases or TAMRA is affected upon protonation. In the case of the 20 nm gold particles with TAMRA-$(GTT)_3$-T_4-SH coating, a slow salt ageing protocol at neutral pH presented an apparently milder alternative that led to stable particles. In general it was more difficult to create particles with a high salt resistance when TAMRA-modified coating strands were used. Only with a mixture of TAMRA-modified and -unmodified strands it was possible to coat respective 20 nm and 60 nm gold nanoparticles. Two possible explanations for this behaviours are: (i) TAMRA, located at the solution-facing 5'-end of the coating strand, partially blocks the electrostatic shielding provided by the DNA coating. (ii) TAMRA adsorbs to the particle surface, similar to adenine, and thereby prevents high coating densities. The first is unlikely to be the case since coating strands with TAMRA at the 3'-end, close to the thiol, also showed a diminished stabilisation efficiency.[1]

For *silver* nanoparticles, the method at pH 3 also led to aggregation, so that a small-step salt ageing procedure at 40 °C (modified from ref. 153) was applied. The elevated temperature during coating putatively suppresses weak, unspecific DNA strand adsorption and favours the strong, covalent surface bond of the thiol groups. Tokareva *et al.* reported that strands with adenine are more suitable for coating silver nanoparticles than their thymine equivalents.[140] In the experiments presented here, not enough silver particle sizes and coating strand combinations were used to allow a judgement on the influence of the strand sequences. Still it is notable that even 60 nm particles could be coated with homo-thymine strands: This either speaks against the findings of Tokareva *et al.*, or for the robustness of the presented protocol. After coating, strands detached quickly from the silver nanoparticle surface, especially for 60 nm particles. The reason for this is the comparably weak Ag-S bond.[130] DNA strands with dithiolated head groups (DTPA-modified) were applied to lower the detachment rate on those particles.

For gold particles to be coated with adenine-rich strands, or for other challenging combinations that are prone to unspecific strand adsorption, reaction temperatures above 40 °C should be tested in the future. Additionally, introducing a stepwise pH 3 protocol, as presented by Zhang *et al.*,[188] combined with small-step salt ageing to high NaCl concentrations, or with magnesium salt in the final salt ageing step[164]

[1] oral communication by Dr. Julia Prinz

could prove beneficial. A strategy that was not explored here was to use small molecules other than BSPP to stabilise the particles and block unspecific DNA strand adsorption. Such helper molecules can be added after the DNA coating strands and fill the gaps between them. Notable examples include T_5-SH strands,[108] nonionic fluorosurfactants,[136] and mercaptohexanol.[189]

Determination of coating strand density

TAMRA-modified coating strands were replaced on the gold nanoparticle surface by dithiothreitol and the number of free TAMRA molecules in solution was determined by fluorescence spectroscopy. The TAMRA concentration was derived from the respective calibration curve (displayed in Figure 3.1), was multiplied by the respective dilution factor and divided by the initial gold nanoparticle concentration to yield the average number of TAMRA strands per particle (displayed in Table 3.1). Measurements were done in triplicate.

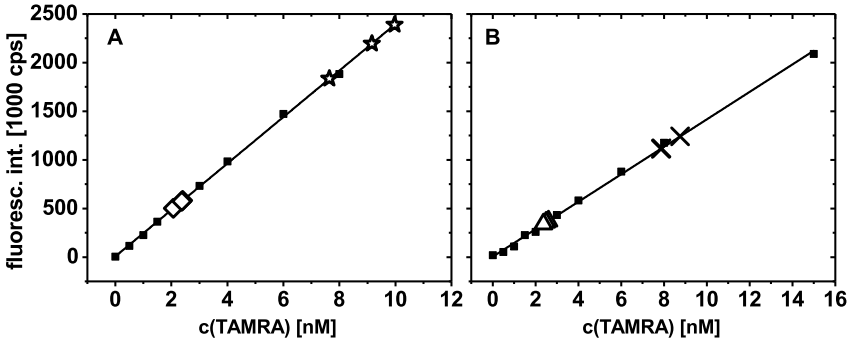

Figure 3.1.: Fluorescence data and calibration curves of TAMRA-DNA. For assignment of the data points refer to Table 3.1.
■ – Calibration values from known TAMRA concentrations.

Table 3.1.: Number of TAMRA-modified coating strands on the respective gold nanoparticles.

particle size	coating sequence	nanolens applied at	TAMRA-DNA per particle
☆ 10 nm	$(ATT)_3$-T_4-SH	20-10*-60/20_b-10*-60	99 ± 13
◊ 10 nm	$(GTT)_3$-T_4-SH	10*-20-60	39 ± 2
△ 20 nm	$(GTT)_3$-T_4-SH	20*-10-60	130 ± 6
✕ 60 nm	$(TTT)_3$-T_4-SH	20-10-60*	2988 ± 187

3.2. Preliminary experiments

Small gold nanoparticle assemblies on the way to functional gold nanolenses

In preliminary experiments, a number of different gold nanoparticle assemblies were prepared on DNA origami scaffolds, first with 5 nm, 10 nm and 15 nm gold nanoparticles, then with larger particles. Figure 3.2 gives an overview on the structures. The (preliminary) coating protocol that was used for the gold nanoparticles in Figure 3.2 A–D can be found on page 29 of the Methods. An efficient plasmon coupling between the particles requires small *relative* gap sizes. The length of the DNA coating strands and thus the coating thickness could not be decreased without compromising the assembly stability. Therefore, here the relative interparticle gaps were decreased by scaling up the particle sizes in a stepwise approach. The upper limit turned out to be determined by the stability of the medium-sized particle in the nanolenses. For

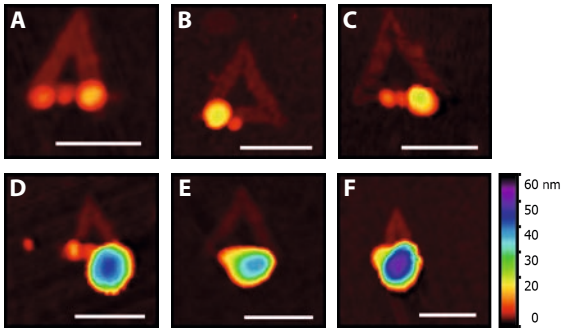

Figure 3.2.: AFM images of different complex gold nanoparticle aggregates that were assembled on DNA origami scaffolds en route to the nanolenses investigated in this thesis. (A) 10-5-15, (B) 20-5, (C) 10-5-20, (D) 10-5-40, (E) 20-5-40 and (F) 20-5-60; the numbers give the constituent nanoparticles' diameters. Scale bars: 100 nm.

this particle, coating strands with sequences other than homo-thymine (reserved for the largest particle) had to be used, which proved to be far less-efficient stabilisers. A further upper limit is defined by the onset of damping and quadrupole resonances in large particles that will lead to a decreased strength of the respective LSP coupling mode.[11] Also, a sufficient size ratio between the constituting nanoparticles (between two and three) has to be maintained.[41] As a compromise, further experiments were carried out with nanolenses from 10 nm, 20 nm and 60 nm nanoparticles.

Optimisation of capture strand number for small nanoparticles

DNA origami scaffolds with three or four capture strands at the central position were prepared and 5 nm particles hybridized to them. Figure 3.3 shows two of the resulting AFM images. The scaffolds with four capture strands have mostly bound two nanoparticles, the scaffolds with three capture strands mostly one nanoparticle. Therefore, the smallest nanoparticles in the nanolenses were immobilised by groups of three capture strands in the succeeding experiments. For particles larger than 10 nm—due to steric and electrostatic hindrance—no multiple binding was observed.

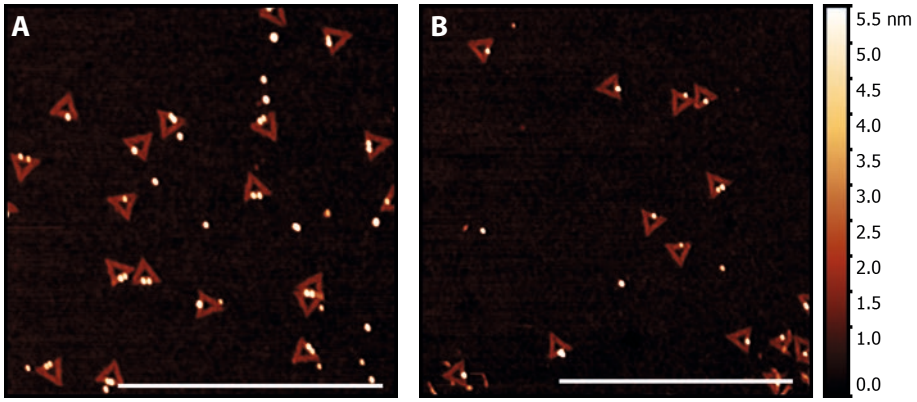

Figure 3.3.: AFM images of DNA origami scaffolds with 5 nm gold nanoparticles bound by (A) four or (B) three capture strands, respectively. Scale bars: 1 µm.

3.3. Gold nanolenses

Gold nanolenses from DNA-coated 10 nm, 20 nm, and 60 nm gold nanoparticles were assembled in the three different designs 20-10-60, 20_b-10-60, and 10-20-60. Representative AFM and SEM images are displayed in Figure 3.4. The AFM images show the 60 nm gold nanoparticles in purple and the 20 nm particles as yellow-to-green shoulders. The DNA origami scaffolds are visible as dark-red triangles beneath the particles. The 10 nm particles are typically not seen since they are difficult to be resolved in close vicinity to the larger particles. Still, the stepwise assembly with AFM imaging in-between ensured that each nanolens included one 10 nm particle

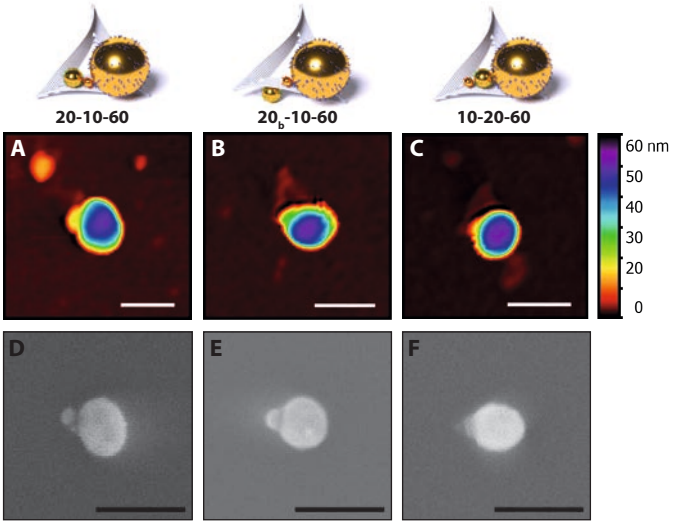

Figure 3.4.: (A-C) AFM and (D-F) SEM images of 20-10-60, 20_b-10-60, and 10-20-60 gold nanolenses. Scale bars: 100 nm.

(cf. Figure 2.12 on page 42). The nanolens assembly was also followed by UV-Vis extinction spectroscopy (Section 3.3.1). In order to compare the three designs regarding their electromagnetic enhancement, gold nanolenses were assembled where the respective 10 nm particles carried TAMRA as Raman reporter at the 5'-end of their coating strands. In the following, such TAMRA-labelled particles will be indicated by an asterisk in the nanolens nomenclature (20-10*-60, 20_b-10*-60, and 10*-20-60, respectively). The 10 nm particle mediates the last step in the nanolenses' enhancement cascade and thus is where the highest enhancement is expected. Twenty single gold nanolenses from each design were characterised in detail: SERS (Section 3.3.2) and dark-field scattering spectra (Section 3.3.4) were collected and complemented by FDTD simulations. Correlated Raman and AFM imaging confirmed that the signals originated from single nanolenses. For several nanolenses, information on the gap size could be inferred from SEM measurements. The complete set of AFM and SEM images can be found in the Appendix (Figures A.2–A.6, page 100ff.). In further experiments (Section 3.3.5), the enhancement in the different interparticle-gaps of the 20-10-60 gold nanolenses was probed by selectively labelling the 20 nm or 60 nm particles with TAMRA (giving 20*-10-60 and 20-10-60* gold nanolenses, respectively).

3.3.1. UV-Vis extinction spectroscopy

The UV-Vis extinction of citrate-stabilised 60 nm gold nanoparticles, DNA-coated 60 nm gold nanoparticles and of gold nanolenses was measured; representative spectra are displayed in Figure 3.5. A slight red-shift (by 3 nm, to 539 nm) was observed when the citrate-stabilised gold particles were coated with thiolated DNA, an effect that has similarly been reported for alkanethiols.[190] Mie theory accordingly predicts a red-shift for the addition of such a dielectric shell.[191] The extinction maximum of the gold nanolenses is further red-shifted (by 2 nm, to 541 nm). This shift is the result of an apparently only weak plasmon coupling between the gold particles that constitute the nanolenses. The observed red-shift underestimates the actual coupling strength since it represents an ensemble value: After gel purification, a mixture of full nanolenses and incomplete structures is present in solution. Extinction data was collected for 20-10-60 and 20_b-10-60 nanolenses, both showing the same maximum position. When 10-20-60 gold nanolenses were assembled, the reaction scale was too low to allow UV-Vis extinction measurements.

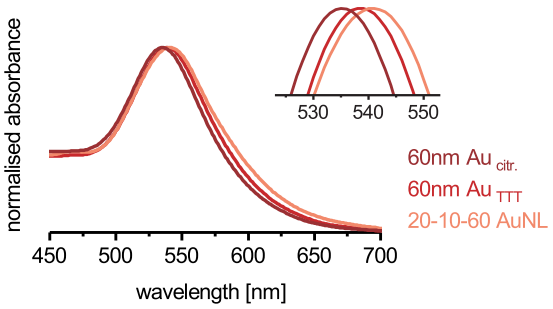

Figure 3.5.: UV-Vis extinction spectra of citrate-stabilised 60 nm gold nanoparticles (60 nm $Au_{citr.}$), DNA-coated 60 nm gold nanoparticles (60 nm Au_{TTT}), and gold nanolenses (20-10-60 AuNL). The inset gives a magnified view on the peak maxima.

3.3.2. Comparison of SERS signals from different gold nanolens designs

The average SERS spectra from the sets of twenty single gold nanolenses from each design are shown in Figure 3.6 (A–C, black). Also displayed are the spectra from the respective single nanolenses that gave the strongest SERS signal (red). The individual spectra from all structures can be found in Figure A.8 on page 106 of the Appendix. The average SERS spectra of the three designs differ in their intensity, with 20-10*-60 gold nanolenses showing the strongest average signal, followed by the 20_b-10*-60 ones, whereas 10*-20-60 gold nanolenses show the weakest average signal. The analysis of single gold nanolenses enables a close look at how differences in average SERS signals between the designs are constituted. The distributions of signal-to-noise ratios for the single nanolenses are displayed in the histograms of Figure 3.6 (D–F). The signal-to-noise ratio is chosen rather than the absolute intensity in order to account for the considerably varying magnitude of noise. Each design yields a majority of spectra with relatively low signals just around the limit

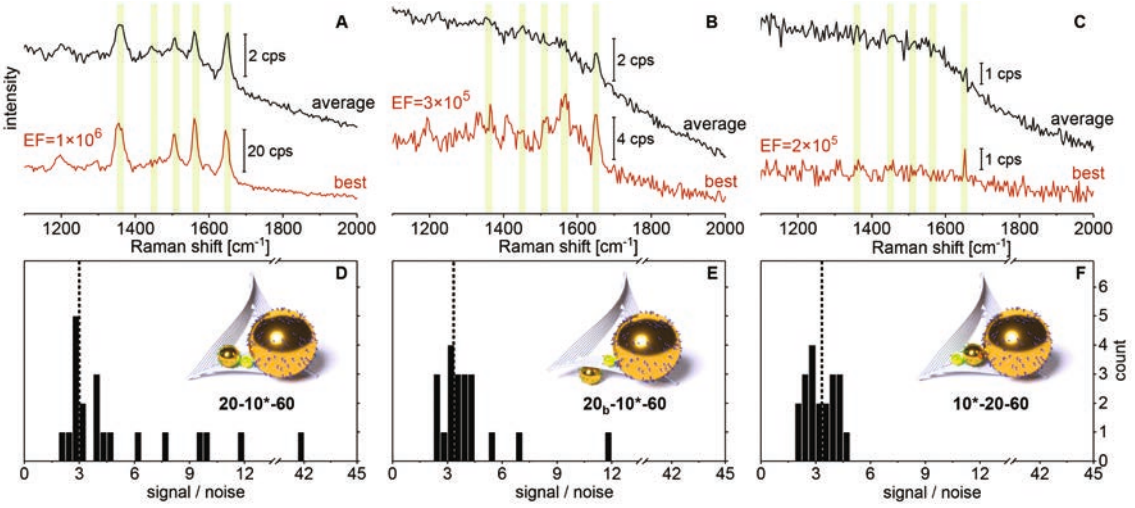

Figure 3.6.: (A–C) Average spectrum and most intense Raman spectrum obtained from each respective gold nanolens design: (A) 20-10*-60, (B) 20_b-10*-60, (C) 10*-20-60. Characteristic bands of TAMRA are highlighted in bright green. Spectra offset for clarity. (D–F) Distribution of signal-to-noise in the individual SERS spectra. The intensity of the most prominent TAMRA band of each respective spectrum is divided by the noise. The limit of detection is indicated by a dotted line.

of detection (determined by three times the standard deviation of the noise). The main difference between the three designs lies in the number and intensity of those spectra of relatively high intensity. Whereas six nanolenses of design 20-10*-60 yield a signal-to-noise ratio above six, for design 20_b-10*-60 only two individual nanolenses show SERS signals of similar intensity. For design 10*-20-60, none of the twenty examined nanolenses yields signals of this strength. The observed wide distribution of signal intensities, with a small number of strong emitters and many weak ones, is a characteristic phenomenon in SERS.[82] Its origin lies in the many factors that have to coincide for strong signal enhancements, such as the nanomorphology of the plasmonic substrate, the Raman scatterer position and orientation, and the incident light polarisation. The signal variations are expected to be slightly damped in the particular systems studied here: A theoretical study showed that by selectively labelling the smallest particle in the nanolens cascade, the statistical variation in enhancement factors can be narrowed down significantly, resulting in more-reproducible SERS signals.[35] The DNA origami scaffold exerts control on type, number and relative positioning of the plasmonic particles. But still, because of the (approximated) $|E/E_0|^4$-proportionality of the Raman scattered intensity, small changes in the plasmonic system can lead to high variations in signal intensity. For some structures, the gap size could be investigated by the help of the SEM images. They show that those nanolenses with a large inter-particle gap ($> 5\,\mathrm{nm}$) do not give a TAMRA signal above the detection limit. There are also nanolenses with apparently small inter-particle gaps and no TAMRA signal, but the SEM data does not allow to determine the exact size of such small gaps. Few-molecule spectroscopy as carried out here is a way to visualise the distribution of strong and weak Raman scatterers that is normally convoluted in those SERS spectra that originate from many plasmonic structures. For a detailed reproduction of such a distribution, the analysis of far more single nanolenses would be necessary—a laborious task with the current AFM-correlation procedure.

One 20-10*-60 gold nanolens showed a particularly strong SERS signal (Figure 3.6 A, red), relating to an enhancement factor EF_{AuNL} of 1.4×10^6. This EF_{AuNL} value could be underestimated because it is determined based on the total number of TAMRA molecules on the 10 nm particle. Only a fraction of these molecules is in the region where the local field is very high and therefore, the number of molecules that contribute to the strong SERS signal is expected to be consider-

ably smaller (up to a factor of 100, as there were estimated to be 99 ± 13 dye molecules on one particle). The resonance of the TAMRA molecules at the wavelength of the excitation laser (532 nm) contributes further to the observed SERS signal. The corresponding AFM, SEM and dark-field scattering data for this particular well-performing gold nanolens are displayed in Figure 3.7 A–C, together with a complimentary data set for a gold nanolens with low enhancement. The SEM data reveals why no SERS signal is observed for the latter: the 20 nm particle is separated off by a gap of approximately 10 nm, where no efficient plasmon interaction is expected. In the well-performing nanolens, the particle distance is too small to be determined from the SEM data. One has to be especially careful when inferring gap sizes between differently-sized particles from SEM data: The top-view perspective leads to underestimation of the distance. High-resolution transmission electron microscopy at a tilted angle would yield a more precise estimate.[192] The two structures in Figure 3.7 (C vs. G) show similar dark-field scattering spectra. Both spectra have a maximum around 565 nm and a shoulder peak around 650 nm. The dark-field scattering data and their correlation with SERS intensities will be discussed in Section 3.3.4.

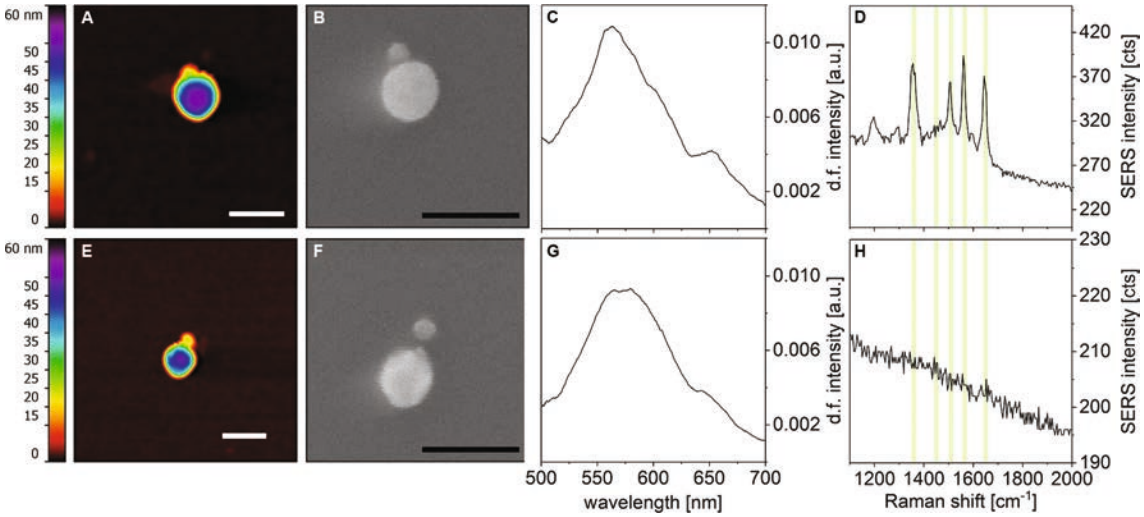

Figure 3.7.: (A) AFM, (B) SEM, (C) dark-field scattering and (D) SERS data for the 20-10*-60 gold nanolens with a particularly strong SERS signal. (E) AFM, (F) SEM, (G) dark-field scattering and (H) SERS data for a 20-10*-60 gold nanolens with low Raman enhancement. The SEM data shows a large inter-particle gap and explains the poor SERS performance of the latter. Scale bars: 100 nm.

3.3.3. Finite-difference time-domain simulations

In order to better understand the SERS behaviour of the different gold nanolenses, FDTD simulations with various particle arrangements were carried out. Figure 3.8 A–C shows the simulation results for the ideal cases, with particles touching and the centres of all particles located on a symmetry axis, like pearls on a tightened string. The maximal enhancement factors found in these simulations have the same order of magnitude as those estimated from the measurements: 10^6. The actual geometry of an individual nanolens might deviate from the ideal arrangement, since in the experiments reported here (i) the nanolenses are dried on the surface, (ii) the nanoparticles are assembled on a planar DNA origami scaffold, and (iii) the tethering capture strands allow for some flexibility and imply variation between individual nanolenses. Thus, further simulations demonstrate how the electric field enhancement is affected when gold nanoparticle positions are varied (Figure 3.8 D–F). The SERS enhancement of a nanolens then depends on how closely its structure matches the ideal collinear geometry of Figure 3.8 A–C. The relatively small enhancement observed for 10*-20-60 gold nanolenses (see Figure 3.6 C) can be explained by the flexibility of the 10 nm gold nanoparticle: In these nanolenses, the TAMRA-labelled 10 nm particle is free to move as far as the DNA tethers allow. The simulation shows that an additional 5 nm gap between 10 nm and 20 nm gold nanoparticle causes the SERS signal in 10*-20-60 nanolenses to drop by two orders of magnitude (Figure 3.8 C vs. F). For 20-10*-60 and 20_b-10*-60 gold nanolenses, on the other hand, the 10 nm particle is wedged between the larger particles and therefore not free to move. In these nanolenses, another distortion can occur: the centres of the spherical particles are expected to be not in a line when assembled on a perfectly flat surface (see schemes in Figure 3.8 D, E). The simulations show this to decrease the enhancement by one order of magnitude in the least favourable case. The initial idea for the 20_b-10*-60 nanolens was to optimize the geometry in a way that the DNA origami scaffold would lift the 10 nm particle into the plane between the 20 nm and 60 nm particles. However, the poor SERS performance of the design indicates that when dried on a surface, the scaffold is not sturdy enough to do so. Furthermore, 20_b-10*-60 gold nanolenses suffer from the additional DNA origami spacer separating the 20 nm gold nanoparticle. The strong SERS enhancement for some 20-10*-60 gold nanolenses indicates an optimal plasmonic coupling with a geometry close to

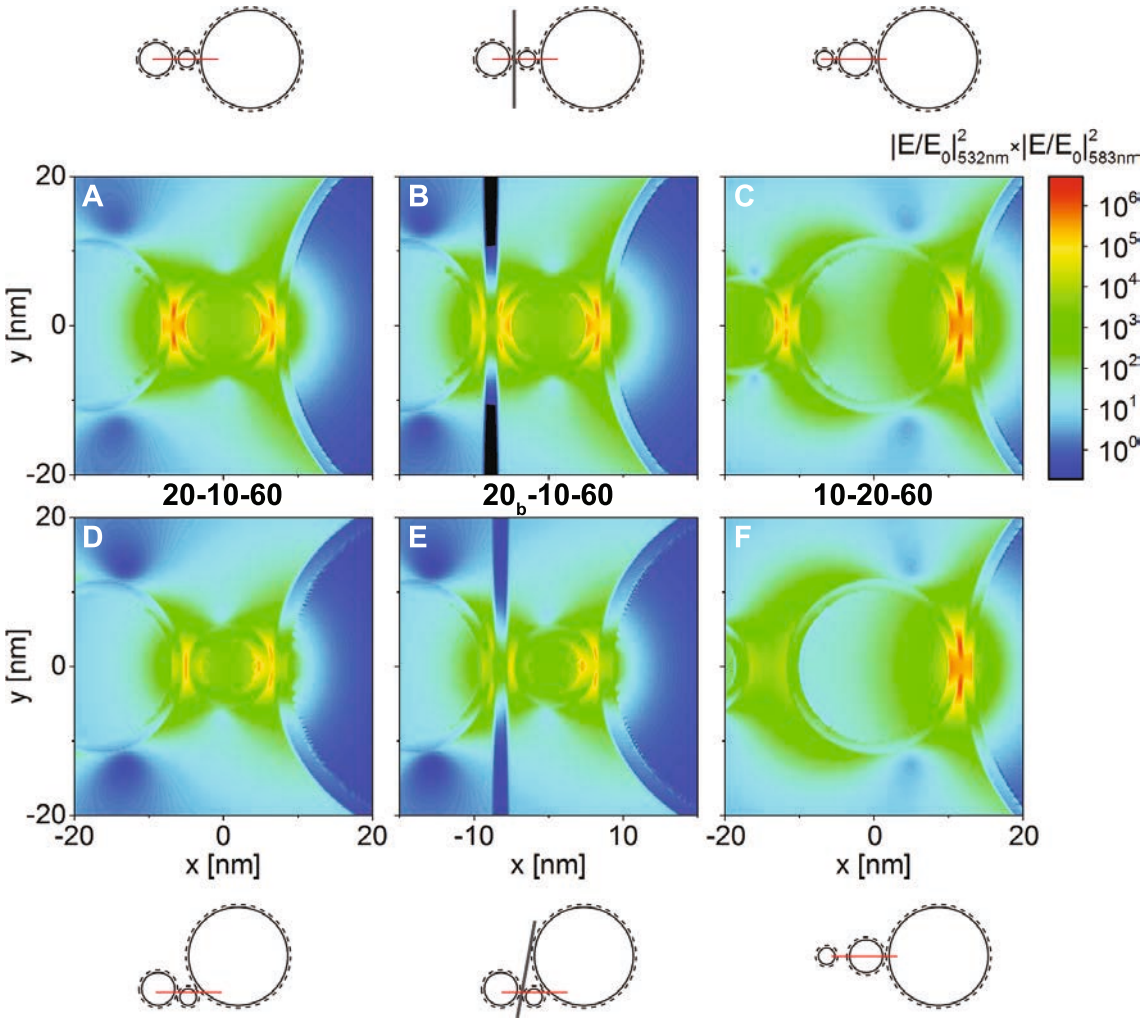

Figure 3.8.: Electromagnetic SERS enhancement of gold nanolenses, based on FDTD simulations of the local fields for the three designs at the excitation wavelength (532 nm) and at the wavelength corresponding to the TAMRA signal at 1650 cm^{-1} (583 nm). (A–C) in-line, no gap (D, E) out-of-line, (F) 5-nm-gap arrangement. The polarization direction of the incident light is along the longitudinal axis of the nanolenses. The red line in the schematics illustrates the plane of observation; the plane is chosen to intersect the position of greatest field intensity. The DNA origami scaffold separating the 20 nm gold nanoparticle in 20_b-10-60 gold nanolenses (B, E) is indicated in grey.

the one shown in Figure 3.8 A. In these cases, the structures might be benefiting from the relative flexibility of the single-layered DNA origami scaffold. Apart from misalignment, it was recently shown that the plasmonic response of the system can also be greatly influenced by the morphology of the individual gap.[192] Both effects are expected to contribute to the large signal fluctuations observed for the gold nanolenses.

3.3.4. Dark-field spectroscopy

Dark-field scattering spectra were collected for the sets of gold nanolenses examined in Section 3.3.2; the spectra are displayed in Figure A.9 on page 107 of the Appendix. Figure 3.9 A shows the extracted dark-field scattering maxima λ_{max} versus the SERS intensities of the respective gold nanolenses. There is no obvious correlation between them. Interestingly, the λ_{max}-distribution for the 20-10*-60 gold nanolenses is significantly narrower than those for the other nanolenses. At the same time, the 20-10*-60 gold nanolenses showed the strongest SERS signals. The medians of the λ_{max}-values for 20-10*-60 (567 nm) and 10*-20-60 (573 nm) gold nanolenses are indicated by dashed lines. The median for the 20_b-10*-60 gold nanolenses lies in-between (569 nm) and is not shown. These values indicate that the 532 nm excitation and 583 nm emission (of the strongest TAMRA band) in the SERS experiments were in

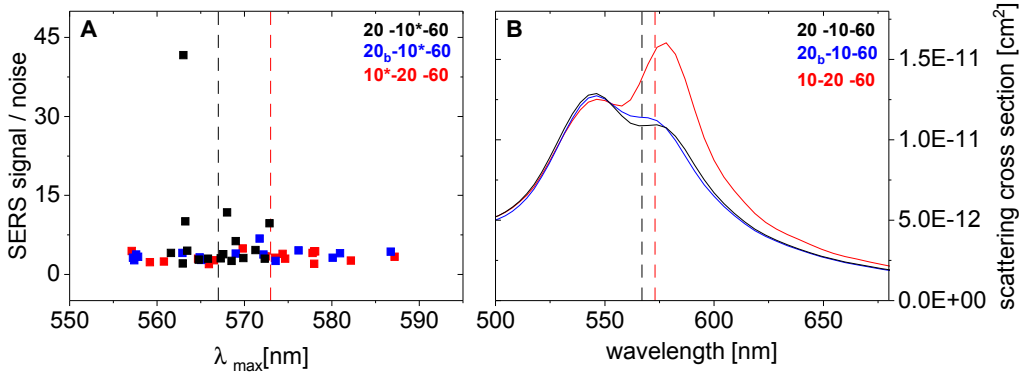

Figure 3.9.: (A) Correlation of the wavelength maximum λ_{max} of the dark-field scattering and the SERS signal/noise of the individual gold nanolenses. (B) Simulated Rayleigh scattering cross sections for the gold nanolens designs. The dashed lines in (A) and (B) indicate the medians of the experimental λ_{max}-distributions for 20-10*-60 and 10*-20-60 nanolenses, respectively.

good match with the plasmonic resonance. Though, the relation between Rayleigh scattering and electromagnetic Raman enhancement is not straight-forward, as emphasized by Moskovits in ref. 193. In the particular case here, there is a discrepancy because longitudinal and transversal coupling modes equally contribute to the dark-field spectra. In the SERS measurement, on the other hand, it is mainly the longitudinal mode that is responsible for the signal enhancement. Therefore, the optimal excitation and emission wavelengths for SERS will be slightly further in the red than suggested by the λ_{max}-values from the dark-field scattering. The experimental data match the scattering cross sections simulated by the FDTD method that are displayed in Figure 3.9 B. The stronger longitudinal coupling mode at 577 nm in the simulations for the 10-20-60 nanolenses is reflected in the red-shift of the respective experimental λ_{max}-median. It is caused by the smaller distance between 20 nm and 60 nm particle in these nanolenses.

Two exemplary dark-field spectra were displayed in Figure 3.7 on page 60; both spectra show a shoulder peak at ca. 650 nm that is not predicted in the simulations. The particles' LSPs can potentially interact with the underlying silicon substrate, and, due to the high refractive index of silicon, a red-shifted p-mode can be excited under the high angle of incidence used in the dark-field configuration.[17] It was reported that dark-field spectra of single gold nanoparticles on silicon substrates are dominated by this mode, with their λ_{max}-values even more red-shifted than those of particle dimers on the same substrate.[194] The excitation of such a surface-coupling mode would explain the shoulder peaks around 650 nm in Figure 3.7. It fits into the picture that the shoulder peak is observed in 3.7 C and G, at both, small and large interparticle-distance. In the simulations, the incident light vector was defined as perpendicular to the surface and therefore no such surface-coupling modes are excited and no peak around 650 nm is observed. Using a tilted incident angle for a broadband light source in this version of Lumerical FDTD Solutions is not straight forward and can lead to erroneous results.[195] In the SERS experiments, the coupling to the silicon is expected to be less pronounced, since for SERS, the full light cone illuminates the sample, whereas in the dark-field configuration, the sample is illuminated intrinsically only from a high angle of incidence.

When comparing the dark-field scattering spectra to the UV-Vis extinction data presented in Section 3.3.1, it has to be considered that both originate from nanolenses under different conditions: Dark-field scattering was recorded in air and with the

plasmonic structures placed on the silicon surface, therefore exposed to a different dielectric environment. Drying effects are further expected to influence particle distances and thus the plasmonic resonances. Especially the exposure to the high Mg^{2+} concentration (110 mM) during the drying process will lead to a decreased interparticle gap. As discussed, on silicon, surface-coupling modes in the red can be excited. Furthermore, the extinction data is a convolution of absorption and scattering, whereas in the dark-field configuration only scattering is detected. With all these influencing factors it is not surprising that the dark-field and UV-Vis extinction maxima do not coincide.

3.3.5. Comparison of SERS signals from different gaps

It is predicted that the electric field enhancement provided by nanolenses is strongest in the gap between the small and the medium-sized particle.[29,42] This is also reflected in the FDTD simulation results (see Figure 3.10 A, which represents the data already shown in Figure 3.8 A, but in a way that better visualises the difference between the gaps). This phenomenon is an intrinsic property of the cascaded field enhancement mechanism.

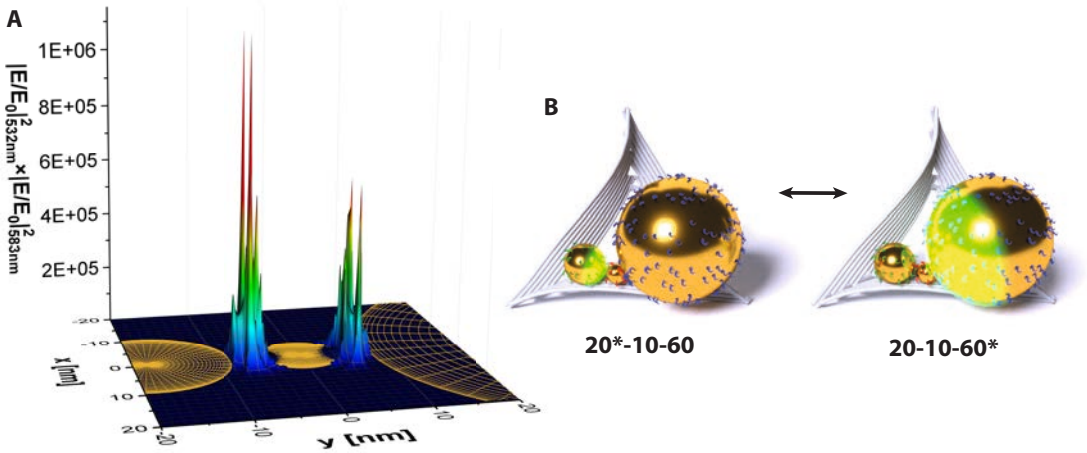

Figure 3.10.: (A) FDTD simulation result indicating the electromagnetic Raman enhancement of the two gaps in a 20-10-60 gold nanolens. The positions of the gold nanoparticles are shown by the golden wireframes.
(B) Illustration showing how the TAMRA coating of the *-marked gold nanoparticles leads to emission from only one of the two gaps (bright green).

Two studies demonstrated such a cascaded enhancement for gold nanolenses by comparing their field enhancement with that of respective heterodimers. Kravets *et al.* used randomly placed dye molecules to study the overall enhancement of the structures,[43] and Höppener *et al.* probed the enhancement at the external border of a gold nanolens.[49] Neither of them selectively probed the field enhancement in the internal gaps of a nanolens. The DNA origami-based approach enables not just the bottom-up assembly of nanolenses, but also the selective incorporation of probe molecules and thus to distinguish the internal nanogaps and their enhancement contribution. In order to selectively probe either one of the gaps, experiments with 20-10-60 gold nanolenses were carried out where either the 20 nm (20*-10-60), or the 60 nm (20-10-60*) gold nanoparticles were TAMRA-labelled. See Figure 3.10 B for a schematic illustration. In this way, the Raman signal originates only from one of the two gaps and the respective local enhancements can be compared. SERS spectra from seventeen single 20*-10-60 gold nanolenses and eleven single 20-10-60* gold nanolenses were measured and the intensity of the strongest TAMRA signal in each spectrum was determined. The spectra are displayed in Figure A.11 on page 108 of the Appendix, the corresponding AFM images in Figure A.12 on page 109. The SERS signal intensity depends on the number of TAMRA molecules in the gap. Since nanoparticles of different size support different densities of dye molecules on their surface, signal intensities have to be normalised when two individual gaps are compared. The SERS signal intensity I_{AuNL} is divided by the density of TAMRA molecules on the respective gold nanoparticle, assuming that the SERS signal is proportional to the number of dye molecules in the area of highest enhancement and that for both gaps these areas share similar size:

$$I_{AuNL,d} = \frac{I_{AuNL}}{N/(\pi d^2)} \,, \tag{3.1}$$

with $I_{AuNL,d}$ – TAMRA density-normalised SERS signal intensity of the nanolens, N – number of TAMRA strands on the coated gold nanoparticles (2988 for 60 nm particles, 130 for 20 nm particles, as determined on page 53), and d – particle diameter. The resulting average $I_{AuNL,d}$ for the 20*-10-60 nanolenses is approximately 30 % higher than that for the 20-10-60* ones (see Table 3.2).

When the incident light is polarized parallel to the longitudinal axis of the nanolens, the regions of high fields are located in the gaps between the particles.

Table 3.2.: SERS signals from gold nanolenses with TAMRA-labelled 20 nm or 60 nm gold nanoparticles. The SERS signal from single nanolenses (I_{AuNL}) is normalised for TAMRA density ($I_{AuNL,d}$) and for signal contribution from isolated, TAMRA-labelled gold nanoparticles ($I_{AuNL,d,i}$).

	20*-10-60	**20-10-60***
average I_{AuNL} [cts]	8.9 ± 5.7	17.3 ± 11.4
$I_{AuNL,d}$ [cts nm^2]	86	65
$I_{AuNL,d,i}$ [cts nm^2]	68	12

For light polarized perpendicular to the longitudinal axis, mainly transverse modes are excited that provide field enhancements similar to single-particle modes.[68,196] Under the illumination used in the experiments presented here, both, longitudinal and transverse modes are excited. Therefore, also the enhancement contributed by the whole nanoparticle surfaces, apart from the gaps, must be taken into account. This is achieved by subtracting the average normalised SERS signals of TAMRA-coated, isolated nanoparticles of the respective size from the signal obtained with the nanolenses:

$$I_{AuNL,d,i} = I_{AuNL,d} - I_{AuNP,d} \ , \tag{3.2}$$

with $I_{AuNL,d,i}$ – isolated-particle-corrected SERS intensity of the nanolens, $I_{AuNP,d}$ – density-normalised SERS intensity of strongest TAMRA band from isolated gold nanoparticles (53 cts nm^2 for 60 nm particles (n=14), 18 cts nm^2 for 20 nm particles (n=11)). The spectra from the single particles are shown in Figure A.10 on page 108 of the Appendix. For the TAMRA-coated single 20 nm particles, the Raman enhancement was too weak and no characteristic TAMRA bands were observed. Thus, as a conservative estimate, the magnitude of the noise was used for correcting the signal from the 20*-10-60 nanolenses. As this correction term is an upper-limit value that is subtracted, the signal from the 20*-10-60 nanolenses could be underestimated. Accordingly, the cascading effect would be underestimated in the current calculation. With the second normalisation, the difference in SERS intensity between the gaps increases considerably: the signal $I_{AuNL,d,i}$ from the gap between 20 nm and 10 nm gold nanoparticle is approximately six times higher than that from the other gap (see Table 3.2). This matches reasonably with the FDTD simulation result, which predicts a factor of two (Figure 3.10 A). The nanolens in this simulation featured a 3.4 nm gap of DNA coating between the metal surfaces; with smaller gap

sizes, larger factors were predicted. The large fluctuations of the signal intensities I_{AuNL} are a characteristic SERS feature and render the data interpretation difficult. In spite of the relatively low number of analysed nanolenses, these results provide the first experimental indication that the gap between medium and small nanoparticle in nanolenses provides stronger field enhancement than that between the large and the small nanoparticle.

3.4. Silver nanolenses

Silver experiences less LSP damping in the visible than gold and thus is seen as the better plasmonic material for many applications. Accordingly, stronger SERS signals are potentially accessible for silver nanolenses. They were assembled only in the 20-10-60 geometry, as this had shown the best performance in the experiments with the gold nanolenses. In the first syntheses, the silver nanolens assemblies suffered from low yields; especially the 60 nm silver nanoparticles did not bind well to the DNA origami scaffold. The cause for this was a rapid coating strand detachment, so that stronger-binding dithiol coating strands in combination with an additional purification step before hybridisation could resolve the issue. Figure 3.11 shows a schematic and an AFM image of successfully assembled silver nanolenses.

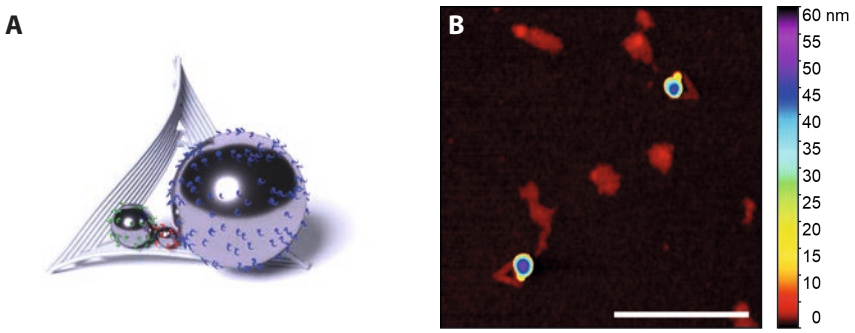

Figure 3.11.: (A) Schematic of an assembled silver nanolens. (B) Exemplary AFM image of two silver nanolenses. As for the gold nanolenses, the 60 nm particle is seen as a purple spot, the 20 nm particle as a yellow shoulder. The underlying DNA origami scaffold is dark red. Scale bar: 500 nm.

3.4.1. UV-Vis extinction spectroscopy

UV-Vis extinction was measured for citrate-stabilised 60 nm silver nanoparticles, DNA-coated 60 nm silver nanoparticles and silver nanolenses. The respective data are displayed in Figure 3.12. Interestingly, when the citrate-stabilised 60 nm silver particles were coated with the thiolated DNA, their extinction maximum *blue*-shifted from 437 nm to 416 nm. This significant shift is opposite to what would be expected from Mie theory, which predicts a red-shift for particles that are coated with a dielectric layer (as observed for the gold particles, that showed a 3 nm red-shift, cf. Figure 3.5, page 57). Considering the several-hour coating procedure at 40 °C, the blue-shift observed here could result from a temperature annealing that smoothes out edges and renders the particles more spherical. However, no resonance shift was observed in a control experiment with 60 nm citrate-stabilised silver particles that were kept at 40 °C for one day. Instead, the surface chemistry of the silver particles yields a possible explanation: A study with alkanethiols of different lengths indicated that for *short* alkanethiols (≤ 3 carbons), a blue-shifted plasmon resonance is to be expected.[197] The authors reason that this could be caused by an increase in electron density on the silver particle surface due to the charge-transfer nature of the Ag–S bond. At longer chain lengths (> 3 carbons), the increasing thickness of the dielectric coating layer dominates. These conclusions were drawn from extrapolation of data for long alkanethiols, but an actual blue-shift in the plasmon resonance has also been experimentally reported, for SH^- binding to colloidal silver.[198] There, a

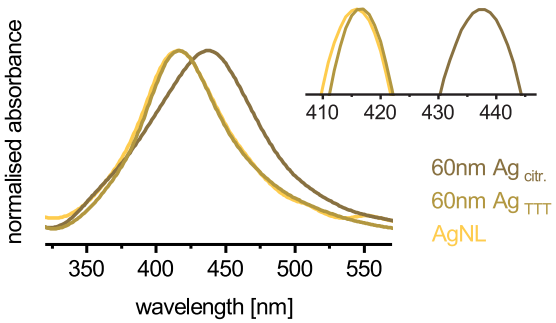

Figure 3.12.: UV-Vis extinction spectra of citrate-stabilised 60 nm silver nanoparticles (60 nm $Ag_{citr.}$), DNA-coated 60 nm silver nanoparticles (60 nm Ag_{TTT}), and silver nanolenses (AgNL). The inset gives a magnified view on the peak maxima.

blue-shift of up to 10 nm was measured, which was reversed under high SH^- concentrations. Possibly the blue-shift observed here can be attributed to the same effect. The DNA coating with its estimated thickness of 1.7 nm is considerably thicker than the monolayers of these studies. But due to the DNA's steric and electrostatic constraints, it might not be as densely packed as the alkanethiols. Additionally, the 60 nm silver particles were coated with *di*thiol-modified DNA strands, enforcing the electron-donating effect per strand. For gold particles, no such effect is expected, due to the more covalent nature of the Au–S bond.[130] Another hypothesis is that the original citrate-stabilised stock suspension is actually a mixture of single and aggregated particles, the latter of which are either lost or disassembled during the coating procedure. This is supported by the larger full width at half maximum of the peak from the citrate-stabilised particles.

Upon assembly of the DNA-coated silver nanoparticles to silver nanolenses, only a minuscule wavelength shift (< 1 nm) relative to the DNA-coated 60 nm particles is observed, which is within the range of error for these measurements. The absence of a strong red-shift upon silver nanolens formation indicates that—in solution—there is only a weak coupling between the constituent particles' LSPs. The electrostatic repulsion, mitigated by only 11 mM Mg^{2+}, and the steric requirements of the hydrated DNA coating, likely keep the negatively charged particles apart. During the assembly of the gold nanolenses, also only a small red-shift (2 nm) was observed. If in-solution measurements were to be carried out with DNA origami-based nanolenses in a future application, higher-ionic strength buffers or an alternate coating approach were advisable. It fits into this picture that SERS measurements with nanolenses in solution (not shown in this work) were mostly unsuccessful.

3.4.2. Finite-difference time-domain simulations

FDTD simulations were carried out for silver nanolenses with an ideal, collinear particle arrangement. As for the gold nanolenses, the field intensity enhancement at 532 nm was multiplied with the one at 583 nm (1650 cm^{-1}) in order to achieve a more realistic estimation of the enhancement of respective Raman signals. A plot of the resulting enhancement in the plane of the symmetry axis is shown in Figure 3.13 A. The maximal electromagnetic enhancement of the Raman signal is located at the crevices between the 10 nm and the 20 nm particles. It is only slightly higher than that from

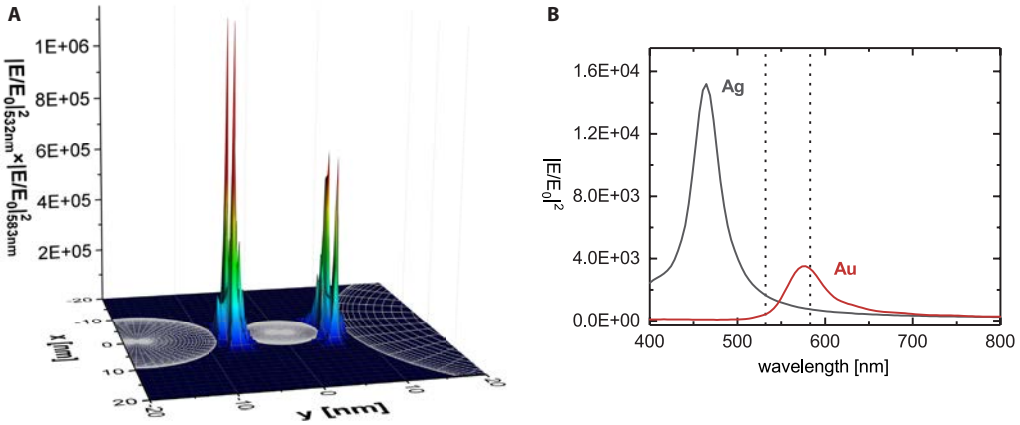

Figure 3.13.: (A) FDTD simulation result for a silver nanolens with an ideal collinear particle arrangement (all particle centres on a straight line). The positions of the silver nanoparticles are shown by the grey wireframes. (B) Maximal electromagnetic field enhancement versus the excitation wavelength, simulated for silver and gold nanolenses in the ideal collinear 20-10-60 geometry. The dotted lines indicate the wavelengths used for the simulation under (A).

the respective gold nanolenses (1.19×10^6 for silver vs. 1.13×10^6 for gold). This result can be understood with a look at the wavelength dependence of the maximal field enhancement provided by the gold and silver nanolenses, as it is displayed in Figure 3.13 B. The silver nanolenses excel at wavelengths below 550 nm, but above that, the gold nanolenses show the higher field enhancement. For excitation at 532 nm and emission at 583 nm (Figure 3.13 B, dotted lines) both structures yield comparable results. FDTD simulations were also run for a distorted silver nanolens geometry, where the particles are arranged out-of-line, as if lying on a sur-

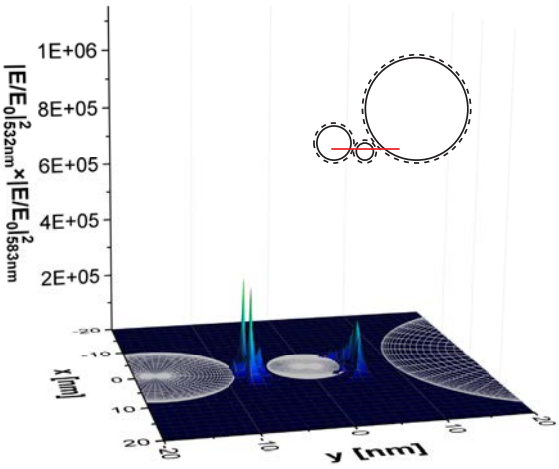

Figure 3.14.: FDTD simulation result for a silver nanolens with an out-of-line particle arrangement (all particles lying on a flat plane). The positions of the silver nanoparticles are shown by the grey wireframes. The plotted area is indicated by a red line in the inset schematic.

face. A plot of the resulting data is shown in Figure 3.14. In this adverse geometry, the maximal electromagnetic Raman enhancement decreases by a factor of approximately four (from 1.19×10^6 to 3.05×10^5). This decrease is similar to the one that was observed for the respective gold nanolenses under the same deformation. Overall, these simulation results show that under the conditions here, silver nanolenses not necessarily are the better plasmonic substrates. However, under the right conditions they can outperform analogous gold nanolenses. This could be realised by either shifting the plasmon resonance to the red (larger particles, a higher-refractive index medium such as water), or by excitation with a respective blue laser line.

3.4.3. Surface-enhanced Raman spectroscopy

In most sensing applications, the analyte does not exhibit Raman enhancement through a molecular resonance, as it was exploited when TAMRA was used as a Raman reporter in the SERS experiments with the gold nanolenses. In order to simulate a more practical sensing application with the silver nanolenses, a protein served as a non-resonant, biologically more relevant model analyte. As such, streptavidin was used, since it is well characterised and easily incorporated into the self-assembly design: It builds a strong, non-covalent bond to the small molecule biotin (shown in Figure 2.7 on page 36). One of the advantages of the DNA origami platform is that it allows the exact positioning of such molecules. A single biotin, and consequently a single streptavidin, was placed between the 20 nm and 10 nm particle of a silver nanolens. Figure 3.15 shows an illustration of a thus-resulting assembly. The unambiguous detection of pristine streptavidin in single silver nanolenses

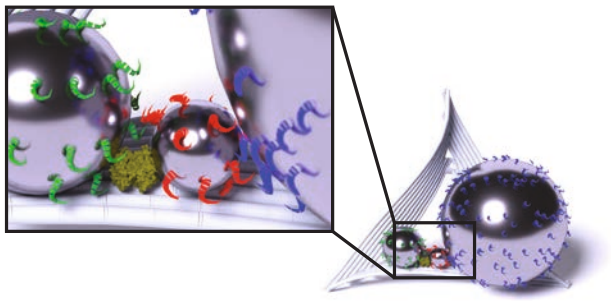

Figure 3.15.: Illustration of a single streptavidin molecule (dark yellow) bound within a silver nanolens.

was complicated by intense, fluctuating SERS spectra in the fingerprint region of the protein (their nature being discussed further below). Therefore, streptavidin was modified with alkyne groups, which give Raman signals at frequencies where only a few other signals appear. This property enables alkynes to be used as Raman tags even in such a crowded and chemically diverse environment as a living cell.[172] For the experiments discussed here, streptavidin was successfully modified with an average of 19 alkyne groups on the full tetrameric protein, as determined by MALDI-TOF MS. Its biotin affinity was apparently not compromised by these modifications: Streptavidin could still be immobilised with high yields on the DNA origami scaffolds (see Figure 2.8 on page 36 of the Methods). In a monosubstituted alkyne, the band for the C≡C stretching vibration is expected between 2100 cm^{-1} and 2150 cm^{-1}.[177] Unfortunately, the available amount of protein did not suffice for a non-enhanced Raman control experiment with the alkyne-modified streptavidin, which would have purveyed the spectral position of the alkyne stretch vibration in this particular chemical environment. Instead, Raman spectra of the P-NHS that was used to modify streptavidin were acquired. They are displayed in Figure 3.16 A. The characteristic stretch vibration of the alkyne group was observed at 2128 cm^{-1} for solid P-NHS, and at 2121 cm^{-1} for P-NHS in aqueous solution. The alkyne signal in the nanolenses is accordingly expected around 2121 cm^{-1}. Despite the high degree of structural control provided by the DNA origami assembly, SERS signal intensities can still vary significantly, as demonstrated by the gold nanolenses in Section 3.3.2.

In order to find silver nanolenses with a strong-enough field enhancement for detection of the single streptavidin, an iterative Raman mapping approach was followed: At first, a large area of $170 \times 190\,\mu m^2$ was scanned with the 10x objective. Due to the large laser spot size of $\sim 10\,\mu m$, several nanolenses would always be in focus. Then, around those positions where an alkyne signal was detected, high resolution scans with the 100x objective were carried out. In these scans, the spot size is smaller (1.3 µm) and in most cases only single plasmonic structures have contributed to the observed signal. The exact point of origin of the alkyne signal is located in the scan data and correlated AFM imaging then ensures whether the signal can be attributed to a single silver nanolens. Figure 3.16 B shows a respective data set where the alkyne signal at 2120 cm^{-1} was observed in both, the low- and the high-resolution scan. As AFM confirmed that only a single nanolens was present, it can be concluded that alkyne reporter groups from a single protein were detected in this

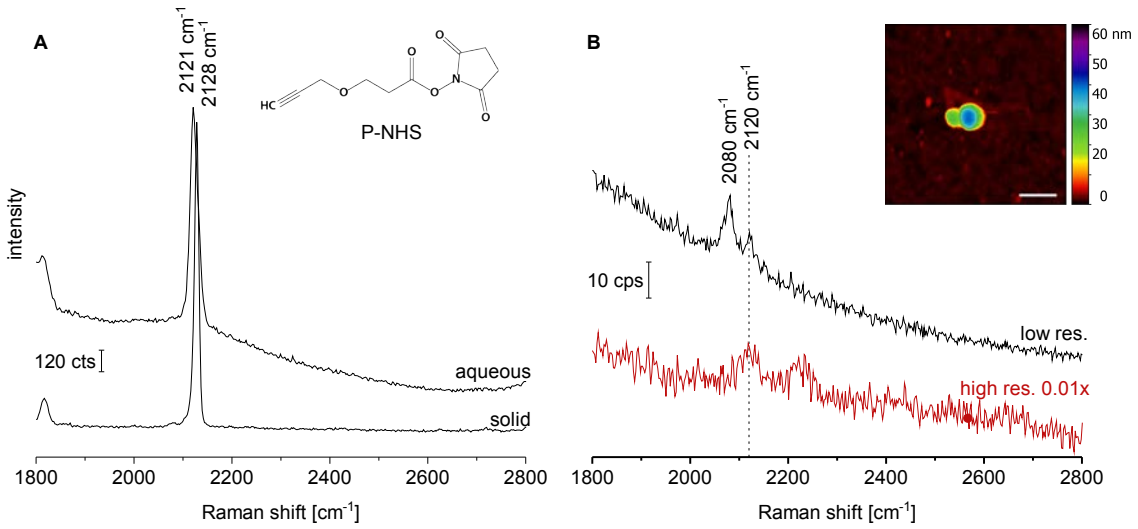

Figure 3.16.: (A) Raman spectra of P-NHS, solid and 125 mM in water. (B) SERS spectra from the same sample position. The high resolution spectrum originates from a single silver nanolens. The dotted line marks the alkyne peak. Low resolution scan: 10x objective, 24 mW, conventional camera. High resolution scan: 100x objective, 0.4 mW, EMCCD camera, scaled down by 0.01. Inset: AFM image of the corresponding silver nanolens. Scale bar: 100 nm. Full spectra and conditions are given in Figures A.13 and A.14 on page 110. Spectra offset for clarity.

non-resonant SERS experiment. Two more data sets from single silver nanolenses are shown in Figure A.15 on page 111 of the Appendix. There, no strong alkyne peaks were observed in the high resolution scans, so that the assignment to the individual nanolenses remains ambiguous.

During the large-scale scans with the 10x objective, repeatedly, peaks that could not be assigned to DNA or streptavidin appeared at apparently random wavenumbers between 2050 cm^{-1} and 2250 cm^{-1}. One example is the peak at 2080 cm^{-1} visible in Figure 3.16 B. The same was true for control experiments on silver nanolenses that did *not* contain streptavidin. Figure 3.17 shows exemplary spectra for such a case. A closer investigation showed these peaks to probably originate from amorphous carbon (nitride) species that are formed as degradation products *in situ*. A more detailed account of the generation of amorphous carbon will be given further below. This raises the question whether the peaks at ca. 2120 cm^{-1} are correctly

attributed to alkyne-modified streptavidin—or belong to those random peaks that are also found in the control, without any alkyne and streptavidin present. In order to clarify this point, three large-scale Raman scans were conducted on silver nanolens samples with and without streptavidin, respectively. The spectra (ca. 1300 for each scan) were analysed for peaks between 2050 cm^{-1} and 2250 cm^{-1} and the respective peak positions were collected. The resulting peak distributions are displayed in the histograms of Figure 3.18. Both histograms show broad distributions, but there is one striking difference: The sample with streptavidin shows a large number of data points for the bin around 2120 cm^{-1}, whereas for the control, only a single peak was observed there. The assignment of the peaks at 2120 cm^{-1} to the alkyne groups on the modified streptavidin therefore stays unaffected. Would these peaks also belong to degradation products from the DNA coating, they would be observed in both types of samples. Photodegradation of streptavidin itself is unlikely: It was shown that direct access of the protein to the silver surface is required for this and that the degradation can be prevented by a monolayer of thiolated molecules (as present here in the form of the DNA coating).[199]

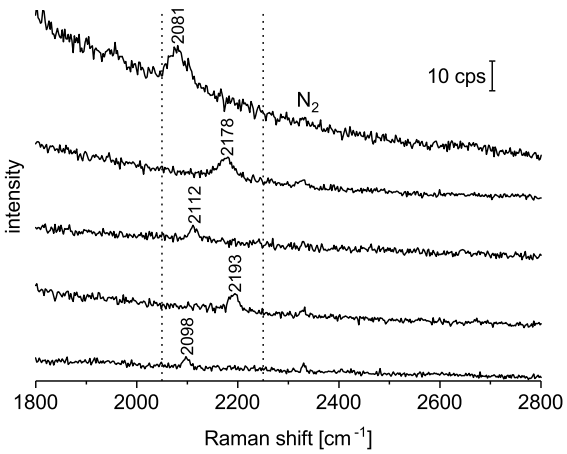

Figure 3.17.: SERS spectra of silver nanolenses without streptavidin, showing spurious peaks between 2050 cm^{-1} and 2250 cm^{-1} (dotted lines). 10x objective, 24 mW power, 8 s integration, offset for clarity.

Amorphous carbon

In an attempt to improve streptavidin detection, SERS spectra under elevated laser intensities were measured, with 2.8 mW at the sample. Spectra from twelve single silver nanolenses with streptavidin were collected under these conditions; the individual spectra are displayed in Figures A.16 and A.17 on page 112f. of the Appendix. Some of the spectra show a broad, double-peaked background signal around 1350 cm^{-1} and 1550 cm^{-1}, for example see spectrum 40-5 in Figure 3.19 A. In others,

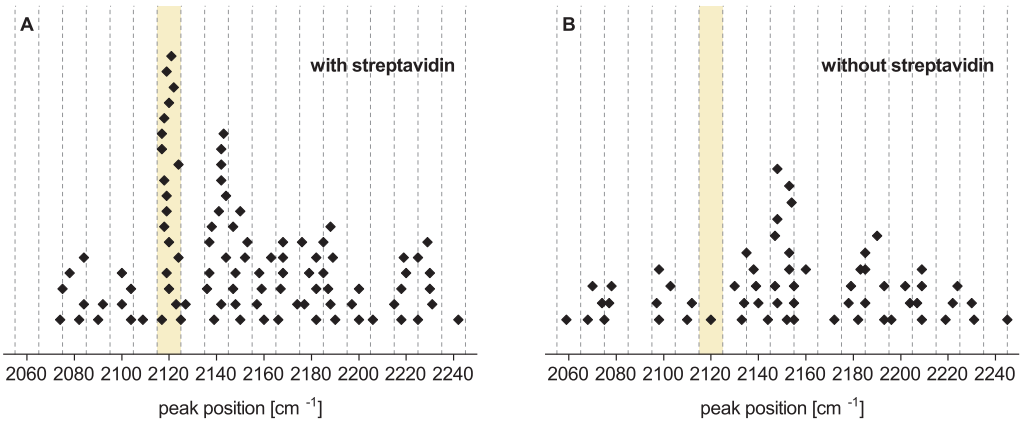

Figure 3.18.: Histograms of the peak occurrence in the spectral region between 2050 cm^{-1} and 2250 cm^{-1}. For each histogram, Raman spectra from three $170 \times 190\,\mu m^2$ scans were analysed. Each point represents one identified peak. Data points are stacked in 10 cm^{-1}-bins, while the x-coordinates still show the exact peak positions. (A) Silver nanolenses with streptavidin. (B) Silver nanolenses without streptavidin.

a variety of intense peaks is observed, which are difficult to assign to characteristic DNA or protein vibrations (see spectra 53-3 and 0-57 in Figure 3.19 A). Such strong signal fluctuations—also referred to as spectral blinking—can be indicative of few-molecule SERS.[200] However, strongly varying, intense peaks in few-molecule SERS are also known to arise from 'amorphous carbon', which can stem from carbon contamination on the particles,[201] or is created *in situ* by photodegradation under the highly enhanced fields.[202–204] Domke *et al.* devote a whole article to the question: "Enhanced Raman Spectroscopy: Single Molecules or Carbon?"[205] In fact, there have been a number of publications that claimed to show single molecule SERS spectra, which were later revealed to originate from amorphous carbon instead.[206–209] Various carbonaceous species make up the amorphous carbon and, accordingly, give many different, rapidly changing peaks.[210] When these peaks are summed up, they yield the overall broad, amorphous carbon spectrum, which resembles the one from graphite.[202,211] It features the so-called 'D peak' around 1350 cm^{-1}, that originates from breathing modes of sp^2-atoms in rings, and the 'G peak' at 1580 cm^{-1}, that originates from bond stretching of pairs of sp^2-atoms in rings and chains.[212] Amorphous carbon has a high Raman cross section and is resonantly excited in SERS experiments.[202,213]

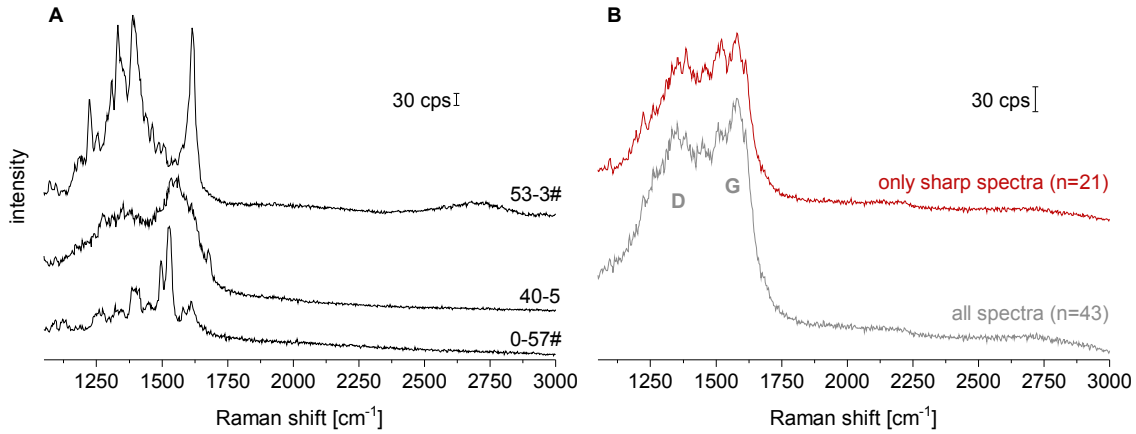

Figure 3.19.: (A) Exemplary SERS spectra from single silver nanolenses. (B) Average SERS spectra from twelve single silver nanolenses. Either all, or only those spectra with sharp peaks were averaged. D and G band are marked, respectively. All individual spectra are shown in Figures A.16 and A.17 on page 112f. of the Appendix. Those averaged for the red graph are marked by a #. Measured with the 100x objective, 4 s integration and 2.8 mW at the sample; spectra offset for clarity.

Fluctuating few-molecule spectra from an analyte of interest can be distinguished from amorphous carbon when a sufficient number of the spectra is averaged. This should give a spectrum that resembles the ensemble spectrum of the respective analyte molecule. If signals originate from amorphous carbon instead, the averaging yields the typical broad carbon band with D and G peak.[205,210] Applied to the data from the twelve single silver nanolenses, a double-peak results that matches in both, position and shape, the various literature for amorphous carbon. It is shown in Figure 3.19 B (grey). When spectra that already have a strong background signal are left out and only those with distinctively sharp peaks are averaged (Figure 3.19, red), the double-peak shape persists, evidencing that the broad amorphous carbon signal is the superposition result of many sharp peaks generated from diverse carbon species.[210]

The intensity ratio of D and G peak can be used to estimate the underlying amorphous carbon's crystallite size L_a. Tuinstra and Koenig have shown that the two quantities are inversely proportional:

$$\frac{I(D)}{I(G)} = \frac{C(\lambda)}{L_a}, \tag{3.3}$$

with $C(516\,\mathrm{nm}) \approx 4.4\,\mathrm{nm}$.[211,214] This relation is widely used, but Ferrari and Robertson pointed out that it holds true only above a threshold size of 2 nm for L_a.[212] For smaller crystallites, the trend reverses, so that with decreasing grain size, $I(D)/I(G)$ decreases as well. This is attributed to the lower probability of finding aromatic rings in the crystallites. The relation proposed for this case reads:

$$\frac{I(D)}{I(G)} = C'(\lambda)\, L_a^2, \tag{3.4}$$

with $C'(514\,\mathrm{nm}) \approx 0.0055\,\mathrm{Å}^{-2}$.[212] Accordingly, the $I(D)/I(G)$-value of 0.81 for the average spectrum of Figure 3.19 B can be assigned to two different L_a values. Equation 3.3 yields 5.4 nm, equation 3.4 yields 1.2 nm. Ferrari and Robertson's data on the change in G band *position* with L_a helps to distinguish the two cases. The G band position of 1580 cm^{-1} as observed in Figure 3.19 indicates that $L_a < 2\,\mathrm{nm}$ and that the system is described by equation 3.4. Depending on the exact pathway of the amorphous carbon formation and due to the dispersive nature of the $I(D)/I(G)$ ratio, this value for L_a could be overestimated.[212] On the other hand, it could be underestimated since $I(D)/I(G)$ rises when amorphous carbons contain a nitrogen content above 5%,[215] which is to be expected for amorphous carbon(nitrides) formed from DNA bases. Overall, the estimated crystallite size of around 1.2 nm is in accordance with what would be expected upon degradation of a DNA coating in a similar size-range ($\sim$ 1.7 nm coating thickness as based on Ref. 161).

The broad feature around 2200 cm^{-1} in Figure 3.19 can be attributed to the sum of various C≡N stretching vibrations in the amorphous carbon (which, as pointed out above, is likely to be more accurately described as an amorphous carbon nitride).[215] These C≡N vibrations give an explanation for the random peaks that were collected in the histograms of Figure 3.18 on page 76. Another potential source for spurious peaks between 2090 cm^{-1} and 2140 cm^{-1} is CO that is chemi- or physisorbed on the metal surface and which commonly accompanies amorphous carbon.[200,216,217] Overall, the generation of amorphous carbon explains several of the features observed in the single silver nanolens SERS spectra:

(i) the broad double-peak background present in some cases

(ii) strongly varying, intense peaks between 1100 cm^{-1} and 1600 cm^{-1}

(iii) random peaks between 1950 cm^{-1} and 2250 cm^{-1}

(iv) occasional broad peaks between 2500 cm^{-1} and 3000 cm^{-1} (combination bands)[218]

The generation of amorphous carbon signals was further investigated by varying the irradiation time. Large area Raman-scans with the 10x objective were conducted, with the aim to get a representative overview despite the notoriously inhomogeneous distribution of nanostructures and hot spot intensities over the surface. The scans used the same laser power (24 mW), but different integration times per spot (0.02 s–2 s). The average of all spectra from a certain scan was generated, thus receiving the average SERS signal from an area as large as $170 \times 190\,\mu m^2$, with approximately 3500 plasmonic nanostructures, as estimated by AFM measurements. Each scan was conducted on a separate position of the silicon wafer. Accounting for the different integration times, the spectra were normalised regarding the N_2-peak at 2330 cm^{-1}. Figure 3.20 displays the respective scan data for silver nanolenses with and without streptavidin. They show a similar trend: The amorphous carbon background increases with longer integration times; at 0.02 s there is no background contribution yet. One of the peaks visible at 0.02 s in the sample without streptavidin, indicated

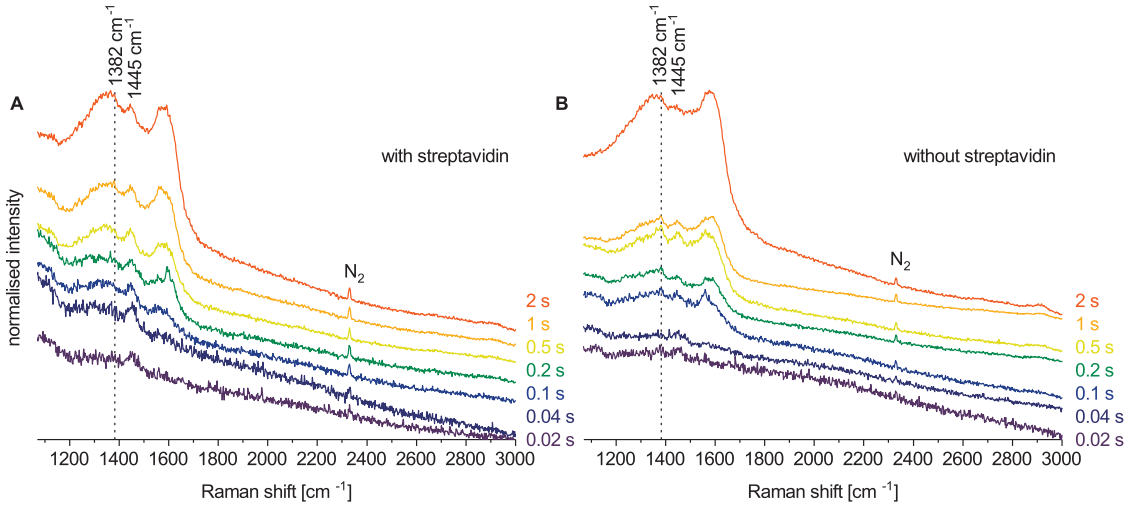

Figure 3.20.: Total area average spectra of $170 \times 190\,\mu m^2$ Raman scans, measured with the 10x-objective and 24 mW at the sample. Integration time per spot is given on the right. Spectra normalised regarding the N_2-peak at 2330 cm^{-1} and offset for clarity. The dotted line marks the position of a characteristic thymine vibration. (A) Silver nanolenses with streptavidin. (B) Silver nanolenses without streptavidin.

by the dotted line, can be attributed to thymine (methyl deformation vibration), which is indeed the most abundant nucleobase in the particle coating.[219] The fact that the band is not seen for the sample with streptavidin might have its reason in streptavidin acting as an additional spacer between the silver nanoparticles. The peak at 1445 cm^{-1} present in all spectra belongs to the third-order transverse optical phonon of silicon.[176] These results suggest that the amorphous carbon species responsible for the background peaks are formed *in situ*. Simply decreasing the integration time will not be the best solution to avoid carbon interference, as the signals of interest then will be too weak (considering that even the omnipresent DNA coating gave only a weak or no Raman signal under the low integration times in Figure 3.20). Several strategies can be pursued instead: Measurements could be conducted at low temperature[202] or in water.[199] It was repeatedly shown that under exclusion of oxygen, no amorphous carbon is formed.[82,210,220] Instead by an inert gas atmosphere, this could be realised by a protective layer of graphene that was already applied for a similar system in this group.[158] The simplest approach would be to combine a lower laser power with longer integration times, thereby allowing a better heat dissipation.

Comparison of gold and silver nanolenses

SERS spectra of four single silver nanolenses with streptavidin were measured under the same conditions as the gold nanolenses from Section 3.3 (i.e., 4 s integration, 0.4 mW, 100x objective; spectra shown in Figure A.18 on page 114 of the Appendix). Even under this low irradiation power, the silver nanolenses showed the intense, fluctuating SERS signals characteristic for amorphous carbon.The average spectrum of the single silver nanolenses accordingly shows a broad, asymmetric carbon peak. The formation of amorphous carbon has been reported for gold and silver nanostructures alike.[200,205] Though, so far there is no systematic study comparing both metals, and also the exact mechanism of the amorphous carbon formation remains unclear. In this context it is interesting that here the formation was only observed for silver nanolenses; during the measurements with the gold nanolenses, there were no amorphous carbon signals. Silver's higher affinity to oxygen and anions likely plays a role in this.[221,222] For silver nanostructures, initial chemical contaminants are also known as potential source of amorphous carbon signals.[201] Here this does not seem

to be the case, as: (i) thiolated molecules displace the carbonaceous contaminants on silver surfaces,[223] and (ii) the amorphous carbon signals set on only after a long-enough irradiation time (see Figure 3.20). Still it cannot be excluded that carbonaceous contaminations remain on the surface after the coating with DNA (which is less dense than the alkanethiol layer from ref. 223) and are subsequently transformed *in situ* into resonant amorphous carbon species with high Raman cross sections.

The study presented here does not include a direct comparison of gold and silver nanolenses' Raman enhancement. The FDTD simulations predict a similar electromagnetic enhancement for them under the 532 nm excitation that was used in the experiments (cf. Figure 3.13 B on page 71). Whereas 532 nm excitation and respectively red-shifted Raman emission are predicted to be near ideal for the gold nanolenses, they are far from the resonance frequency of the silver nanolenses' LSPs: At 450 nm excitation a two orders of magnitude stronger electromagnetic enhancement of the Raman signal is to be expected from the silver structures. An experimental enhancement factor for the silver nanolenses determined at 532 nm excitation therefore would not say much about their potential as plasmonic devices. An adequate comparison of the enhancement potential of gold and silver nanolenses would need to be carried out at their respective plasmonic resonance frequencies. When working with silver nanostructures, the issue of the amorphous carbon formation remains to be addressed in the ways indicated above.

4. Conclusion and outlook

Protocols were developed to coat gold and silver nanoparticles with high densities of single-stranded DNA, rendering them stable even in high-ionic strength buffers. This enabled DNA origami scaffolds to assemble the coated 10 nm, 20 nm and 60 nm gold and silver nanoparticles into discrete, complex nanolenses. *Gold* nanolenses were prepared in three different geometrical arrangements (20-10-60, 20_b-10-60, 10-20-60). For each, sets of single nanolenses were analysed by AFM, SEM, dark-field scattering and Raman spectroscopy. The Raman enhancement was probed by dye molecules in the coating of the 10 nm particles. The gold nanolenses in 20-10-60 geometry overall showed the strongest SERS, with enhancement factors up to 1.4×10^6. This is below the enhancement factors reached in typical single-molecule experiments ($\sim 10^8$),[224] but here it is achieved without significant contribution from chemical enhancement because the DNA separates the dye molecules from the gold surface. The FDTD simulations predict the plasmonic resonance for 20-10-60 gold nanolenses at a wavelength of 577 nm. In order to achieve the maximal signal enhancement in a SERS experiment, the excitation source should be blue-shifted from the plasmonic resonance, and the emission band of interest red-shifted, respectively. With excitation at 532 nm and emission at 583 nm (most prominent TAMRA band), the SERS measurements on the gold nanolenses met these conditions. The experiments also gave insight into the distribution of SERS signal intensities from individual nanolenses. Despite the structural control provided by the DNA origami scaffold, these varied considerably. For some nanolenses, the SEM images showed the low signals to correlate with large interparticle gaps, indicating that the nanoparticle anchoring might be too flexible. In the current DNA origami scaffold designs, the capture strands indeed were longer than their complementary counterparts on the nanoparticles (28 nt vs. 13 nt). The overhangs were intended to decrease steric interactions between the particles and to increase the range of the capture strands. At the same time, the flexibility should allow the particles to touch during the sample

deposition, electrostatically mediated by the highly concentrated magnesium ions. Shorter capture strands, especially for the 10 nm particles, will be a way to reduce these variations. The scattering maxima obtained in the dark-field measurements on the 20-10-60 nanolenses were distributed around 567 nm, matching respective FDTD simulations. The localization of the field enhancement in the 20-10-60 gold nanolenses was further examined by selectively labelling the 20 nm or 60 nm gold nanoparticles with dye molecules. The highest enhancement was found for the gap between the 20 nm and 10 nm gold nanoparticles, in accordance with theoretical predictions and indicating a cascaded field enhancement.

Silver nanolenses were only assembled in the 20-10-60 geometry, as this had yielded the strongest SERS signals for gold nanolenses. When integrated into the DNA origami scaffold, single analyte molecules can be placed at defined positions relative to the plasmonic particles. This is a notable advantage over many other studies, where statistical methods have to prove the single-molecule origin of eventually observed SERS signals.[224] Often there is also no control over the position of the analyte. Here, a single protein (streptavidin) was bound between the 20 nm and 10 nm particle on the DNA origami scaffold, to serve as a biological model analyte. In the respective Raman measurements on single silver nanolenses, strong background peaks were observed that hindered the direct observation of characteristic protein bands. To enable an unambiguous detection nevertheless, streptavidin was labelled with alkyne groups (nineteen on average). A combination of large-scale and small-scale Raman scans, correlated with AFM measurements, localised a single silver nanolens with a detectable alkyne signal. Nanolenses are generally not well-suited for SERS measurements on large molecules like proteins: The highest fields are confined to the relatively small volume between the two smallest particles in the nanolens cascade. The maximal field intensity is highly sensitive to an increase of this gap and it is accordingly difficult to fit a protein in. Still it was possible to detect a signal from the (non-resonant) alkyne labels of a single streptavidin. It is not unlikely that either the protein was deformed in this case, or that only a few of the side chain residues protruded into the plasmonic gap. For protein experiments with stronger signals, a homodimer of two large plasmonic particles would be a better substrate as it provides a comparably larger volume of high field enhancement. For the silver nanolenses, the 532 nm excitation used in the SERS experiments was far from the plasmonic resonance. The FDTD simulations suggest that a hundred-

times-stronger Raman enhancement would be feasible with an excitation around 450 nm. The best experimental way to determine the ideal excitation conditions would be wavelength-scanned SERS measurements with a tunable laser.[225] In the current Raman set-up, no laser line in the blue was available. Measurements in a higher-refractive index medium (such as water) or with larger silver particles would approach the problem from the other side and red-shift the plasmonic resonance. Also, the 21 nm blue-shift of the 60 nm silver nanoparticles upon coating with DNA is worth a closer investigation in this context. The spurious peaks observed in the SERS measurements on single silver nanolenses could be attributed to amorphous carbon. Variation of the integration time showed that the amorphous carbon is formed *in situ*: The respective signals only set on after a certain exposure time to the laser field. The sensitivity of the measurements is limited under such short integration times, so several alternative strategies were proposed to reduce or prevent amorphous carbon formation. So far, no amorphous carbon signals were observed with gold nanolenses. However, considering the literature, it cannot be excluded for future experiments, especially under higher laser powers.[200]

In the present designs, the nanolenses do not yet match the sensitivity of published DNA origami-based dimers,[156] but several strategies for improvement follow from the experiments described above. 20-10-60 nanolenses come with the inherent disadvantage that the particle centres are not aligned in the z-direction, especially when the structures are assembled on a flat DNA origami scaffold and deposited on a solid surface. Therefore, only reduced coupling strengths and field intensities are accessible with such a design. Placing one particle on the other face of a 2D origami scaffold, as in the 20_b-10-60 nanolenses, did not yield better results. The scaffold was apparently not sturdy enough to lift the particles in line; even decreased SERS signals were observed, owing to the DNA origami scaffold as an additional spacer in-between the particles. In a nanolens design that orders the particles according to their size, on the other hand, the particle centres are intrinsically aligned in all directions. It therefore has the greatest potential to yield high field enhancements. However, in the presented experiments, the 10-20-60 gold nanolenses showed the *lowest* SERS signals. The reason for this likely were the relatively long capture strands, which did not keep the 10 nm gold nanoparticles close enough to the 20 nm ones. As indicated above, they should be replaced by shorter capture strands (e.g., 13 nt long, with 4 nt spacer and 9 nt recognition sequence, as for the coating strands).

Applying the coating protocol at 40 °C also to gold, larger gold nanoparticles might be coated with strands of custom sequence and the nanolens cascade could be extended by one particle, so that 10-20-40-80 gold nanolenses could be realised with only small changes in the methods presented here. A fourth particle in the cascade is expected to increase the overall enhancement significantly.[29] There is just enough space on the triangular DNA origami scaffold for such an assembly, though a more rigid support like an 14-helix bundle[150] or a multi-layered rectangle[100] could prove beneficial for higher reproducibility.

Simulations by the Stockman group show that for small three-particle nanolenses (smallest particle $< 6\,\mathrm{nm}$), an *electrodynamic resonance* with giant field enhancements is expected, reaching up to $|E/E_0|^4 \approx 750^4 \approx 3 \times 10^{11}$.[41] Such small particles would also require smaller interparticle gaps for an efficient plasmon interaction. In order to realise these, it will be imperative to develop a nanoparticle coating that is thinner than the current DNA coating. The same is true for other plasmonic assemblies on DNA origami scaffolds that require small gaps and it will be especially beneficial for SERS applications, where signals from the DNA coating potentially overlap with those from a respective analyte. Only a few of the many DNA strands in the particle coating are required for tethering to the DNA origami scaffold. Actually, even a single strand could theoretically suffice for that.[226]

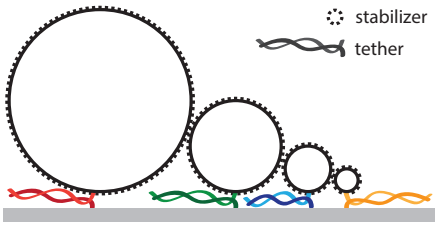

Figure 4.1.: Concept of a nanolens based on particles with a hybrid coating. DNA origami scaffold shown in grey.

The reason why high densities of DNA strands on the particle surface are needed is the stabilisation against salt-induced aggregation. It seems appropriate to distribute the two tasks the coating has to fulfil—tethering and stabilising—between two specialised molecules. For the former, a single DNA strand would ensure that no DNA would interfere in the respective gaps between the plasmonic particles. With DNA strands hybridised in the 'zipper configuration',[227] the positioning should be as precise as with several tethers, and long recognition sequences ($\geq 30\,\mathrm{nt}$) should enable a tight binding. A schematic of such an assembly is shown in Figure 4.1. Similar systems of plasmonic homodimers without DNA origami were realised by Bidault *et al.*[226,228] For stabilisation they used thiolated oligoethylene glycol. Their results indicate that this would not suf-

fice to stabilise 60 nm particles against the magnesium buffer required for the DNA origami integrity. A charged head group on the molecule would help to increase its stabilisation efficiency. At the same time, such a simple molecule would contribute considerably less background signals in SERS measurements. Appropriately-spaced capture strands in zipper configuration could force the particles to touch and would let the stabiliser molecule determine the spacing between the metal surfaces. The chain length of the oligoethylene glycol then would be a way to fine-tune the particle distances. Such an approach would be especially useful as the capture strand placement alone only allows a precision of ~ 5 nm for the particle placement, while at the same time, the electromagnetic Raman enhancement changes greatly even upon small variations in gap size. Still, such singly-charged, small coating molecules might not provide as stable particles as the polyanionic DNA single strands. So it might be worthwhile to explore DNA origami scaffolds that do not require high ionic strength buffers. Wireframe-based origami scaffolds are stable at low salt concentrations (4 mM $MgCl_2$ instead of 10 mM),[103,229] and cationic polymers can stabilise DNA origami scaffolds in absence of magnesium by enveloping them.[113] A hybrid coating as outlined here would be a substantial improvement for the whole field of DNA origami-based plasmonics. With gap sizes in the range of 1 nm, such substrates will be able to compete in terms of field enhancements with more-established SERS substrates.

For applications in the long run, the system integration of self-assembled plasmonic nanostructures into larger, probably silicon-based photonic devices will be fundamental. DNA origami scaffolds can serve as a mediators here. They adsorb in an oriented fashion on lithographically introduced patches on silicon wafers;[230] fluorescent DNA origami beacons were thereby already integrated in respective photonic crystal cavities.[231] The combination of optical cavities with plasmonic nanostructures is a promising avenue for analytical devices with an unprecedented sensitivity.[232] For wet applications, e.g., when integrated into a microfluidic system, the electrostatic adsorption would ideally be followed by a covalent linkage to the surface. A disadvantage of the DNA origami scaffolds applied in this thesis is that there are three possible orientations for equilateral triangles to adsorb onto triangular patches (given that one face adsorbs preferentially). An absolute orientation could be achieved by a disk-shaped DNA origami scaffold with an offset hole.[233] Such lithographically patterned silicon wafers could be used to create

periodic, oriented arrays of the plasmonic nanolenses. These could give rise to long-range photonic interactions with significantly increased field intensities.[234–236] The DNA origami scaffold can also incorporate further functional units, such as quantum dots.[237] When surrounding a nanolens, they can act as gain medium for a spaser.[32] For practical applications it will be a considerable advantage that large quantities of the plasmonic nanostructures can be self-assembled in parallel.

Through offering control over many parameters in the nanosystem, DNA origami is certainly one of the most versatile techniques for fundamental studies on complex plasmonic particle aggregates. The presented work demonstrates the potential and the limitations of such an approach. The assembled gold and silver nanolenses did not yet provide the high field enhancements that would justify their use over simple homodimers, but it was shown that DNA origami is a promising path towards nanolenses that meet the anticipations.

Bibliography

[1] R. P. Feynman, *Engineering and Science* **1960**, *23*, 22–36.

[2] A. Sebastian, Ars Technica: IBM unveils world's first 5nm chip. https://arstechnica.com/gadgets/2017/06/ibm-5nm-chip/ viewed on 2017-07-16.

[3] The British Museum Database - Lycurgus Cup http://www.britishmuseum.org/research/collection_online/collection_object_details.aspx?assetId=36154001&objectId=61219&partId=1, viewed on 2017-07-16, image published under a CC BY-NC-SA 4.0 license.

[4] D. Norris, M. Bawendi, *Physical Review B* **1996**, *53*, 16338.

[5] K. Bourzac, *Nature* **2013**, *493*, 283–284.

[6] M.-C. Daniel, D. Astruc, *Chemical Reviews* **2004**, *104*, 293–346.

[7] S. A. Maier, M. L. Brongersma, P. G. Kik, S. Meltzer, A. A. Requicha, H. A. Atwater, *Advanced Materials* **2001**, *13*, 1501–1505.

[8] J. B. Pendry, *Physical Review Letters* **2000**, *85*, 3966.

[9] T. W. Ebbesen, H. J. Lezec, H. Ghaemi, T. Thio, P. Wolff, *Nature* **1998**, *391*, 667–669.

[10] A. Naldoni, V. M. Shalaev, M. L. Brongersma, *Science* **2017**, *356*, 908–909.

[11] K. L. Kelly, E. Coronado, L. L. Zhao, G. C. Schatz, *The Journal of Physical Chemistry B* **2003**, *107*, 668–677.

[12] R. F. Aroca, D. J. Ross, C. Domingo, *Applied Spectroscopy* **2004**, *58*, 324A–338A.

[13] E. Fort, S. Grésillon, *Journal of Physics D: Applied Physics* **2007**, *41*, 013001.

[14] M. Moskovits, *Reviews of Modern Physics* **1985**, *57*, 783.

[15] M. Fleischmann, P. J. Hendra, A. McQuillan, *Chemical Physics Letters* **1974**, *26*, 163–166.

[16] D. L. Jeanmaire, R. P. Van Duyne, *Journal of Electroanalytical Chemistry and Interfacial Electrochemistry* **1977**, *84*, 1–20.

[17] S.-Y. Ding, E.-M. You, Z.-Q. Tian, M. Moskovits, *Chemical Society Reviews* **2017**, 4042–4076.

[18] K. Kneipp, Y. Wang, H. Kneipp, L. T. Perelman, I. Itzkan, R. R. Dasari, M. S. Feld, *Physical Review Letters* **1997**, *78*, 1667.

[19] S. Nie, S. R. Emory, *Science* **1997**, *275*, 1102–1106.

[20] E. Ozbay, *Science* **2006**, *311*, 189–193.

[21] J. Turkevich, P. C. Stevenson, J. Hillier, *Discussions of the Faraday Society* **1951**, *11*, 55–75.

[22] J. A. Schuller, E. S. Barnard, W. Cai, Y. C. Jun, J. S. White, M. L. Brongersma, *Nature Materials* **2010**, *9*, 193–204.

[23] B. Nikoobakht, M. A. El-Sayed, *Chemistry of Materials* **2003**, *15*, 1957–1962.

[24] P. S. Kumar, I. Pastoriza-Santos, B. Rodriguez-Gonzalez, F. J. G. de Abajo, L. M. Liz-Marzan, *Nanotechnology* **2007**, *19*, 015606.

[25] J. Xie, Q. Zhang, J. Y. Lee, D. I. Wang, *ACS Nano* **2008**, *2*, 2473–2480.

[26] R. Jin, Y. Cao, C. A. Mirkin, K. Kelly, G. C. Schatz, J. Zheng, *Science* **2001**, *294*, 1901–1903.

[27] J. Prinz, B. Schreiber, L. Olejko, J. Oertel, J. Rackwitz, A. Keller, I. Bald, *The Journal of Physical Chemistry Letters* **2013**, *4*, 4140–4145.

[28] V. Merk, J. Kneipp, K. Leosson, *Advanced Optical Materials* **2013**, *1*, 313–318.

[29] K. Li, M. I. Stockman, D. J. Bergman, *Physical Review Letters* **2003**, *91*, 227402.

[30] K. Li, M. I. Stockman, D. J. Bergman, *Physical Review B* **2005**, *72*, 153401.

[31] S. Biswas, X. Liu, J. W. Jarrett, D. Brown, V. Pustovit, A. Urbas, K. L. Knappenberger Jr, P. F. Nealey, R. A. Vaia, *Nano Letters* **2015**, *15*, 1836–1842.

[32] K. Li, X. Li, M. I. Stockman, D. J. Bergman, *Physical Review B* **2005**, *71*, 115409.

[33] S. Toroghi, P. G. Kik, *Applied Physics Letters* **2012**, *100*, 183105.

[34] S. Toroghi, P. Kika in Proceedings of SPIE, *Vol. 8457*, **2012**, pp. 84570D–1.

[35] G. Zito, G. Rusciano, A. Sasso, *The Journal of Chemical Physics* **2016**, *145*, 054708.

[36] M. E. Mezeme, S. Lasquellec, C. Brosseau, *Physical Review E* **2011**, *84*, 026612.

[37] Z. Zhang, Z. Zhang, H. Wang, *Applied Optics* **2011**, *50*, 3513–3518.

[38] L. Yang, X. Luo, M. Hong, *Journal of Computational and Theoretical Nanoscience* **2010**, *7*, 1364–1367.

[39] Z. Li, Z. Yang, H. Xu, *Physical Review Letters* **2006**, *97*, 079701.

[40] K. Li, M. I. Stockman, D. J. Bergman, *Physical Review Letters* **2006**, *97*, 079702.

[41] J. Dai, F. Cajko, I. Tsukerman, M. I. Stockman, *Physical Review B* **2008**, *77*, 115419.

[42] J. Kneipp, X. Li, M. Sherwood, U. Panne, H. Kneipp, M. I. Stockman, K. Kneipp, *Analytical Chemistry* **2008**, *80*, 4247–4251.

[43] V. Kravets, G. Zoriniants, C. P. Burrows, F. Schedin, C. Casiraghi, P. Klar, A. Geim, W. L. Barnes, A. Grigorenko, *Physical Review Letters* **2010**, *105*, 246806.

[44] S. Syrenova, C. Wadell, C. Langhammer, *Nano Letters* **2014**, *14*, 2655–2663.

[45] M. L. Coluccio, F. Gentile, G. Das, A. Nicastri, A. M. Perri, P. Candeloro, G. Perozziello, R. P. Zaccaria, J. S. T. Gongora, S. Alrasheed, et al., *Science Advances* **2015**, *1*, e1500487.

[46] M. Coluccio, F. Gentile, G. Das, G. Perozziello, N. Malara, S. Alrasheed, P. Candeloro, E. Di Fabrizio, *Journal of Optics* **2015**, *17*, 114021.

[47] X. Liu, S. Biswas, J. W. Jarrett, E. Poutrina, A. Urbas, K. L. Knappenberger, R. A. Vaia, P. F. Nealey, *Advanced Materials* **2015**, *27*, 7314–7319.

[48] G. Das, S. Alrasheed, M. L. Coluccio, F. Gentile, A. Nicastri, P. Candeloro, G. Cuda, G. Perozziello, E. Di Fabrizio, *RSC Advances* **2016**, *6*, 107916–107923.

[49] C. Hoeppener, Z. J. Lapin, P. Bharadwaj, L. Novotny, *Physical Review Letters* **2012**, *109*, 017402.

[50] J. A. Lloyd, S. H. Ng, A. C. Liu, Y. Zhu, W. Chao, T. Coenen, J. Etheridge, D. E. Gomez, U. Bach, *ACS Nano* **2017**, *11*, 1604–1612.

[51] N. C. Seeman, *Nature* **2003**, *421*, 427–432.

[52] F. Hong, F. Zhang, Y. Liu, H. Yan, *Chemical Reviews* **2017**, *117*, 12584–12640.

[53] P. W. Rothemund, *Nature* **2006**, *440*, 297–302.

[54] C. E. Castro, F. Kilchherr, D.-N. Kim, E. L. Shiao, T. Wauer, P. Wortmann, M. Bathe, H. Dietz, *Nature Methods* **2011**, *8*, 221–229.

[55] S. Bidault, F. J. Garcia de Abajo, A. Polman, *Journal of the American Chemical Society* **2008**, *130*, 2750–2751.

[56] M. P. Busson, B. Rolly, B. Stout, N. Bonod, E. Larquet, A. Polman, S. Bidault, *Nano Letters* **2011**, *11*, 5060–5065.

[57] B. Ding, S. Cabrini, R. N. Zuckermann, J. Bokor, *Journal of Vacuum Science & Technology B: Microelectronics and Nanometer Structures Processing Measurement and Phenomena* **2009**, *27*, 184–187.

[58] B. Ding, Z. Deng, H. Yan, S. Cabrini, R. N. Zuckermann, J. Bokor, *Journal of the American Chemical Society* **2010**, *132*, 3248–3249.

[59] S. A. Maier, *Plasmonics: Fundamentals and Applications*, Springer Science & Business Media, **2007**.

[60] P. G. Etchegoin, E. Le Ru, M. Meyer, *The Journal of Chemical Physics* **2006**, *125*, 164705.

[61] S. Schlücker, W. Kiefer, *Surface-Enhanced Raman Spectroscopy: Analytical, Biophysical and Life Science Applications*, John Wiley & Sons, **2011**.

[62] P. B. Johnson, R.-W. Christy, *Physical Review B* **1972**, *6*, 4370.

[63] K. A. Willets, R. P. Van Duyne, *Annual Review of Physical Chemistry* **2007**, *58*, 267–297.

[64] T. V. Shahbazyan, M. I. Stockman, *Plasmonics: Theory and Applications*, Springer, **2013**.

[65] K. Yee, *IEEE Transactions on antennas and propagation* **1966**, *14*, 302–307.

[66] E. Prodan, C. Radloff, N. J. Halas, P. Nordlander, *Science* **2003**, *302*, 419–422.

[67] P. Nordlander, C. Oubre, E. Prodan, K. Li, M. Stockman, *Nano Letters* **2004**, *4*, 899–903.

[68] K. Yoshida, T. Itoh, H. Tamaru, V. Biju, M. Ishikawa, Y. Ozaki, *Physical Review B* **2010**, *81*, 115406.

[69] M. I. Stockman, L. N. Pandey, L. S. Muratov, T. F. George, *Physical Review Letters* **1994**, *72*, 2486.

[70] Z. Wang, S. Pan, T. D. Krauss, H. Du, L. J. Rothberg, *Proceedings of the National Academy of Sciences* **2003**, *100*, 8638–8643.

[71] G. Pellegrini, M. Celebrano, M. Finazzi, P. Biagioni, *The Journal of Physical Chemistry C* **2016**, *120*, 26021–26024.

[72] E. Le Ru, P. Etchegoin, *Principles of Surface-Enhanced Raman Spectroscopy and Related Plasmonic Effects*, Elsevier, **2008**.

[73] D. J. Bergman, M. I. Stockman, *Physical Review Letters* **2003**, *90*, 027402.

[74] F. Siebert, P. Hildebrandt, *Vibrational Spectroscopy in Life Science*, John Wiley & Sons, **2008**.

[75] J. W. Strutt, *The London Edinburgh and Dublin Philosophical Magazine and Journal of Science* **1871**, *41*, 447–454.

[76] A. Smekal, *Naturwissenschaften* **1923**, *11*, 873–875.

[77] C. V. Raman, *Indian Journal of Physics* **1928**, *2*, 387–398.

[78] G. Landsberg, L. Mandelstam, *Naturwissenschaften* **1928**, *16*, 558.

[79] G. Placzek, *Rayleigh-Streuung und Raman-Effekt*, *Vol. 2*, Akademische Verlag-Gesellschaft, **1934**.

[80] K. Kneipp, H. Kneipp, H. G. Bohr, *Single-Molecule SERS Spectroscopy*, Springer, **2006**, pp. 261–277.

[81] K. Kneipp, Y. Wang, H. Kneipp, I. Itzkan, R. R. Dasari, M. S. Feld, *Physical Review Letters* **1996**, *76*, 2444.

[82] Y. Fang, N.-H. Seong, D. D. Dlott, *Science* **2008**, *321*, 388–392.

[83] E. Zeman, K. Carron, G. C. Schatz, R. Van Duyne, *The Journal of Chemical Physics* **1987**, *87*, 4189–4200.

[84] J. D. Watson, F. H. Crick, *Nature* **1953**, *171*, 737–738.

[85] J. C. Wang, *Proceedings of the National Academy of Sciences* **1979**, *76*, 200–203.

[86] R. Langridge, H. Wilson, C. Hooper, M. H. Wilkins, L. Hamilton, *Journal of Molecular Biology* **1960**, *2*, 19–IN11.

[87] F. H. C. Crick, L. Barnett, S. Brenner, R. J. Watts-Tobin, *Nature* **1961**, *192*, 1227–1232.

[88] H. R. Drew, R. M. Wing, T. Takano, C. Broka, S. Tanaka, K. Itakura, R. E. Dickerson, *Proceedings of the National Academy of Sciences* **1981**, *78*, 2179–2183.

[89] D. N. Gopaul, F. Guo, G. D. Van Duyne, *The EMBO Journal* **1998**, *17*, 4175–4187.

[90] R. Holliday, *Genetical Research* **1964**, *5*, 282–304.

[91] Y. Liu, S. C. West, *Nature Reviews Molecular Cell Biology* **2004**, *5*, 937–944.

[92] N. C. Seeman, N. R. Kallenbach, *Biophysical Journal* **1983**, *44*, 201–209.

[93] Y. Wang, J. E. Mueller, B. Kemper, N. C. Seeman, *Biochemistry* **1991**, *30*, 5667–5674.

[94] S. N. Cohen, A. C. Chang, H. W. Boyer, R. B. Helling, *Proceedings of the National Academy of Sciences* **1973**, *70*, 3240–3244.

[95] N. C. Seeman, *Journal of Theoretical Biology* **1982**, *99*, 237–247.

[96] J. Chen, N. C. Seeman, *Nature* **1991**, *350*, 631–633.

[97] N. C. Seeman, *Annual Review of Biochemistry* **2010**, *79*, 65–87.

[98] V. Linko, H. Dietz, *Current Opinion in Biotechnology* **2013**, *24*, 555–561.

[99] E. S. Andersen, M. Dong, M. M. Nielsen, K. Jahn, R. Subramani, W. Mamdouh, M. M. Golas, B. Sander, H. Stark, C. L. Oliveira, et al., *Nature* **2009**, *459*, 73–76.

[100] S. M. Douglas, H. Dietz, T. Liedl, B. Högberg, F. Graf, W. M. Shih, *Nature* **2009**, *459*, 414–418.

[101] D. Han, S. Pal, J. Nangreave, Z. Deng, Y. Liu, H. Yan, *Science* **2011**, *332*, 342–346.

[102] Y. Ke, L. L. Ong, W. M. Shih, P. Yin, *Science* **2012**, *338*, 1177–1183.

[103] E. Benson, A. Mohammed, J. Gardell, S. Masich, E. Czeizler, P. Orponen, B. Högberg, *Nature* **2015**, *523*, 441–444.

[104] X. Li, X. Yang, J. Qi, N. C. Seeman, *Journal of the American Chemical Society* **1996**, *118*, 6131–6140.

[105] S. M. Douglas, A. H. Marblestone, S. Teerapittayanon, A. Vazquez, G. M. Church, W. M. Shih, *Nucleic Acids Research* **2009**, *37*, 5001–5006.

[106] R. Veneziano, S. Ratanalert, K. Zhang, F. Zhang, H. Yan, W. Chiu, M. Bathe, *Science* **2016**, 4388.

[107] W. Liu, H. Zhong, R. Wang, N. C. Seeman, *Angewandte Chemie International Edition* **2011**, *123*, 278–281.

[108] J. Sharma, R. Chhabra, C. S. Andersen, K. V. Gothelf, H. Yan, Y. Liu, *Journal of the American Chemical Society* **2008**, *130*, 7820–7821.

[109] R. Chhabra, J. Sharma, Y. Ke, Y. Liu, S. Rinker, S. Lindsay, H. Yan, *Journal of the American Chemical Society* **2007**, *129*, 10304–10305.

[110] N. Wu, D. M. Czajkowsky, J. Zhang, J. Qu, M. Ye, D. Zeng, X. Zhou, J. Hu, Z. Shao, B. Li, et al., *Journal of the American Chemical Society* **2013**, *135*, 12172–12175.

[111] T. G. Martin, H. Dietz, *Nature Communications* **2012**, *3*, 1103.

[112] V. Cassinelli, B. Oberleitner, J. Sobotta, P. Nickels, G. Grossi, S. Kempter, T. Frischmuth, T. Liedl, A. Manetto, *Angewandte Chemie International Edition* **2015**, *54*, 7795–7798.

[113] N. P. Agarwal, M. Matthies, F. N. Gür, K. Osada, T. L. Schmidt, *Angewandte Chemie International Edition* **2017**, *129*, 5552–5556.

[114] A. N. Marchi, I. Saaem, B. N. Vogen, S. Brown, T. H. LaBean, *Nano Letters* **2014**, *14*, 5740–5747.

[115] T. Gerling, K. F. Wagenbauer, A. M. Neuner, H. Dietz, *Science* **2015**, *347*, 1446–1452.

[116] M. Langecker, V. Arnaut, T. G. Martin, J. List, S. Renner, M. Mayer, H. Dietz, F. C. Simmel, *Science* **2012**, *338*, 932–936.

[117] S. M. Douglas, I. Bachelet, G. M. Church, *Science* **2012**, *335*, 831–834.

[118] B. Teschome, S. Facsko, T. Schoenherr, J. Kerbusch, A. Keller, A. Erbe, *Langmuir* **2016**, *32*, 10159–10165.

[119] J. Fu, Y. R. Yang, A. Johnson-Buck, M. Liu, Y. Liu, N. G. Walter, N. W. Woodbury, H. Yan, *Nature Nanotechnology* **2014**, *9*, 531–536.

[120] N. D. Derr, B. S. Goodman, R. Jungmann, A. E. Leschziner, W. M. Shih, S. L. Reck-Peterson, *Science* **2012**, *338*, 662–665.

[121] P. C. Nickels, B. Wunsch, P. Holzmeister, W. Bae, L. M. Kneer, D. Grohmann, P. Tinnefeld, T. Liedl, *Science* **2016**, *354*, 305–307.

[122] J. J. Funke, P. Ketterer, C. Lieleg, S. Schunter, P. Korber, H. Dietz, *Science Advances* **2016**, *2*, e1600974.

[123] L. Olejko, P. J. Cywinski, I. Bald, *Angewandte Chemie International Edition* **2015**, *54*, 673–677.

[124] L. Olejko, P. Cywinski, I. Bald, *Nanoscale* **2016**, *8*, 10339–10347.

[125] L. Olejko, I. Bald, *RSC Advances* **2017**, *7*, 23924–23934.

[126] J. Rackwitz, J. Kopyra, I. Dkabkowska, K. Ebel, M. L. Rankovic, A. R. Milosavljevic, I. Bald, *Angewandte Chemie International Edition* **2016**, *128*, 10404–10408.

[127] S. Vogel, J. Rackwitz, R. Schurman, J. Prinz, A. R. Milosavljevic, M. Refregiers, A. Giuliani, I. Bald, *The Journal of Physical Chemistry Letters* **2015**, *6*, 4589–4593.

[128] A. P. Alivisatos, K. P. Johnsson, X. Peng, T. E. Wilson, et al., *Nature* **1996**, *382*, 609–611.

[129] C. A. Mirkin, R. L. Letsinger, R. C. Mucic, J. J. Storhoff, *Nature* **1996**, *382*, 607–609.

[130] H. Sellers, A. Ulman, Y. Shnidman, J. E. Eilers, *Journal of the American Chemical Society* **1993**, *115*, 9389–9401.

[131] J.-S. Lee, A. K. Lytton-Jean, S. J. Hurst, C. A. Mirkin, *Nano Letters* **2007**, *7*, 2112–2115.

[132] M. R. Jones, N. C. Seeman, C. A. Mirkin, *Science* **2015**, *347*, 1260901.

[133] J. J. Storhoff, R. Elghanian, R. C. Mucic, C. A. Mirkin, R. L. Letsinger, *Journal of the American Chemical Society* **1998**, *120*, 1959–1964.

[134] S. J. Hurst, A. K. Lytton-Jean, C. A. Mirkin, *Analytical Chemistry* **2006**, *78*, 8313–8318.

[135] X. Zhang, M. R. Servos, J. Liu, *Journal of the American Chemical Society* **2012**, *134*, 7266–7269.

[136] Y. Zu, Z. Gao, *Analytical Chemistry* **2009**, *81*, 8523–8528.

[137] J. J. Storhoff, R. Elghanian, C. A. Mirkin, R. L. Letsinger, *Langmuir* **2002**, *18*, 6666–6670.

[138] H. Kimura-Suda, D. Y. Petrovykh, M. J. Tarlov, L. J. Whitman, *Journal of the American Chemical Society* **2003**, *125*, 9014–9015.

[139] B. Liu, J. Liu, *Analytical Methods* **2017**, *9*, 2633–2643.

[140] I. Tokareva, E. Hutter, *Journal of the American Chemical Society* **2004**, *126*, 15784–15789.

[141] S. Pal, Z. Deng, B. Ding, H. Yan, Y. Liu, *Angewandte Chemie International Edition* **2010**, *122*, 2760–2764.

[142] J. Chao, Y. Lin, H. Liu, L. Wang, C. Fan, *Materials Today* **2015**, *18*, 326–335.

[143] R. Schreiber, N. Luong, Z. Fan, A. Kuzyk, P. C. Nickels, T. Zhang, D. M. Smith, B. Yurke, W. Kuang, A. O. Govorov, et al., *Nature Communications* **2013**, *4*, 2948.

[144] X. Lan, Z. Chen, G. Dai, X. Lu, W. Ni, Q. Wang, *Journal of the American Chemical Society* **2013**, *135*, 11441–11444.

[145] A. Kuzyk, Y. Yang, X. Duan, S. Stoll, A. O. Govorov, H. Sugiyama, M. Endo, N. Liu, *Nature Communications* **2016**, *7*, 10591.

[146] A. Kuzyk, M. J. Urban, A. Idili, F. Ricci, N. Liu, *Science Advances* **2017**, *3*, e1602803.

[147] F. N. Guer, F. W. Schwarz, J. Ye, S. Diez, T. L. Schmidt, *ACS Nano* **2016**, *10*, 5374–5382.

[148] W. P. Klein, C. N. Schmidt, B. Rapp, S. Takabayashi, W. B. Knowlton, J. Lee, B. Yurke, W. L. Hughes, E. Graugnard, W. Kuang, *Nano Letters* **2013**, *13*, 3850–3856.

[149] K. Vogele, J. List, G. Pardatscher, N. B. Holland, F. C. Simmel, T. Pirzer, *ACS Nano* **2016**, *10*, 11377–11384.

[150] E.-M. Roller, L. V. Besteiro, C. Pupp, L. K. Khorashad, A. O. Govorov, T. Liedl, *Nature Physics* **2017**, 761–765.

[151] G. P. Acuna, M. Bucher, I. H. Stein, C. Steinhauer, A. Kuzyk, P. Holzmeister, R. Schreiber, A. Moroz, F. D. Stefani, T. Liedl, et al., *ACS Nano* **2012**, *6*, 3189–3195.

[152] G. Acuna, F. Möller, P. Holzmeister, S. Beater, B. Lalkens, P. Tinnefeld, *Science* **2012**, *338*, 506–510.

[153] C. Vietz, I. Kaminska, M. Sanz Paz, P. Tinnefeld, G. P. Acuna, *ACS Nano* **2017**, 4969–4975.

[154] T. Zhang, N. Gao, S. Li, M. J. Lang, Q.-H. Xu, *The Journal of Physical Chemistry Letters* **2015**, *6*, 2043–2049.

[155] J. Prinz, C. Heck, L. Ellerik, V. Merk, I. Bald, *Nanoscale* **2016**, *8*, 5612–5620.

[156] S. Simoncelli, E.-M. Roller, P. Urban, R. Schreiber, A. J. Turberfield, T. Liedl, T. Lohmueller, *ACS Nano* **2016**, *10*, 9809–9815.

[157] S. Tanwar, K. Haldar, T. Sen, *Journal of the American Chemical Society: in press* **2017**.

[158] J. Prinz, A. Matkovic, J. Pevsic, R. Gajic, I. Bald, *Small* **2016**, *12*, 5458–5467.

[159] P. Kuehler, E.-M. Roller, R. Schreiber, T. Liedl, T. Lohmueller, J. Feldmann, *Nano Letters* **2014**, *14*, 2914–2919.

[160] M. Pilo-Pais, A. Watson, S. Demers, T. LaBean, G. Finkelstein, *Nano Letters* **2014**, *14*, 2099–2104.

[161] V. V. Thacker, L. O. Herrmann, D. O. Sigle, T. Zhang, T. Liedl, J. J. Baumberg, U. F. Keyser, *Nature Communications* **2014**, *5*, 3448.

[162] M. T. Spence, I. D. Johnson, *The molecular probes handbook: a guide to fluorescent probes and labeling technologies*, Life Technologies Corporation, **2010**.

[163] X. Zhang, T. Gouriye, K. Goeken, M. R. Servos, R. Gill, J. Liu, *The Journal of Physical Chemistry C* **2013**, *117*, 15677–15684.

[164] D. Y. Petrovykh, H. Kimura-Suda, L. J. Whitman, M. J. Tarlov, *Journal of the American Chemical Society* **2003**, *125*, 5219–5226.

[165] N. L. Rosi, D. A. Giljohann, C. S. Thaxton, A. K. Lytton-Jean, M. S. Han, C. A. Mirkin, *Science* **2006**, *312*, 1027–1030.

[166] F. Li, H. Zhang, B. Dever, X.-F. Li, X. C. Le, *Bioconjugate Chemistry* **2013**, *24*, 1790–1797.

[167] P. E. Laibinis, G. M. Whitesides, D. L. Allara, Y. T. Tao, A. N. Parikh, R. G. Nuzzo, *Journal of the American Chemical Society* **1991**, *113*, 7152–7167.

[168] E. E. L. Tanner, S. V. Sokolov, N. P. Young, R. G. Compton, *Physical Chemistry Chemical Physics* **2017**, *19*, 9733–9738.

[169] N. M. Green, *Methods in Enzymology* **1990**, *184*, 51–67.

[170] C. M. Dundas, D. Demonte, S. Park, *Applied Microbiology and Biotechnology* **2013**, *97*, 9343–9353.

[171] D. E. Hyre, I. Le Trong, E. A. Merritt, J. F. Eccleston, N. M. Green, R. E. Stenkamp, P. S. Stayton, *Protein Science* **2006**, *15*, 459–467.

[172] H. Yamakoshi, K. Dodo, A. Palonpon, J. Ando, K. Fujita, S. Kawata, M. Sodeoka, *Journal of the American Chemical Society* **2012**, *134*, 20681–20689.

[173] L. R. Cohen, K. Strupat, F. Hillenkamp, *Journal of the American Society for Mass Spectrometry* **1997**, *8*, 1046–1052.

[174] A. Wortmann, T. Pimenova, S. Alves, R. Zenobi, *Analyst* **2007**, *132*, 199–207.

[175] G. Bellot, M. A. McClintock, C. Lin, W. M. Shih, *Nature Methods* **2011**, *8*, 192–194.

[176] A. Zwick, R. Carles, *Physical Review B* **1993**, *48*, 6024.

[177] G. Socrates, *Infrared and Raman Characteristic Group Frequencies: Tables and Charts*, John Wiley & Sons, **2004**.

[178] Z. Zhu, T. Zhu, Z. Liu, *Nanotechnology* **2004**, *15*, 357–364.

[179] D.-S. Wang, M. Kerker, *Physical Review B* **1981**, *24*, 1777.

[180] K. Kneipp, H. Kneipp, I. Itzkan, R. R. Dasari, M. S. Feld, *Journal of Physics: Condensed Matter* **2002**, *14*, R597.

[181] Y. Zhang, B. Walkenfort, J. H. Yoon, S. Schlucker, W. Xie, *Physical Chemistry Chemical Physics* **2015**, *17*, 21120–21126.

[182] W. S. Cleveland, *Journal of the American Statistical Association* **1979**, *74*, 829–836.

[183] Nanodrop 200c user manual, Thermo Scientific.

[184] X. Liu, M. Atwater, J. Wang, Q. Huo, *Colloids and Surfaces B: Biointerfaces* **2007**, *58*, 3–7.

[185] D. Paramelle, A. Sadovoy, S. Gorelik, P. Free, J. Hobley, D. G. Fernig, *Analyst* **2014**, *139*, 4855–4861.

[186] E. D. Palik, *Handbook of Optical Constants of Solids*, *Vol. 3*, Academic Press, **1998**.

[187] J. Kundu, O. Neumann, B. Janesko, D. Zhang, S. Lal, A. Barhoumi, G. Scuseria, N. Halas, *The Journal of Physical Chemistry C* **2009**, *113*, 14390–14397.

[188] X. Zhang, M. R. Servos, J. Liu, *Chemical Communications* **2012**, *48*, 10114–10116.

[189] T. M. Herne, M. J. Tarlov, *Journal of the American Chemical Society* **1997**, *119*, 8916–8920.

[190] A. C. Templeton, J. J. Pietron, R. W. Murray, P. Mulvaney, *The Journal of Physical Chemistry B* **2000**, *104*, 564–570.

[191] G. Mie, *Annalen der Physik* **1908**, *330*, 377–445.

[192] P. S. Popp, J. F. Herrmann, E.-C. Fritz, B. J. Ravoo, C. Höppener, *Small* **2016**, *12*, 1667–1675.

[193] M. Moskovits, *Physical Chemistry Chemical Physics* **2013**, *15*, 5301–5311.

[194] V. Pini, P. Kosaka, J. Ruz, O. Malvar, M. Encinar, J. Tamayo, M. Calleja, *Scientific Reports* **2016**, *6*, 22836.

[195] Lumerical Knowledge Base: Plane waves - Angled injection, https://kb.lumerical.com/en/ref_sim_obj_plane_waves_-_angled_injection.html, viewed on 2017-07-11.

[196] L. V. Brown, H. Sobhani, J. B. Lassiter, P. Nordlander, N. J. Halas, *ACS Nano* **2010**, *4*, 819–832.

[197] M. D. Malinsky, K. L. Kelly, G. C. Schatz, R. P. Van Duyne, *Journal of the American Chemical Society* **2001**, *123*, 1471–1482.

[198] T. Linnert, P. Mulvaney, A. Henglein, *The Journal of Physical Chemistry* **1993**, *97*, 679–682.

[199] E. J. Bjerneld, F. Svedberg, P. Johansson, M. Kall, *The Journal of Physical Chemistry A* **2004**, *108*, 4187–4193.

[200] N. P. Pieczonka, R. F. Aroca, *ChemPhysChem* **2005**, *6*, 2473–2484.

[201] C. E. Taylor, S. D. Garvey, J. E. Pemberton, *Analytical Chemistry* **1996**, *68*, 2401–2408.

[202] J. Tsang, J. Demuth, P. Sanda, J. Kirtley, *Chemical Physics Letters* **1980**, *76*, 54–57.

[203] G. Goncher, C. Parsons, C. Harris, *The Journal of Physical Chemistry* **1984**, *88*, 4200–4209.

[204] J. S. Suh, M. Moskovits, J. Shakhesemampour, *The Journal of Physical Chemistry* **1993**, *97*, 1678–1683.

[205] K. F. Domke, D. Zhang, B. Pettinger, *The Journal of Physical Chemistry C* **2007**, *111*, 8611–8616.

[206] E. J. Bjerneld, P. Johansson, M. Käll, *Single Molecules* **2000**, *1*, 239–248.

[207] A. Otto, *Journal of Raman Spectroscopy* **2002**, *33*, 593–598.

[208] C. C. Neacsu, J. Dreyer, N. Behr, M. B. Raschke, *Physical Review B* **2006**, *73*, 193406.

[209] K. F. Domke, B. Pettinger, *Physical Review B* **2007**, *75*, 236401.

[210] A. Kudelski, B. Pettinger, *Chemical Physics Letters* **2000**, *321*, 356–362.

[211] F. Tuinstra, J. L. Koenig, *The Journal of Chemical Physics* **1970**, *53*, 1126–1130.

[212] A. C. Ferrari, J. Robertson, *Physical Review B* **2000**, *61*, 14095.

[213] A. Ferrari, J. Robertson, *Physical Review B* **2001**, *64*, 075414.

[214] D. S. Knight, W. B. White, *Journal of Materials Research* **1989**, *4*, 385–393.

[215] A. Ferrari, S. Rodil, J. Robertson, *Physical Review B* **2003**, *67*, 155306.

[216] A. Kudelski, B. Pettinger, *Chemical Physics Letters* **2004**, *383*, 76–79.

[217] I. Mrozek, C. Pettenkofer, A. Otto, *Surface Science* **1990**, *238*, 192–198.

[218] P. J. Moyer, J. Schmidt, L. M. Eng, A. J. Meixner, G. W. Sandmann, H. Dietz, W. Plieth, *Journal of the American Chemical Society* **2000**, *122*, 5409–5410.

[219] C. Otto, T. Van den Tweel, F. De Mul, J. Greve, *Journal of Raman Spectroscopy* **1986**, *17*, 289–298.

[220] P. Etchegoin, H. Liem, R. Maher, L. Cohen, R. Brown, H. Hartigan, M. Milton, J. Gallop, *Chemical Physics Letters* **2002**, *366*, 115–121.

[221] A. Kudelski, *The Journal of Physical Chemistry B* **2006**, *110*, 12610–12615.

[222] A. Kudelski, *Journal of Raman Spectroscopy* **2007**, *38*, 1494–1499.

[223] K. L. Norrod, K. L. Rowlen, *Analytical Chemistry* **1998**, *70*, 4218–4221.

[224] P. G. Etchegoin, E. Le Ru, *Physical Chemistry Chemical Physics* **2008**, *10*, 6079–6089.

[225] A. D. McFarland, M. A. Young, J. A. Dieringer, R. P. Van Duyne, *The Journal of Physical Chemistry B* **2005**, *109*, 11279–11285.

[226] S. Bidault, A. Devilez, V. Maillard, L. Lermusiaux, J.-M. Guigner, N. Bonod, J. Wenger, *ACS Nano* **2016**, *10*, 4806–4815.

[227] C. Vietz, B. Lalkens, G. P. Acuna, P. Tinnefeld, *New Journal of Physics* **2016**, *18*, 045012.

[228] S. Bidault, A. Devilez, P. Ghenuche, B. Stout, N. Bonod, J. Wenger, *ACS Photonics* **2016**, *3*, 895–903.

[229] M. Matthies, N. P. Agarwal, T. L. Schmidt, *Nano Letters* **2016**, *16*, 2108–2113.

[230] A. Gopinath, P. W. Rothemund, *ACS Nano* **2014**, *8*, 12030–12040.

[231] A. Gopinath, E. Miyazono, A. Faraon, P. W. Rothemund, *Nature* **2016**, *535*, 401–405.

[232] J. Xavier, S. Vincent, F. Meder, F. Vollmer, *Nanophotonics: in press* **2017**.

[233] A. Gopinath, D. G. Kirkpatrick, P. W. Rothemund, C. Thachuk in Canadian Conference on Computational Geometry, **2016**, pp. 230–236.

[234] S. Zou, G. C. Schatz, *Chemical Physics Letters* **2005**, *403*, 62–67.

[235] S. Toroghi, P. G. Kik, *Physical Review B* **2012**, *85*, 045432.

[236] E. Almpanis, N. Papanikolaou, B. Auguie, C. Tserkezis, N. Stefanou, *Optics Letters* **2012**, *37*, 4624–4626.

[237] H. Bui, C. Onodera, C. Kidwell, Y. Tan, E. Graugnard, W. Kuang, J. Lee, W. B. Knowlton, B. Yurke, W. L. Hughes, *Nano Letters* **2010**, *10*, 3367–3372.

A. Appendix

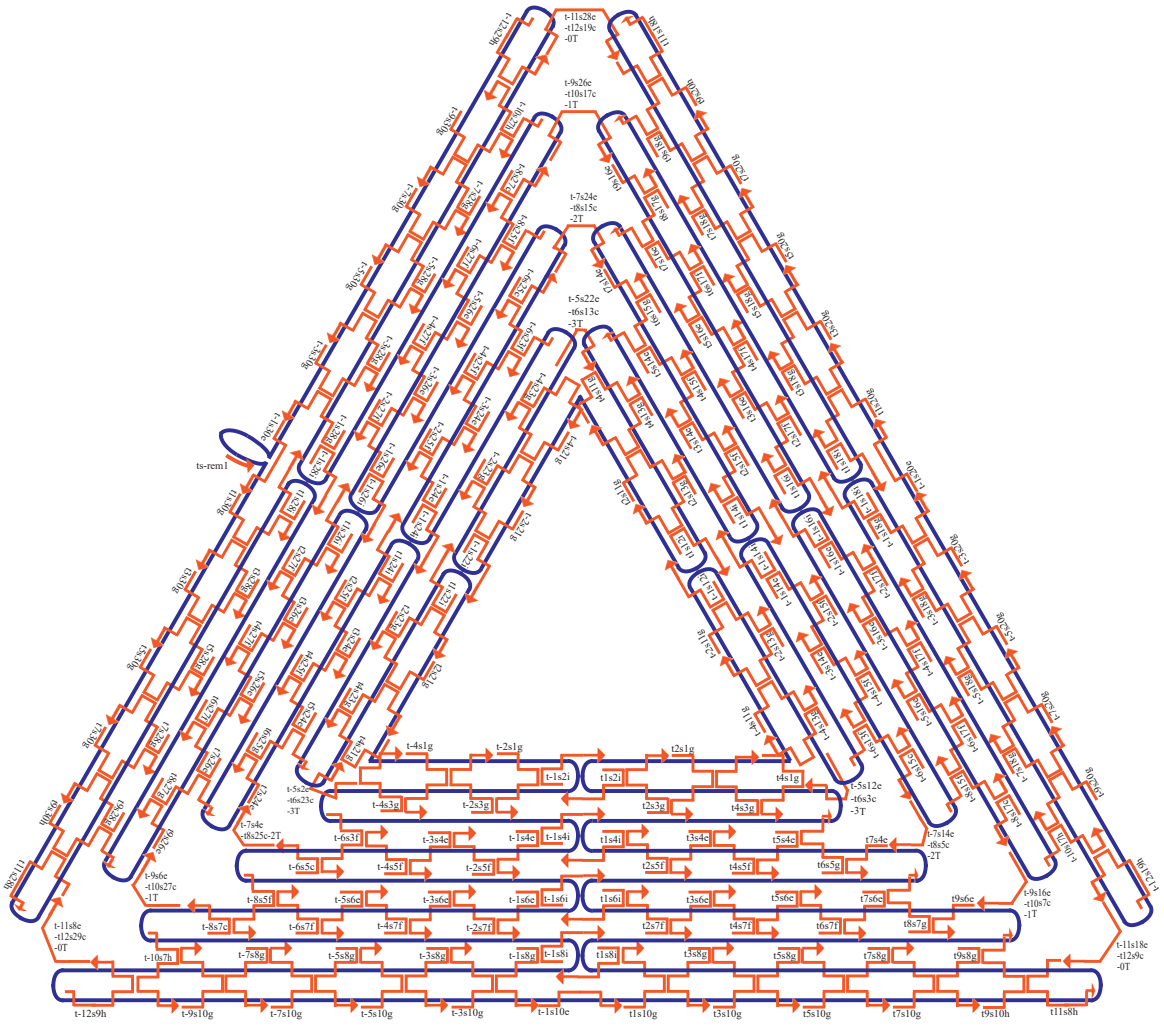

Figure A.1.: Map of the DNA origami scaffold. Staple strands: red, scaffold strand: blue. The original version of this graphic was created by Alexandru Rotaru.

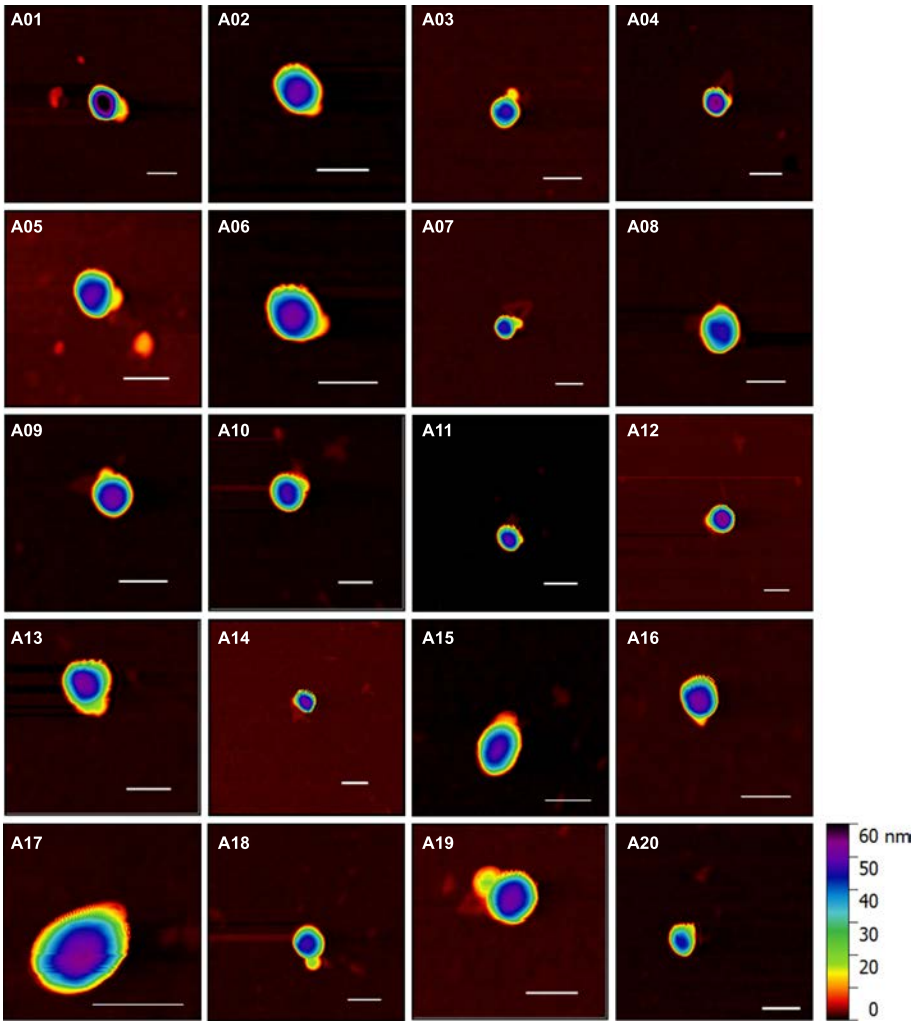

Figure A.2.: AFM images of the single 20-10*-60 gold nanolenses used for the nanolens design comparison. Scale bars: 100 nm.

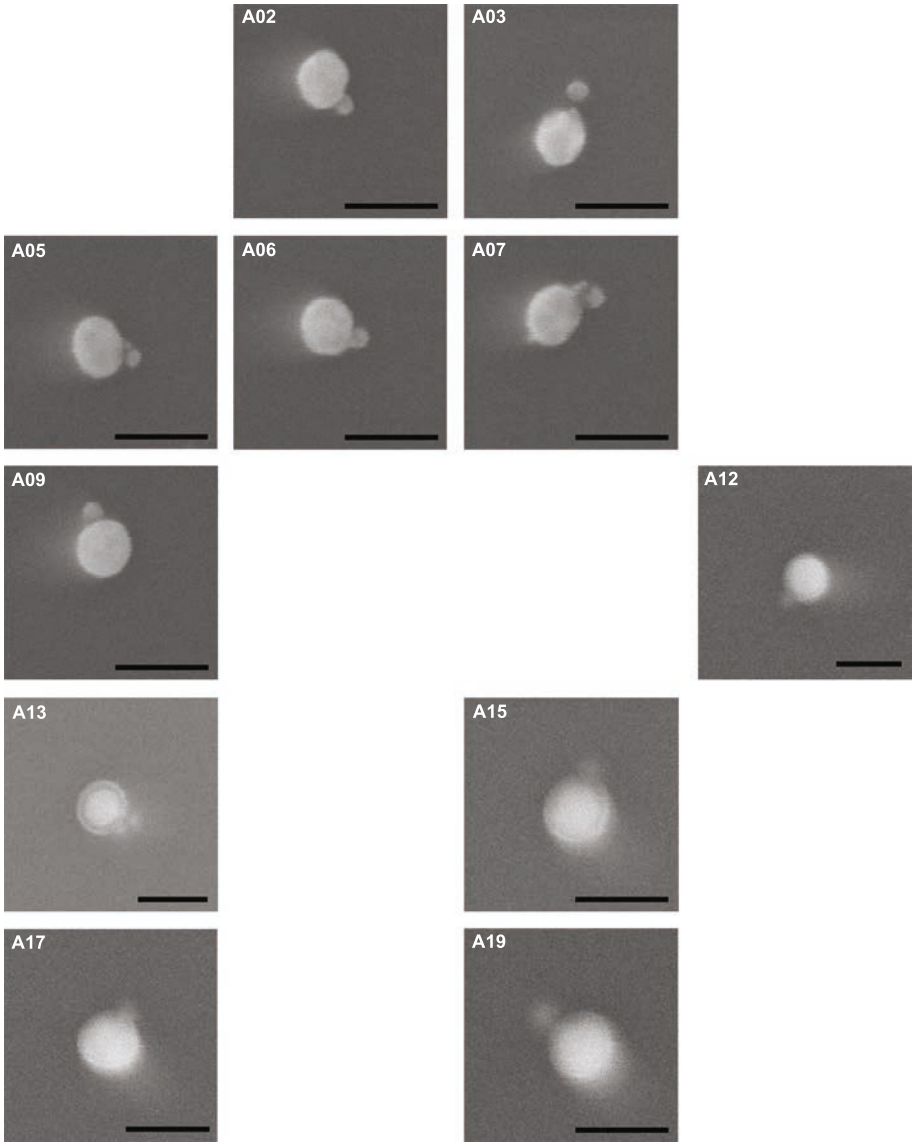

Figure A.3.: SEM images of the single 20-10*-60 gold nanolenses used for the nanolens design comparison. The numbering corresponds to the one in the AFM images of Figure A.2. Scale bars: 100 nm. Since the scratches on the silicon substrates had a very low contrast when imaging with low magnification, it was not possible to find the all gold nanolenses of the set displayed in Figure A.2.

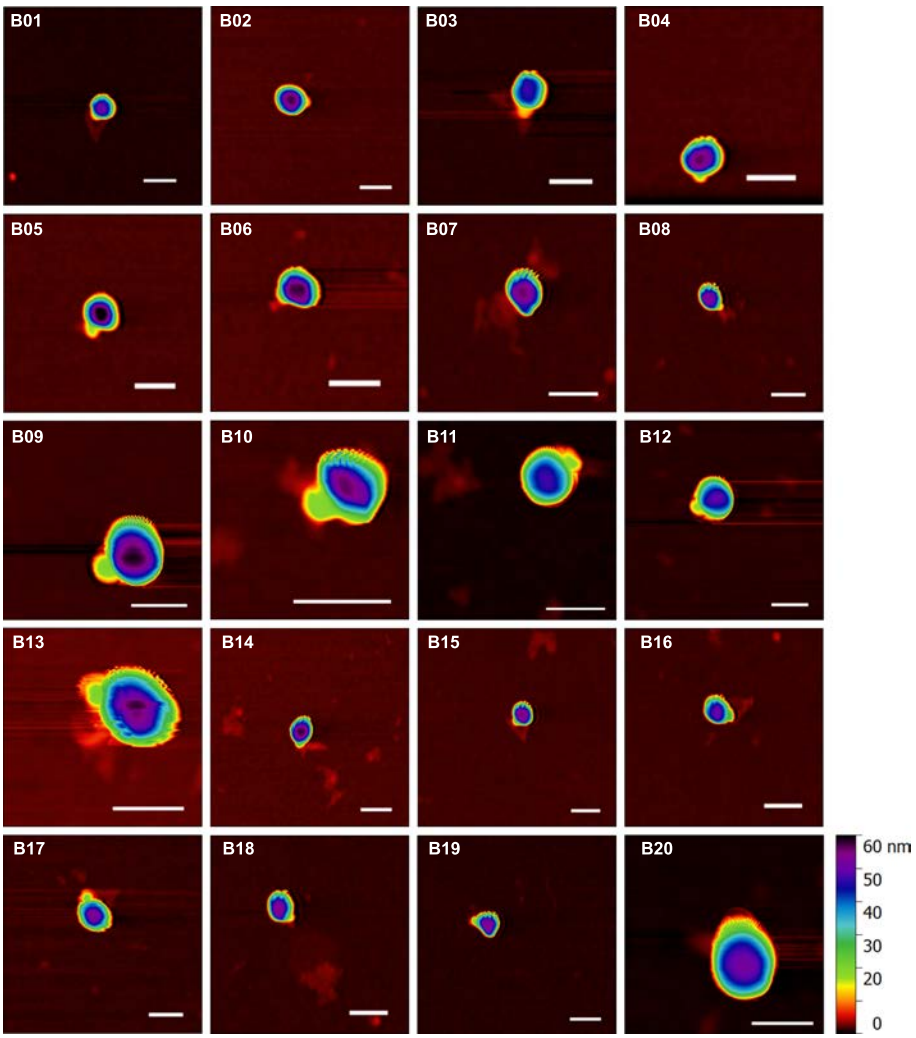

Figure A.4.: AFM images of the single 20_b-10*-60 gold nanolenses used for the nanolens design comparison. Scale bars: 100 nm.

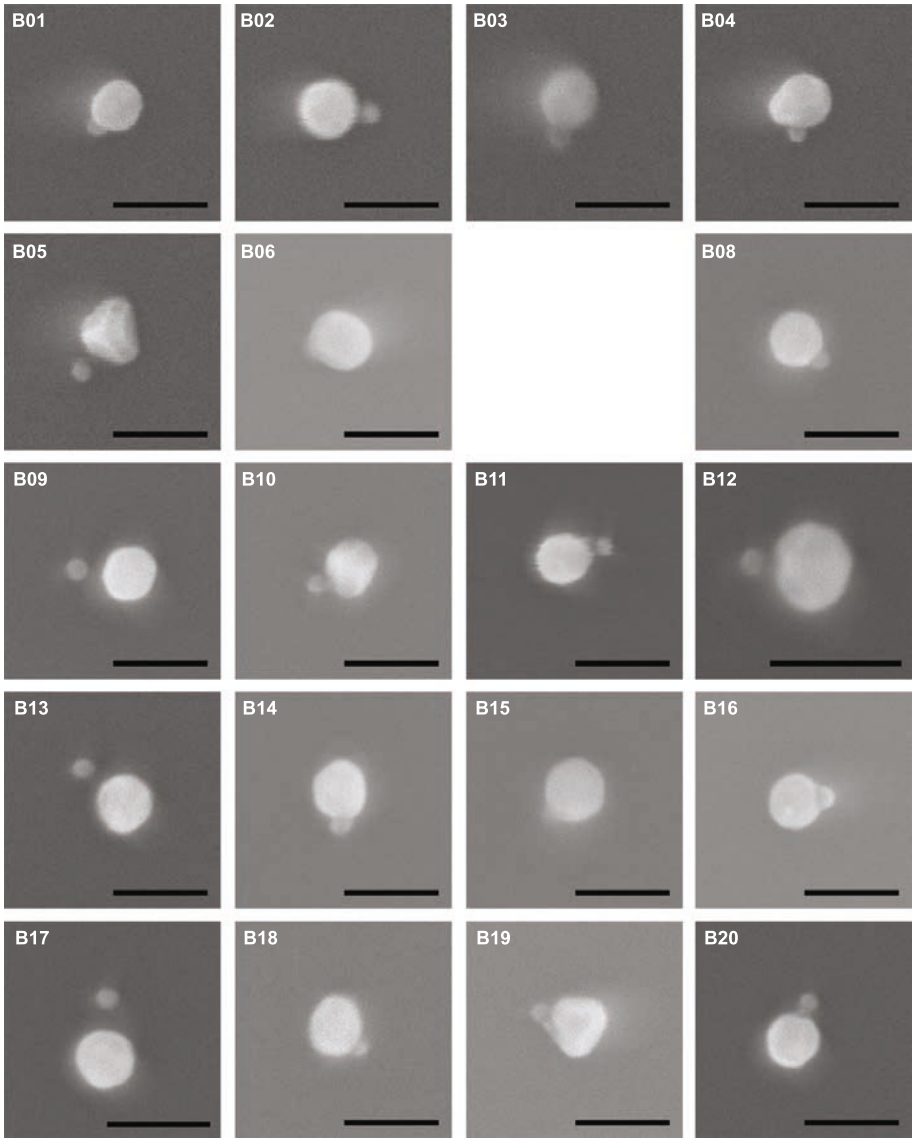

Figure A.5.: SEM images of the single 20_b-10*-60 gold nanolenses used for the nanolens design comparison. The numbering corresponds to the one in the AFM images of Figure A.4. Scale bars: 100 nm. Since the scratches on the silicon substrates had a very low contrast when imaging with low magnification, it was not possible to find the all gold nanolenses of the set displayed in Figure A.4.

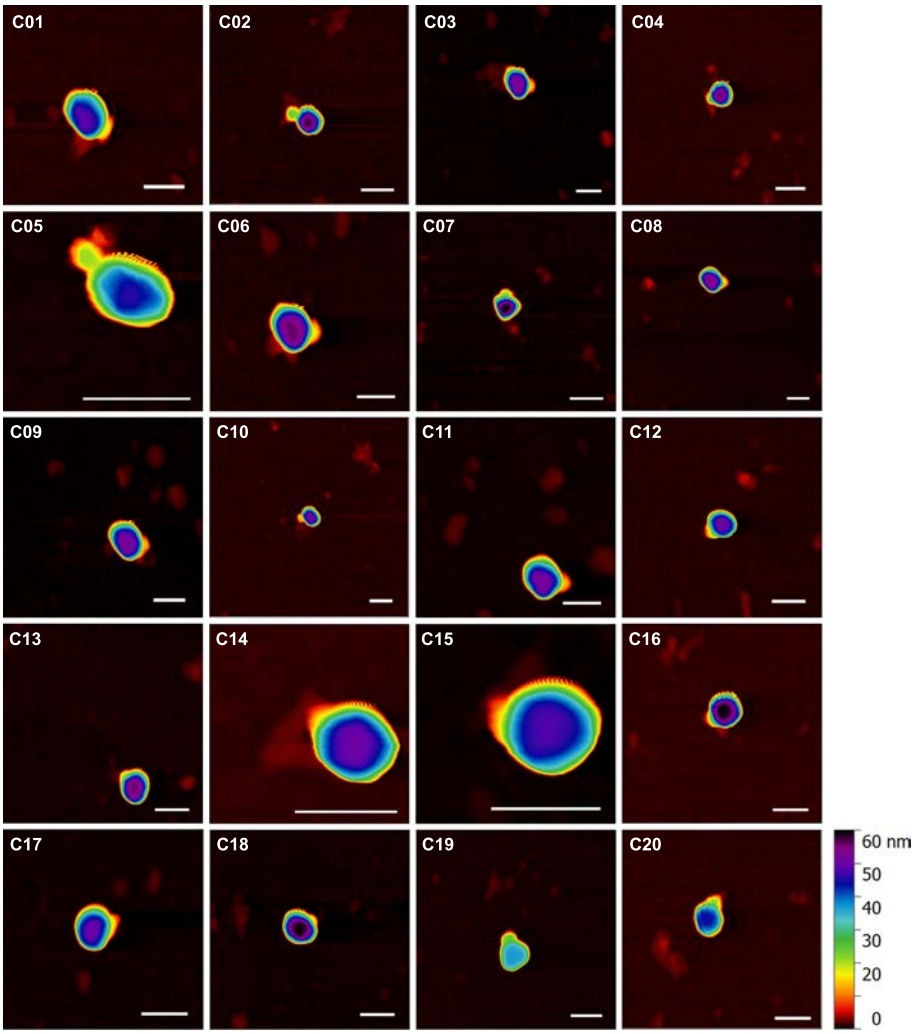

Figure A.6.: AFM images of the single 10*-20-60 gold nanolenses used for the nanolens design comparison. Scale bars: 100 nm.

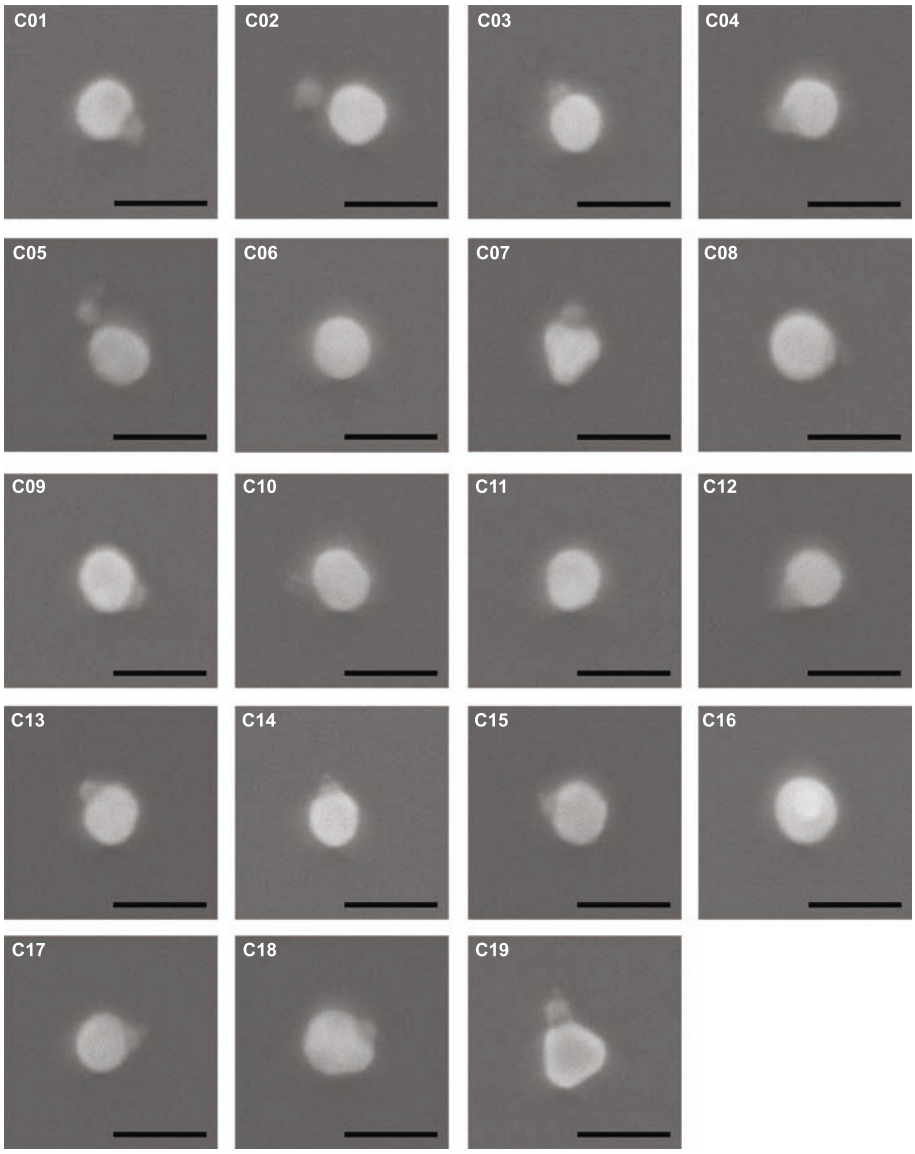

Figure A.7.: SEM images of the single 10*-20-60 gold nanolenses used for the nanolens design comparison. The numbering corresponds to the one in the AFM images of Figure A.6. Scale bars: 100 nm. Since the scratches on the silicon substrates had a very low contrast when imaging with low magnification, it was not possible to find the all gold nanolenses of the set displayed in Figure A.6.

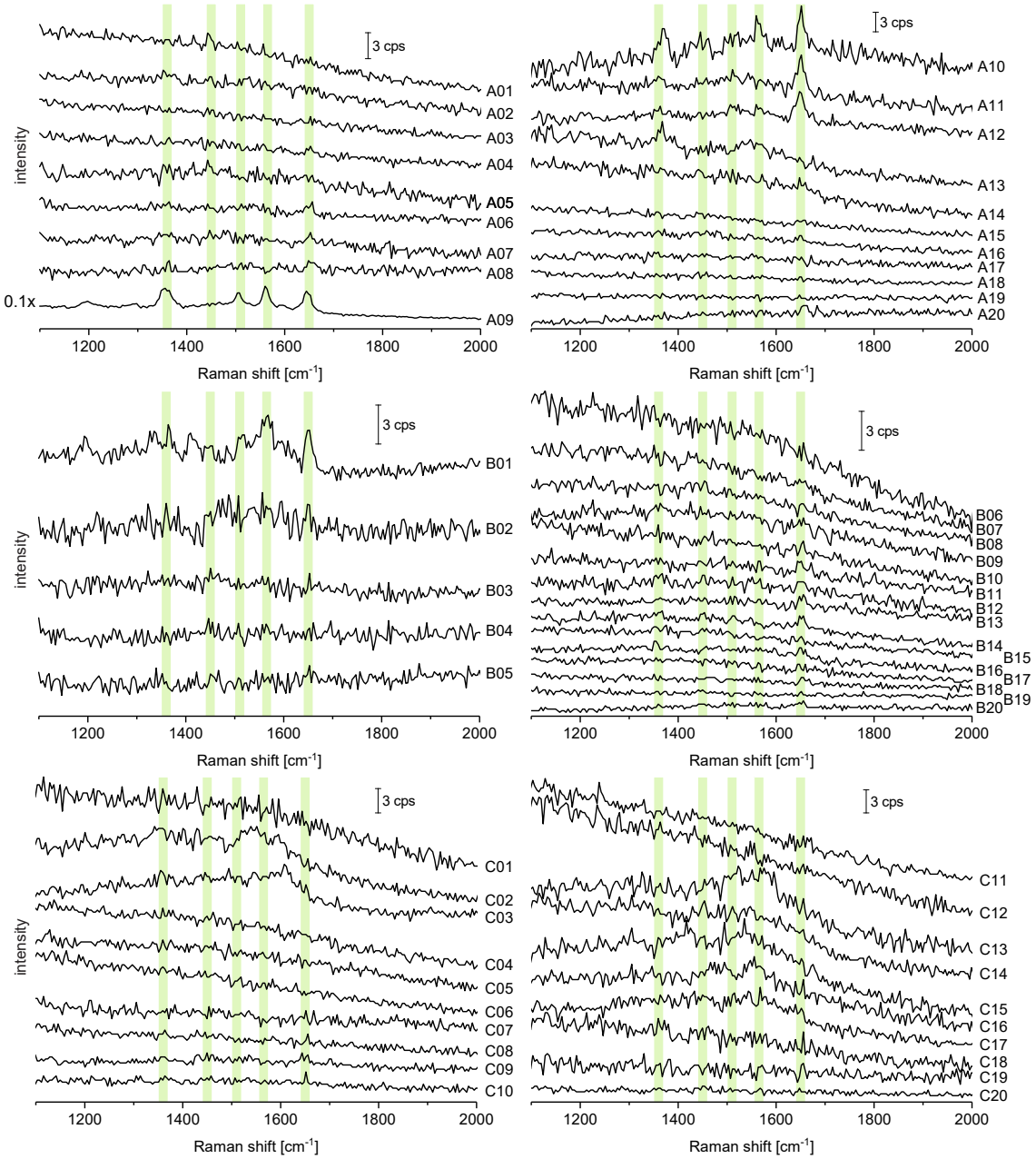

Figure A.8.: SERS spectra obtained from 20-10*-60 (A01–A20), 20_b-10*-60 (B01–B20) and 10*-20-60 (C01–C20) gold nanolenses. Characteristic TAMRA bands are marked in green. The numbering corresponds to the one used for the AFM and SEM images in Figures A.2 – A.7. Measured with the 100x objective, 4 s integration and 0.4 mW at the sample, offset for clarity. Spectrum A09 was scaled down by a factor of 10.

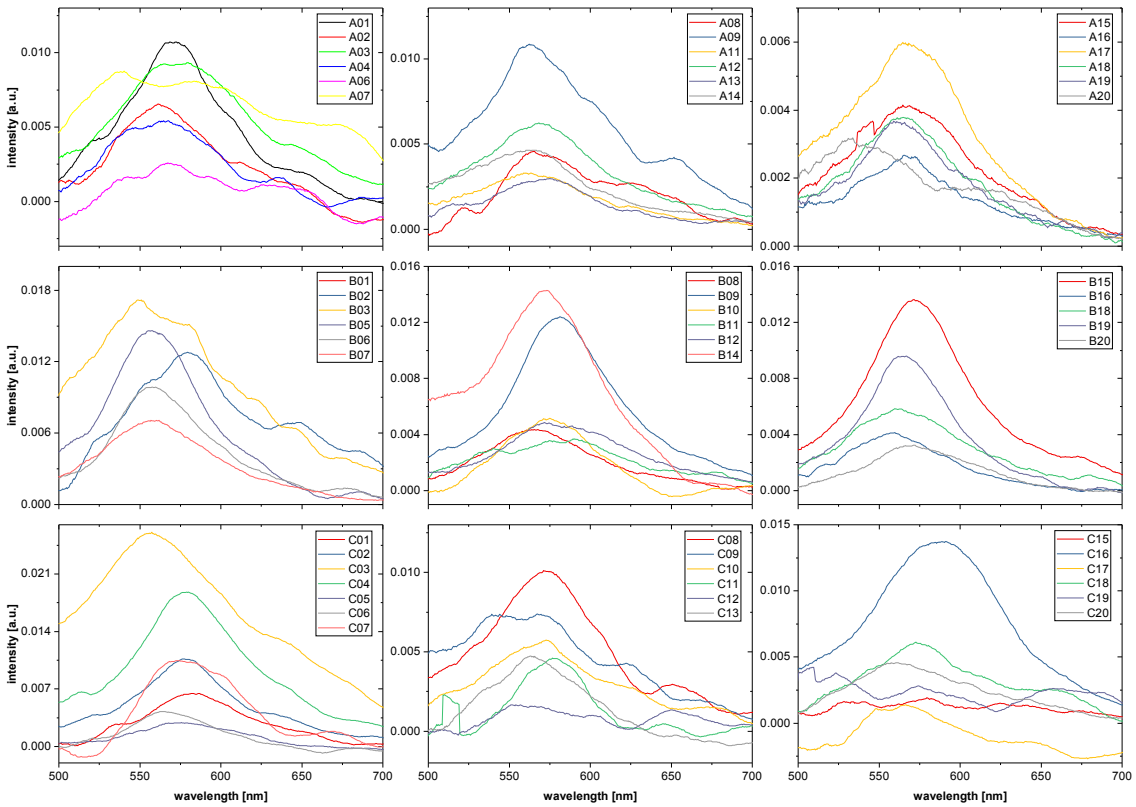

Figure A.9.: Dark field scattering spectra obtained from 20-10*-60 (A01–A20), 20_b-10*-60 (B01–B20) and 10*-20-60 (C01–C20) gold nanolenses. The numbering corresponds to the ones in Figures A.2 – A.8. For a few nanolenses, spectra are distorted or no clear spectra could be obtained due to background scattering on the sample. These were excluded from the λ_{max} analysis.

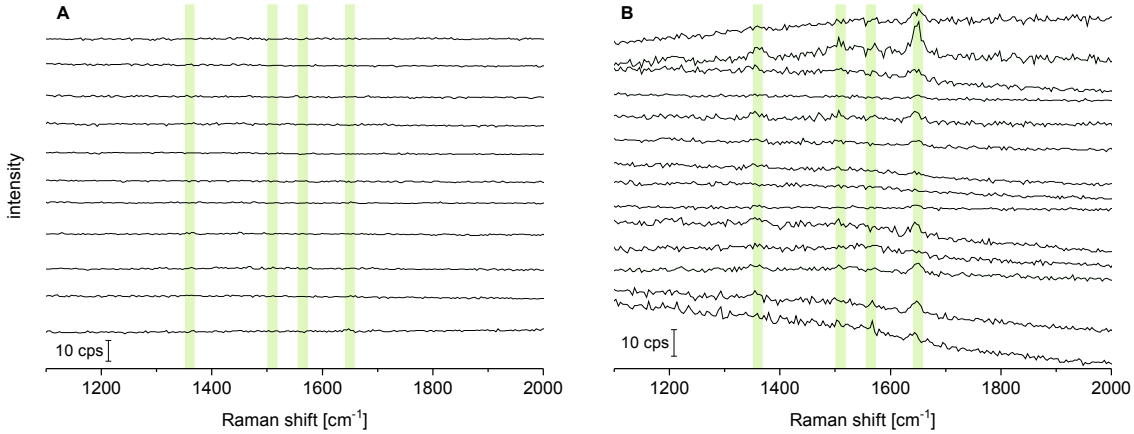

Figure A.10.: SERS spectra obtained from (A) single 20 nm and (B) single 60 nm gold particles coated with TAMRA-modified DNA strands and used for correcting the data from the gap comparison as well as for calculating enhancement factors (60 nm particles). Characteristic TAMRA bands are marked in green. Measured with the 100x objective, 4 s integration and 0.4 mW at the sample, offset for clarity.

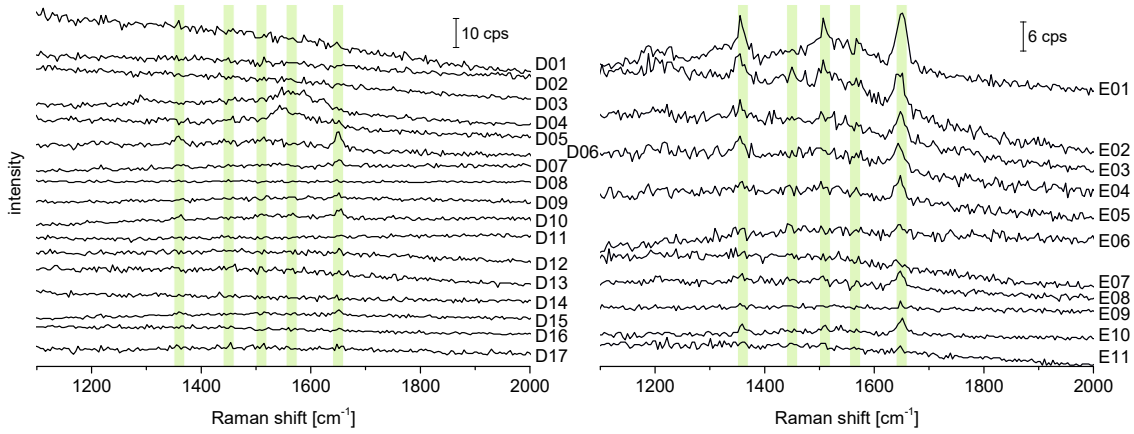

Figure A.11.: SERS spectra from single gold nanolenses where either the 20 nm gold nanoparticle (D01–D17, 20*-10-60), or the 60 nm gold nanoparticle (E01–E11, 20-10-60*) carried TAMRA-modified DNA strands. The numbering corresponds to the one in the AFM images of Figure A.12. These spectra were used to compare the signal intensities from the two different internal gaps. Characteristic TAMRA bands are marked in green. Measured with the 100x objective, 4 s integration and 0.4 mW at the sample, offset for clarity.

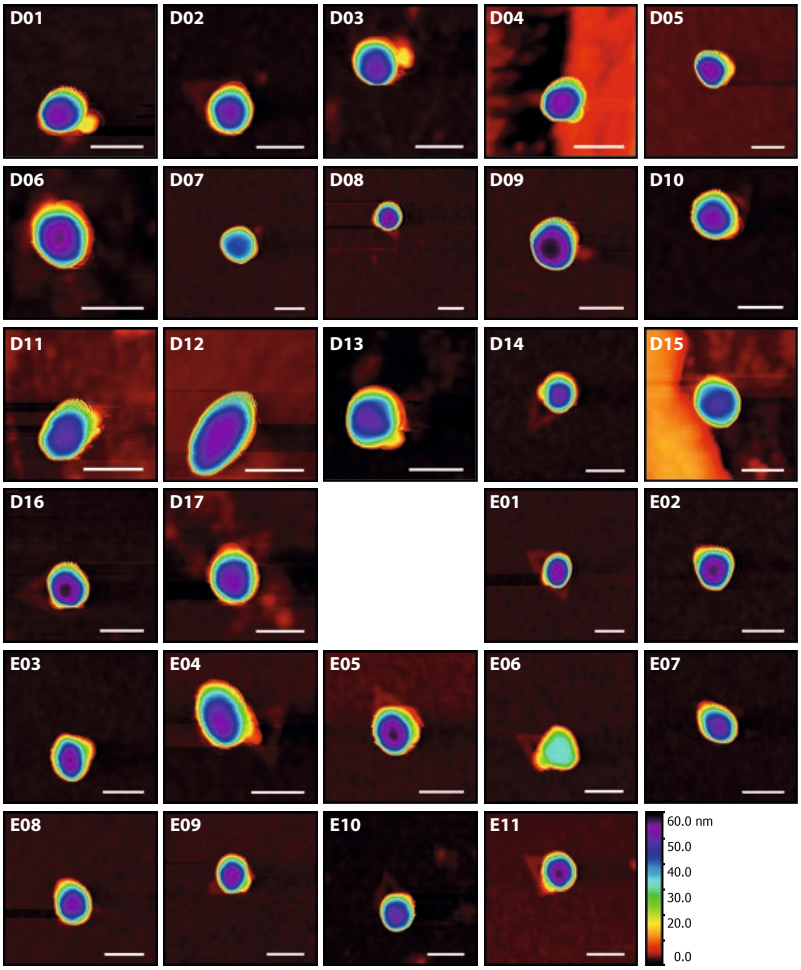

Figure A.12.: AFM images of the single 20*-10-60 gold nanolenses (D01–D17) and 20-10-60* gold nanolenses (E01–E11) used for the gap comparison. Scale bars: 100 nm.

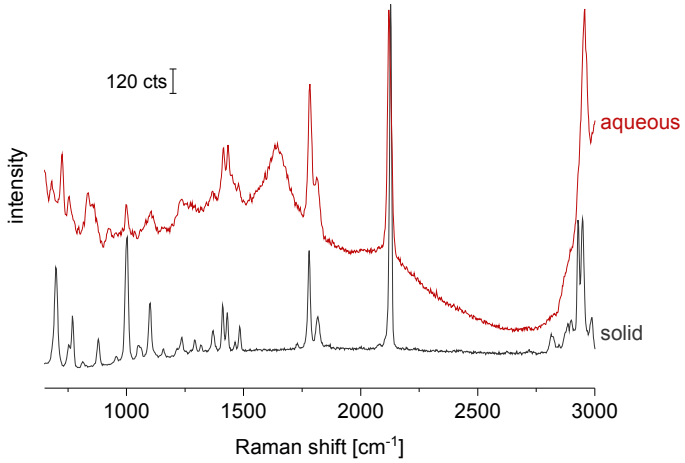

Figure A.13.: Raman spectra of P-NHS, solid and with 125 mM in water, obtained with the 10x objective and 24 mW at the sample. (solid) 0.5 s integration, 10 accumulations. (aqueous) 10 s integration, 40 accumulations. A drop of 10 µl of the liquid sample was placed and measured on a silicon wafer. Spectra offset for clarity.

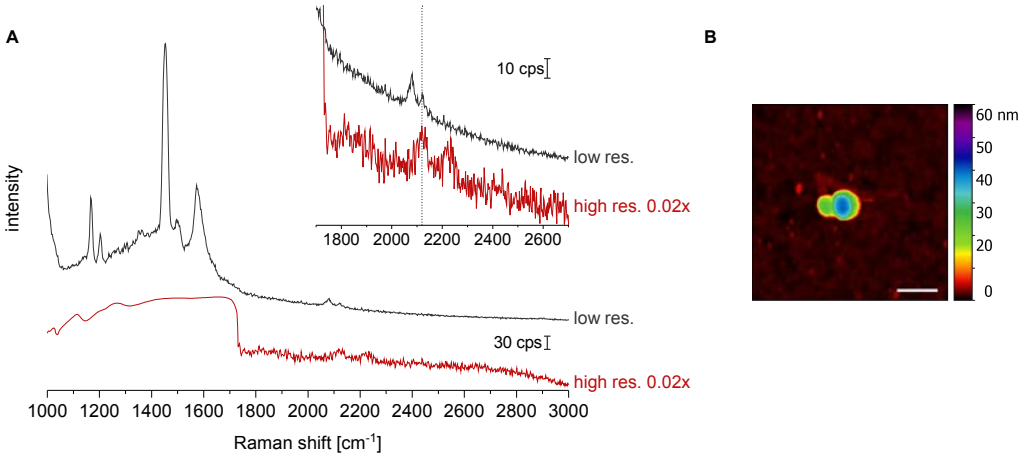

Figure A.14.: (A) SERS spectra from silver nanolenses with streptavidin, same position on a silicon wafer. Low resolution: 10x objective, 24 mW, 8 s integration, conventional camera. High resolution: 100x objective, 0.4 mW, 4 s integration, EMCCD camera, scaled down by 0.02, detector oversaturated below 1750 cm^{-1}. The high resolution spectrum originates from a single silver nanolens. The inset is a zoom-in onto the alkyne peak at 2120 cm^{-1} (dotted line). Spectra offset for clarity. (B) AFM image of the corresponding silver nanolens.

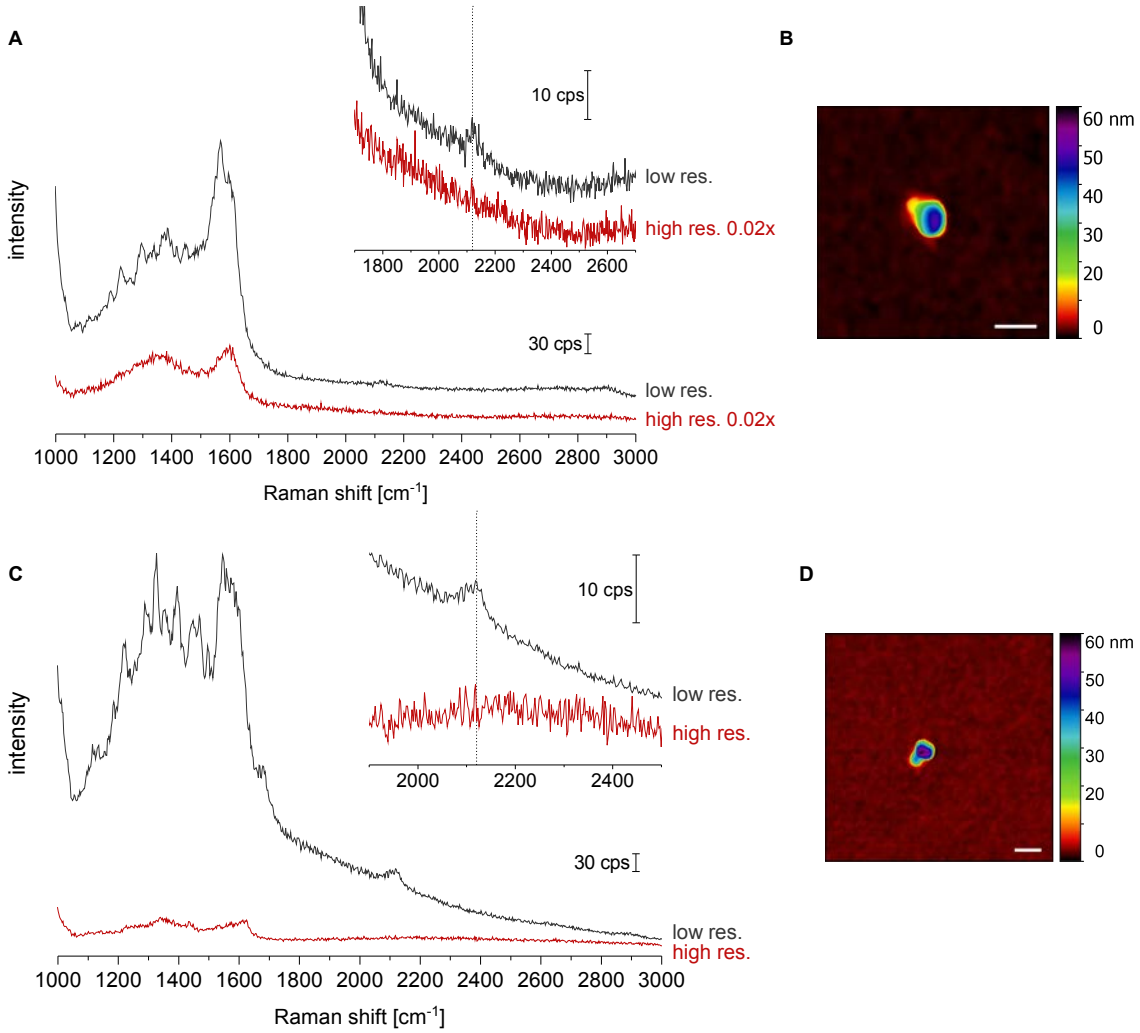

Figure A.15.: (A/C) SERS spectra from silver nanolenses with streptavidin, same positions on a silicon wafer.
Low resolution: 10x objective, 24 mW, 8 s integration, conventional camera. High resolution: 100x objective, 0.4 mW, single silver nanolenses, (A) 2 s integration, EMCCD camera, scaled down by 0.02, (C) 4 s integration, conventional camera. Spectra offset for clarity. The insets zoom onto the alkyne peak at 2120 cm^{-1} (dotted line).
(B/D) AFM images of the corresponding single silver nanolenses. Scale bars: 100 nm.

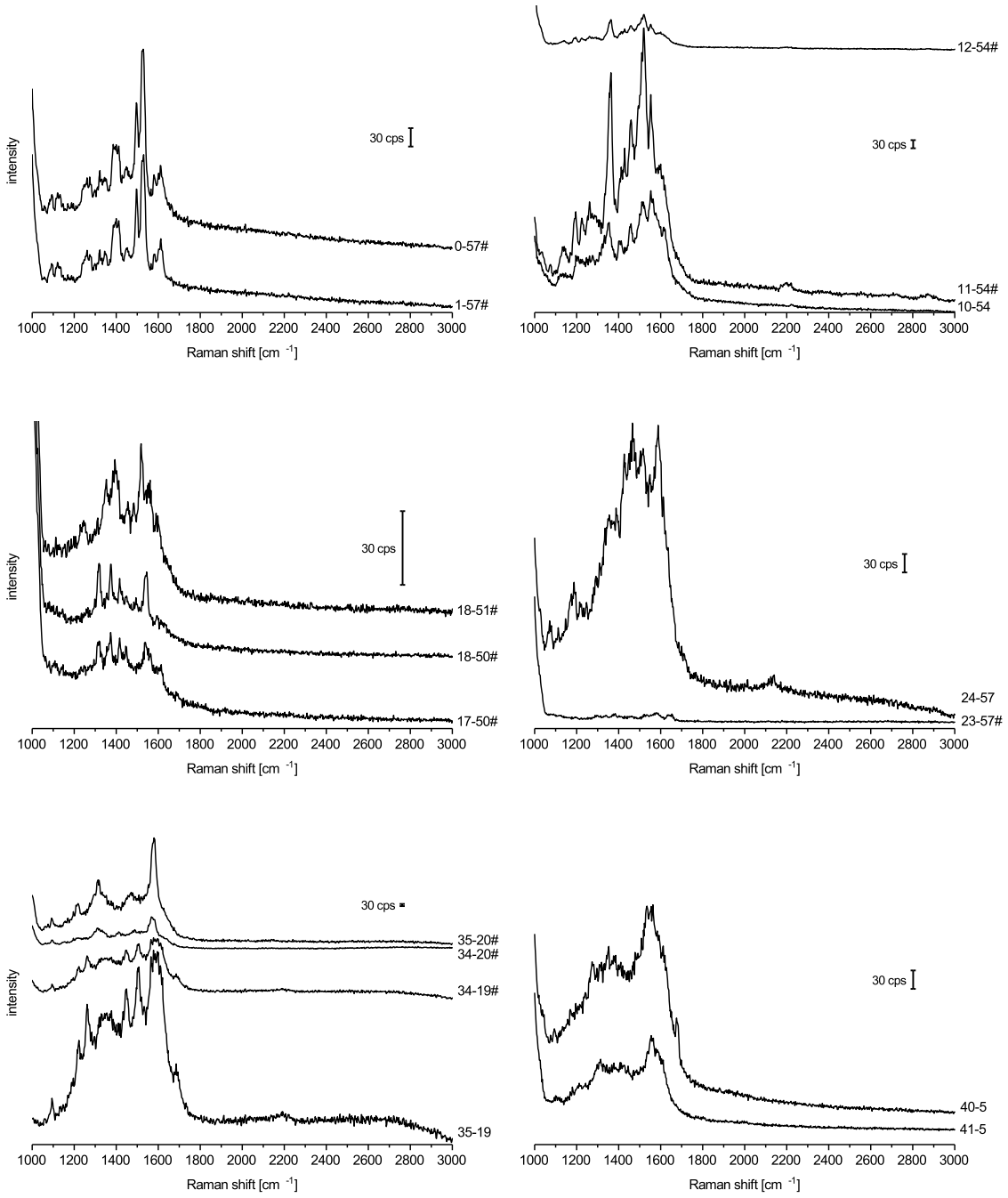

Figure A.16.: Each diagram shows SERS spectra from a certain single silver nanolens with streptavidin, measured at different positions during the Raman scan. The respective coordinates are annotated on the right, with the first-measured spectrum at the bottom and the last-measured at the top. Obtained with the 100x objective, 4 s integration and **2.8 mW** at the sample. Spectra are offset for clarity.

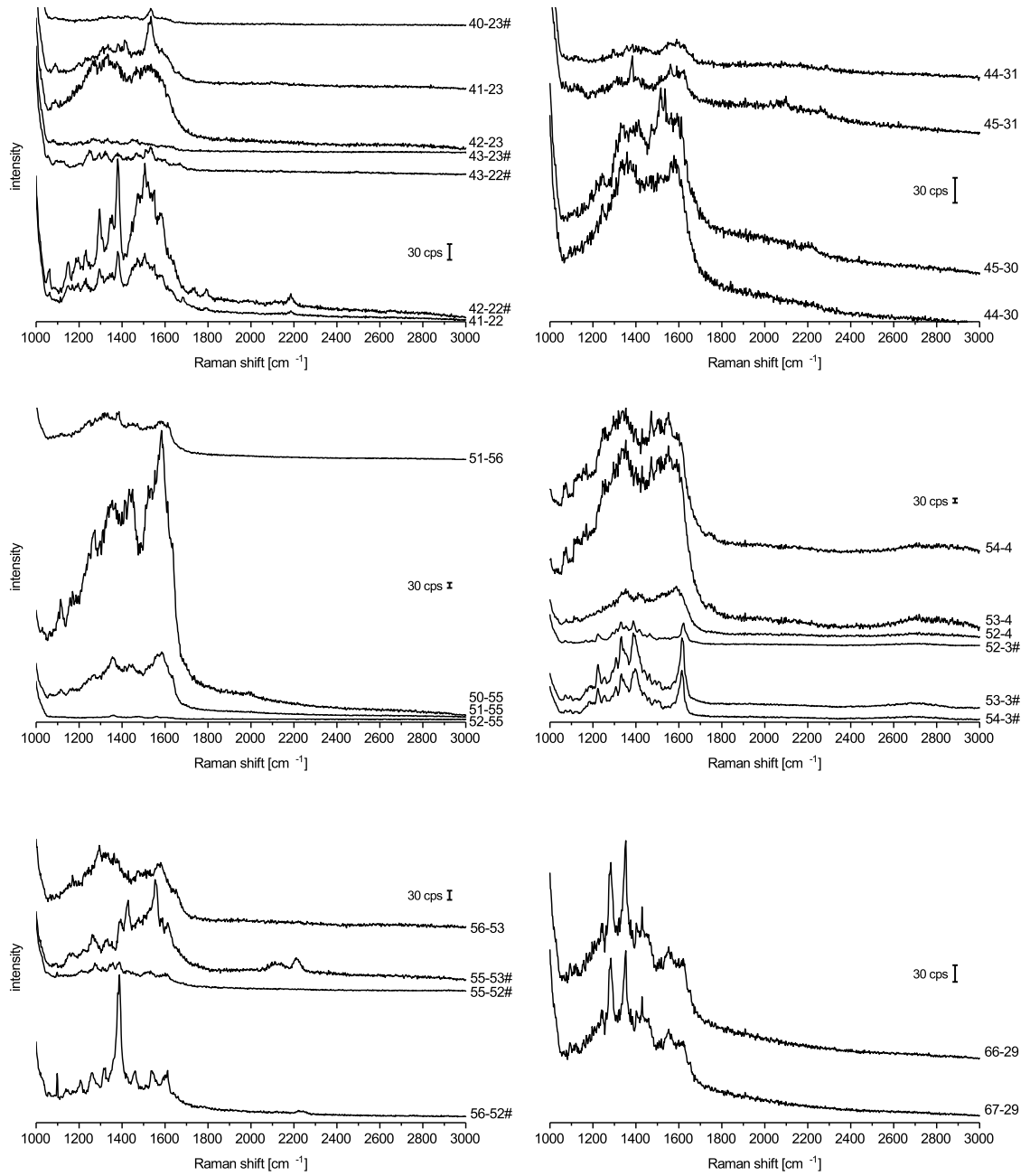

Figure A.17.: Each diagram shows SERS spectra from a certain single silver nanolens with streptavidin, measured at different positions during the Raman scan. The respective coordinates are annotated on the right, with the first-measured spectrum at the bottom and the last-measured at the top. Obtained with the 100x objective, 4 s integration and **2.8 mW** at the sample. Spectra are offset for clarity.

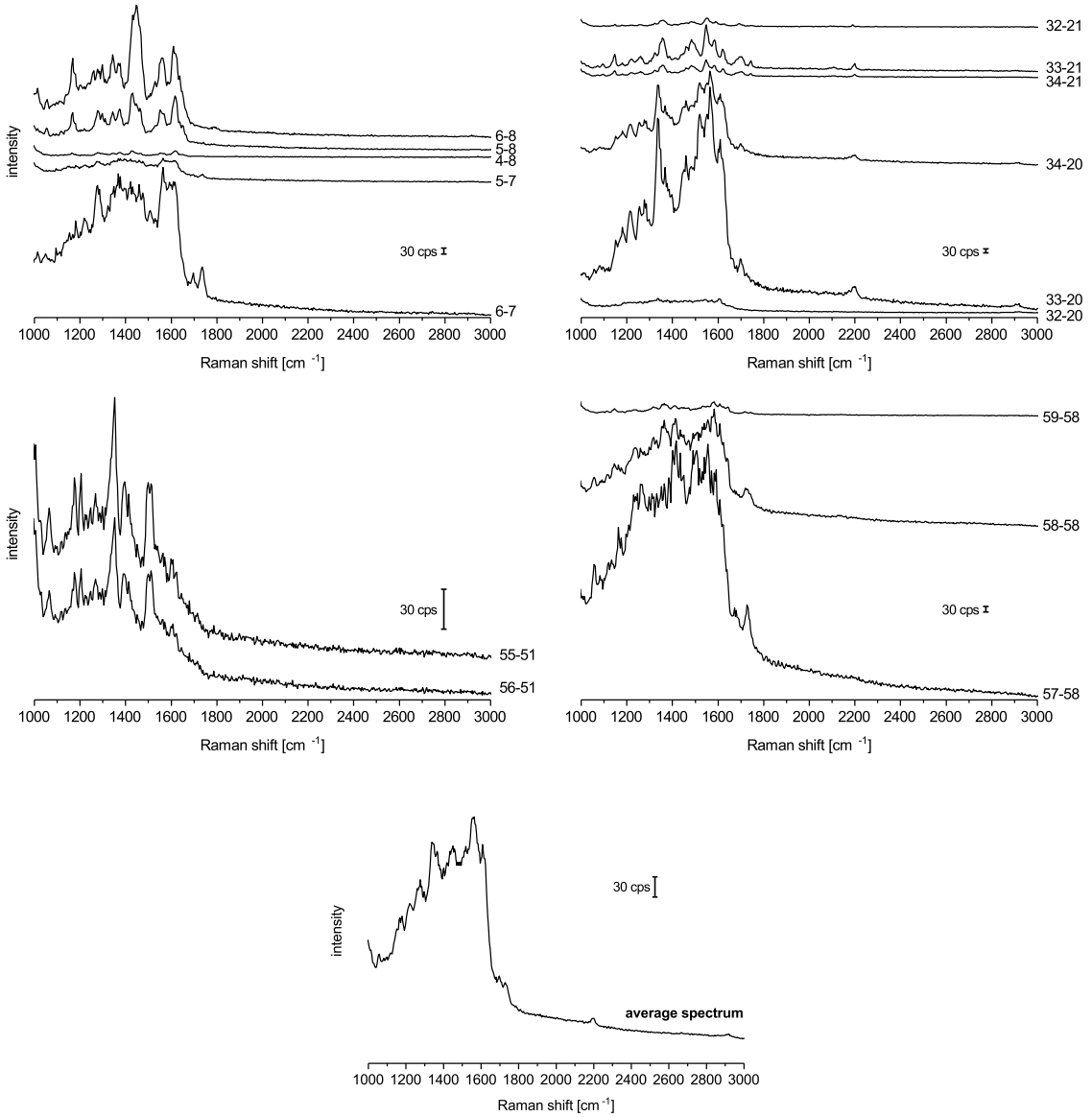

Figure A.18.: Each diagram shows SERS spectra from a certain single silver nanolens with streptavidin, measured at different positions during the Raman scan. The respective coordinates are annotated on the right, with the first-measured spectrum at the bottom and the last-measured at the top. Obtained with the 100x objective, 4 s integration and **0.4 mW** at the sample. Spectra are offset for clarity. The bottom diagram shows the average of the four upper diagrams.

Table A.1.: Staple strand set used for assembly of the DNA origami scaffold. Strands eventually modified in certain designs are given in bold.

t8s27g	CGCGAACTAAAACAGAGGTGAGGCTTAGAAGTATT
t8s7g	AGCCATTTAAACGTCACCAATGAACACCAGAACCA
t9s10h	TATCTTACCGAAGCCCAAACGCAATAATAACGAAAATCACCAG
t9s16e	ACTAAAGTACGGTGTCGAATATAA
t9s18g	TGCTGTAGATCCCCCTCAAATGCTGCGAGAGGCTTTTGCA
t9s20h	AAAGAAGTTTTGCCAGCATAAATATTCATTGACTCAACATGTT
t9s26e	ACCACCAGCAGAAGATGATAGCCC
t9s28g	TAAAACATTAGAAGAACTCAAACTTTTTATAATCAGTGAG
t9s30h	GCCACCGAGTAAAAGAACATCACTTGCCTGAGCGCCATTAAAA
t9s6e	CCATTAGCAAGGCCGGGGGAATTA
t9s8g	GAGCCAGCGAATACCCAAAAGAACATGAAATAGCAATAGC
t-10s17h	ACCAACCTAAAAAATCAACGTAACAAATAAATTGGGCTTGAGA
t-10s27h	AACTCACATTATTGAGTGTTGTTCCAGAAACCGTCTATCAGGG
t-10s7h	ACGACAATAAATCCCGACTTGCGGGAGATCCTGAATCTTACCA
t-12s19h	CCTGACGAGAAACACCAGAACGAGTAGGCTGCTCATTCAGTGA
t-12s29h	ACGTGGACTCCAACGTCAAAGGGCGAATTTGGAACAAGAGTCC
t-12s9h	TGCTATTTTGCACCCAGCTACAATTTTGTTTTGAAGCCTTAAA
t-1s10e	AGAGAATAACATAAAAACAGGGAAGCGCATTA
t-1s12i	AGGGATAGCTCAGAGCCACCACCCCATGTCAA
t-1s14e	ATTTTCTGTCAGCGGAGTGAGAATACCGATAT
t-1s14i	CAACAGTTTATGGGATTTTGCTAATCAAAAGG
t-1s16e	ATTCGGTCTGCGGGATCGTCACCCGAAATCCG
t-1s16i	GCCGCTTTGCTGAGGCTTGCAGGGGAAAAGGT
t-1s18g	CGACCTGCGGTCAATCATAAGGGAACGGAACAACATTATT
t-1s18i	GCGCAGACTCCATGTTACTTAGCCCGTTTTAA
t-1s20e	ACAGGTAGAAAGATTCATCAGTTGAGATTTAG
t-1s22i	CGCGTCTGATAGGAACGCCATCAACTTTTACA
t-1s24e	CAGTTTGACGCACTCCAGCCAGCTAAACGACG
t-1s24i	AGGAAGATGGGGACGACGACAGTAATCATATT
t-1s26e	GCCAGTGCGATCCCCGGGTACCGAGTTTTTCT
t-1s26i	CTCTAGAGCAAGCTTGCATGCCTGGTCAGTTG
t-1s28g	TTTCACCAGCCTGGCCCTGAGAGAAAGCCGGCGAACGTGG
t-1s28i	CCTTCACCGTGAGACGGGCAACAGCAGTCACA
t-1s2i	CCTTTTTTCATTTAACAATTTCATAGGATTAG
t-1s30e	CGAGAAAGGAAGGGAAGCGTACTATGGTTGCT
t-1s4e	TTATCAAACCGGCTTAGGTTGGGTAAGCCTGT
t-1s4i	TTTAACCTATCATAGGTCTGAGAGTTCCAGTA
t-1s6e	TTAGTATCGCCAACGCTCAACAGTCGGCTGTC
t-1s6i	AGTATAAAATATGCGTTATACAAAGCCATCTT
t-1s8g	TTTCCTTAGCACTCATCGAGAACAATAGCAGCCTTTACAG
t-1s8i	CAAGTACCTCATTCCAAGAACGGGAAATTCAT
t-2s11g	CCTCAGAACCGCCACCCAAGCCCAATAGGAACGTAAATGA
t-2s13g	AGACGTTACCATGTACCGTAACACCCCTCAGAACCGCCAC
t-2s15f	CACGCATAAGAAAGGAACAACTAAGTCTTTCC
t-2s17f	ATTGTGTCTCAGCAGCGAAAGACACCATCGCC
t-2s1g	AAAACAAAATTAATTAAATGGAAACAGTACATTAGTGAAT
t-2s21g	GCTCATTTTTTAACCAGCCTTCCTGTAGCCAGGCATCTGC
t-2s23g	GTAACCGTCTTTCATCAACATTAAAATTTTTGTTAAATCA

t-2s25f	ACGTTGTATTCCGGCACCGCTTCTGGCGCATC
t-2s27f	CCAGGGTGGCTCGAATTCGTAATCCAGTCACG
t-2s3g	AGAGTCAAAAATCAATATATGTGATGAAACAAACATCAAG
t-2s5f	ACTAGAAATATATAACTATATGTACGCTGAGA
t-2s7f	TCAATAATAGGGCTTAATTGAGAATCATAATT
t-3s10g	AACGTCAAAAATGAAAAGCAAGCCGTTTTTATGAAACCAA
t-3s14e	GTTTTGTCAGGAATTGCGAATAATCCGACAAT
t-3s16e	GACAACAAGCATCGGAACGAGGGTGAGATTTG
t-3s18g	TATCATCGTTGAAAGAGGACAGATGGAAGAAAAATCTACG
t-3s20g	TTAATAAAACGAACTAACCGAACTGACCAACTCCTGATAA
t-3s24e	TGTAGATGGGTGCCGGAAACCAGGAACGCCAG
t-3s26e	GGTTTTCCATGGTCATAGCTGTTTGAGAGGCG
t-3s28g	GTTTGCGTCACGCTGGTTTGCCCCAAGGGAGCCCCCGATT
t-3s30g	TAGAGCTTGACGGGGAGTTGCAGCAAGCGGTCATTGGGCG
t-3s4e	GATTAAGAAATGCTGATGCAAATCAGAATAAA
t-3s6e	CACCGGAATCGCCATATTTAACAAAATTTACG
t-3s8g	AGCATGTATTTCATCGTAGGAATCAAACGATTTTTTGTTT
t-4s11g	AGGTTTAGTACCGCCATGAGTTTCGTCACCAGGATCTAAA
t-4s13g	AGCGTAACTACAAACTACAACGCCTATCACCGTACTCAGG
t-4s15f	TAGTTGCGAATTTTTTCACGTTGATCATAGTT
t-4s17f	GTACAACGAGCAACGGCTACAGAGGATACCGA
t-4s1g	GAGCAAAAGAAGATGAGTGAATAACCTTGCTTATAGCTTA
t-4s21g	GTTAAAATTCGCATTAATGTGAGCGAGTAACACACGTTGG
t-4s23g	GGATAGGTACCCGTCGGATTCTCCTAAACGTTAATATTTT
t-4s25f	AGTTGGGTCAAAGCGCCATTCGCCCCGTAATG
t-4s27f	CGCGCGGGCCTGTGTGAAATTGTTGGCGATTA
t-4s3g	ACATAGCGCTGTAAATCGTCGCTATTCATTTCAATTACCT
t-4s5f	GTTAAATACAATCGCAAGACAAAGCCTTGAAA
t-4s7f	CCCATCCTCGCCAACATGTAATTTAATAAGGC
t-5s10g	TCCCAATCCAAATAAGATTACCGCGCCCAATAAATAATAT
t-5s16e	AACAGCTTGCTTTGAGGACTAAAGCGATTATA
t-5s18g	CCAAGCGCAGGCGCATAGGCTGGCAGAACTGGCTCATTAT
t-5s20g	ACCAGTCAGGACGTTGGAACGGTGTACAGACCGAAACAAA
t-5s26e	TGCTGCAAATCCGCTCACAATTCCCAGCTGCA
t-5s28g	TTAATGAAGTTTGATGGTGGTTCCGAGGTGCCGTAAAGCA
t-5s30g	CTAAATCGGAACCCTAAGCAGGCGAAAATCCTTCGGCCAA
t-5s6e	GTGTGATAAGGCAGAGGCATTTTCAGTCCTGA
t-5s8g	ACAAGAAAGCAAGCAAATCAGATAACAGCCATATTATTTA
t-6s13f	ACAGACAGCCCAAATCTCCAAAAAAAAATTTCTTA
t-6s15c	CGAGGTGAGGCTCCAAAAGGAGCC
t-6s17f	ACCCCCAGACTTTTTCATGAGGAACTTGCTTT
t-6s23f	CGGCGGATTGAATTCAGGCTGCGCAACGGGGGATG
t-6s25c	TGGCGAAATGTTGGGAAGGGCGAT
t-6s27f	TGTCGTGCACACAACATACGAGCCACGCCAGC
t-6s3f	TCCCTTAGAATAACGCGAGAAAACTTTTACCGACC
t-6s5c	GTTTGAAATTCAAATATATTTTAG
t-6s7f	AATAGATAGAGCCAGTAATAAGAGATTTAATG
t-7s10g	GCCAGTTACAAAATAATAGAAGGCTTATCCGGTTATCAAC
t-7s18g	AAAACACTTAATCTTGACAAGAACTTAATCATTGTGAATT
t-7s20g	ACCTTATGCGATTTTATGACCTTCATCAAGAGCATCTTTG
t-7s28g	TTCCAGTCCTTATAAATCAAAAGAGAACCATCACCCAAAT

t-7s30g	CAAGTTTTTTGGGGTCGAAATCGGCAAAATCCGGGAAACC
t-7s8g	GCGCCTGTTATTCTAAGAACGCGATTCCAGAGCCTAATTT
t-8s15f	CGGTTTATCAGGTTTCCATTAAACGGGAATACACT
t-8s17c	GGCAAAAGTAAAATACGTAATGCC
t-8s25f	TCTTCGCTATTGGAAGCATAAAGTGTATGCCCGCT
t-8s27c	GCGCTCACAAGCCTGGGGTGCCTA
t-8s5f	TTCTGACCTAAAATATAAAGTACCGACTGCAGAAC
t-8s7c	TCAGCTAAAAAAGGTAAAGTAATT
t-9s10g	ACGCTAACGAGCGTCTGGCGTTTTAGCGAACCCAACATGT
t-9s20g	TGGTTTAATTTCAACTCGGATATTCATTACCCACGAAAGA
t-9s30g	CGATGGCCCACTACGTATAGCCCGAGATAGGGATTGCGTT
ts-rem1	GCGCTTAATGCGCCGCTACAGGGC
t-5s2e-t6s23c-3T	TTAATTAATTTTTTACCATATCAAA
t-7s4e-t8s25c-2T	TTAATTTCATCTTAGACTTTACAA
t-9s6e-t10s27c-1T	CTGTCCAGACGTATACCGAACGA
t-11s8e-t12s29c-0T	TCAAGATTAGTGTAGCAATACT
t-5s12e-t6s3c-3T	TGTAGCATTCCTTTTATAAACAGTT
t-7s14e-t8s5c-2T	TTTAATTGTATTTCCACCAGAGCC
t-9s16e-t10s7c-1T	ACTACGAAGGCTTAGCACCATTA
t-11s18e-t12s9c-0T	ATAAGGCTTGCAACAAAGTTAC
t-5s22e-t6s13c-3T	GTGGGAACAAATTTCTATTTTTGAG
t-7s24e-t8s15c-2T	CGGTGCGGGCCTTCCAAAAACATT
t-9s26e-t10s17c-1T	ATGAGTGAGCTTTTAAATATGCA
t-11s28e-t12s19c-0T	ACTATTAAAGAGGATAGCGTCC
t11s18h	AATACTGCGGAATCGTAGGGGGTAATAGTAAAATGTTTAGACT
t11s28h	TCTTTGATTAGTAATAGTCTGTCCATCACGCAAATTAACCGTT
t11s8h	CAGAAGGAAACCGAGGTTTTTAAGAAAAGTAAGCAGATAGCCG
t1s10g	GACGGGAGAATTAACTCGGAATAAGTTTATTTCCAGCGCC
t1s12i	TCATATGTGTAATCGTAAAACTAGTCATTTTC
t1s14i	GTGAGAAAATGTGTAGGTAAAGATACAACTTT
t1s16i	GGCATCAAATTTGGGGCGCGAGCTAGTTAAAG
t1s18i	TTCGAGCTAAGACTTCAAATATCGGGAACGAG
t1s20g	GAATACCACATTCAACTTAAGAGGAAGCCCGATCAAAGCG
t1s22i	TCGGGAGATATACAGTAACAGTACAAATAATT
t1s24i	CCTGATTAAAGGAGCGGAATTATCTCGGCCTC
t1s26i	GCAAATCACCTCAATCAATATCTGCAGGTCGA
t1s28i	CGACCAGTACATTGGCAGATTCACCTGATTGC
t1s2i	CGGGGTTTCCTCAAGAGAAGGATTTTGAATTA
t1s30g	TTGACGAGCACGTATACTGAAATGGATTATTTAATAAAAG
t1s4i	AGCGTCATGTCTCTGAATTTACCGACTACCTT
t1s6i	TTCATAATCCCCTTATTAGCGTTTTTCTTACC
t1s8i	ATGGTTTATGTCACAATCAATAGATATTAAAC
t2s11g	AGAAAAGCCCCAAAAAGAGTCTGGAGCAAACAATCACCAT
t2s13g	ACAGTCAAAGAGAATCGATGAACGACCCCGGTTGATAATC
t2s15f	ATAGTAGTATGCAATGCCTGAGTAGGCCGGAG
t2s17f	AACCAGACGTTTAGCTATATTTTCTTCTACTA
t2s1g	GATAAGTGCCGTCGAGCTGAAACATGAAAGTATACAGGAG
t2s21g	CCTGATTGCTTTGAATTGCGTAGATTTTCAGGCATCAATA
t2s23g	TGGCAATTTTTAACGTCAGATGAAAACAATAACGGATTC
t2s25f	AAGGAATTACAAAGAAACCACCAGTCAGATGA
t2s27f	GGACATTCACCTCAAATATCAAACACAGTTGA

t2s3g	TTTGATGATTAAGAGGCTGAGACTTGCTCAGTACCAGGCG
t2s5f	CCGGAACCCAGAATGGAAAGCGCAACATGGCT
t2s7f	AAAGACAACATTTTCGGTCATAGCCAAAATCA
t3s10g	GTCAGAGGGTAATTGATGGCAACATATAAAAGCGATTGAG
t3s14e	CAATATGACCCTCATATATTTTAAAGCATTAA
t3s16e	CATCCAATAAATGGTCAATAACCTCGGAAGCA
t3s18g	AACTCCAAGATTGCATCAAAAAGATAATGCAGATACATAA
t3s20g	CGCCAAAAGGAATTACAGTCAGAAGCAAAGCGCAGGTCAG
t3s24e	TAATCCTGATTATCATTTTGCGGAGAGGAAGG
t3s26e	TTATCTAAAGCATCACCTTGCTGATGGCCAAC
t3s28g	AGAGATAGTTTGACGCTCAATCGTACGTGCTTTCCTCGTT
t3s30g	AGAATCAGAGCGGGAGATGGAAATACCTACATAACCCTTC
t3s4e	TGTACTGGAAATCCTCATTAAAGCAGAGCCAC
t3s6e	CACCGGAAAGCGCGTTTTCATCGGAAGGGCGA
t3s8g	CATTCAACAAACGCAAAGACACCAGAACACCCTGAACAAA
t4s11g	GCAAATATTTAAATTGAGATCTACAAAGGCTACTGATAAA
t4s13g	CGTTCTAGTCAGGTCATTGCCTGACAGGAAGATTGTATAA
t4s15f	CAGGCAAGATAAAAATTTTTAGAATATTCAAC
t4s17f	GATTAGAGATTAGATACATTTCGCAAATCATA
t4s1g	TAGCCCGGAATAGGTGAATGCCCCCTGCCTATGGTCAGTG
t4s21g	GCGCAGAGGCGAATTAATTATTTGCACGTAAATTCTGAAT
t4s23g	GATTATACACAGAAATAAAGAAATACCAAGTTACAAAATC
t4s25f	TAGGAGCATAAAAGTTTGAGTAACATTGTTTG
t4s27f	TGACCTGACAAATGAAAAATCTAAAATATCTT
t4s3g	TTTAACGGTTCGGAACCTATTATTAGGGTTGATATAAGTA
t4s5f	CTCAGAGCATATTCACAAACAAATTAATAAGT
t4s7f	GGAGGGAATTTAGCGTCAGACTGTCCGCCTCC
t5s10g	GATAACCCACAAGAATGTTAGCAAACGTAGAAAATTATTC
t5s14e	TTAATGCCTTATTTCAACGCAAGGGCAAAGAA
t5s16e	TTAGCAAATAGATTTAGTTTGACCAGTACCTT
t5s18g	TAATTGCTTTACCCTGACTATTATGAGGCATAGTAAGAGC
t5s20g	AACACTATCATAACCCATCAAAAATCAGGTCTCCTTTTGA
t5s24e	AATGGAAGCGAACGTTATTAATTTCTAACAAC
t5s26e	TAATAGATCGCTGAGAGCCAGCAGAAGCGTAA
t5s28g	GAATACGTAACAGGAAAAACGCTCCTAAACAGGAGGCCGA
t5s30g	TTAAAGGGATTTTAGATACCGCCAGCCATTGCGGCACAGA
t5s4e	CCTTGAGTCAGACGATTGGCCTTGCGCCACCC
t5s6e	TCAGAACCCAGAATCAAGTTTGCCGGTAAATA
t5s8g	TTGACGGAAATACATACATAAAGGGCGCTAATATCAGAGA
t6s15g	ATAAAGCCTTTGCGGGAGAAGCCTGGAGAGGGTAG
t6s17f	TAAGAGGTCAATTCTGCGAACGAGATTAAGCA
t6s25g	TCAATAGATATTAAATCCTTTGCCGGTTAGAACCT
t6s27f	CAATATTTGCCTGCAACAGTGCCATAGAGCCG
t6s5g	CAGAGCCAGGAGGTTGAGGCAGGTAACAGTGCCCG
t6s7f	ATTAAAGGCCGTAATCAGTAGCGAGCCACCCT
t7s10g	ATAAGAGCAAGAAACATGGCATGATTAAGACTCCGACTTG
t7s14e	ATGACCCTGTAATACTTCAGAGCA
t7s16e	TAAAGCTATATAACAGTTGATTCCCATTTTTG
t7s18g	CGGATGGCACGAGAATGACCATAATCGTTTACCAGACGAC
t7s20g	GATAAAAACCAAAATATTAAACAGTTCAGAAATTAGAGCT
t7s24e	ACAATTCGACAACTCGTAATACAT

t7s26e	TTGAGGATGGTCAGTATTAACACCTTGAATGG
t7s28g	CTATTAGTATATCCAGAACAATATCAGGAACGGTACGCCA
t7s30g	GAATCCTGAGAAGTGTATCGGCCTTGCTGGTACTTTAATG
t7s4e	GCCGCCAGCATTGACACCACCCTC
t7s6e	AGAGCCGCACCATCGATAGCAGCATGAATTAT
t7s8g	CACCGTCACCTTATTACGCAGTATTGAGTTAAGCCCAATA
t8s17g	TAATTGCTTGGAAGTTTCATTCCAAATCGGTTGTA

Publications

– C. Heck, Y. Kanehira, J. Kneipp, I. Bald, "Single proteins placed within the SERS hot spots of self-assembled silver nanolenses" *Angewandte Chemie Int. Ed.* **2018**, *accepted*, doi: 10.1002/anie.201801748R1.
– C. Heck, J. Prinz, V. Merk, A. Dathe, O. Stranik, W. Fritzsche, J. Kneipp, I. Bald, "Gold nanolenses self-assembled by DNA origami" *ACS Photonics* **2017**, *4*, 1123–1130.
– J. Prinz, C. Heck, L. Ellerik, V. Merk, I. Bald, "DNA origami based Au–Ag-core–shell nanoparticle dimers with single-molecule SERS sensitivity" *Nanoscale* **2016**, *8*, 5612–5620.
– C. Heck, Y. Kanehira, J. Kneipp, I. Bald, "Amorphous carbon generation in DNA origami-based plasmonic nanostructures" *in preparation.*

Talks

– Falling Walls Lab Finale, Berlin, November 2017.
– BioNanoPhotonics workshop, Tel Aviv University (Israel), March 2017.

Poster presentations

– C. Heck, J. Kneipp, I. Bald, "Single silver nanolenses that provide intense SERS spectra", Faraday Discussions: Surface-Enhanced Raman Scattering, Glasgow (UK), August 2017.
– C. Heck, J. Kneipp, I. Bald, "Gold and silver nanolenses", Future Trends in DNA-based Nanotechnology, Dresden, May 2017.
– C. Heck, J. Prinz, V. Merk, J. Kneipp, I. Bald, "Self-assembled gold nanolenses for surface-enhanced Raman scattering", Functional DNA Nanotechnology, Rome (Italy), June 2016.
– C. Heck, J. Prinz, V. Merk, J. Kneipp, I. Bald, "Gold nanolenses self-assembled by DNA origami for surface-enhanced Raman scattering", DNA Nanotechnology, Jena, May 2016.
– C. Heck, J. Prinz, V. Merk, J. Kneipp, I. Bald, "Gold nanolenses on DNA origami substrates for surface-enhanced Raman scattering", DNA Nanotechnology meets

Plasmonics, Bad Honnef, December 2015.
– C. Heck, J. Prinz, V. Merk, J. Kneipp, I. Bald, "Gold nanolenses on DNA origami substrates for surface-enhanced Raman scattering", International Conference on DNA Computing and Molecular Programming, Cambridge (USA), August 2015.
– C. Heck, J. Prinz, V. Merk, J. Kneipp, I. Bald, "Gold nanolenses on DNA origami substrates for surface-enhanced Raman scattering", Molecular Plasmonics, Jena, May 2015.
– C. Heck, J. Prinz, V. Merk, J. Kneipp, I. Bald, "Gold nanolenses on DNA origami substrates for surface-enhanced Raman scattering", International Conference on Raman Spectroscopy, Jena, August 2014.
– C. Heck, J. Prinz, V. Merk, J. Kneipp, I. Bald, "Gold nanolenses for surface-enhanced Raman scattering on DNA origami substrates", DNA-Based Nanotechnology: Digital Chemistry, Dresden, May 2014.
– J. Prinz*, C. Heck*, B. Schreiber, L. Olejko, J. Oertel, A. Keller, V. Merk, J. Kneipp, I. Bald, "DNA origami structures for highly sensitive surface-enhanced Raman scattering", Bunsentagung, Hamburg, May 2014. *Both authors contributed equally to this work.

Acknowledgements

Zunächst möchte ich Prof. Dr. Ilko Bald für die ausgezeichnete Betreuung und die tolle Forschungsumgebung danken. Ebenso bin ich Prof. Dr. Janina Kneipp, meiner Zweitbetreuerin, dankbar für die vielen anregenden Diskussionen und die Möglichkeit, Lumerical zu nutzen. Prof. Dr. Ralf Seidel danke ich für die Begutachtung der Arbeit. Dr. Julia Prinz verdanke ich die Bestimmung der Laserpunktgröße und viele andere Tipps im Umgang mit dem Raman-Mikroskop. Ohne Youngeun Choi, Steffi Vogel und Dr. Lydia Olejko hätte die Arbeit bei Weitem nicht so viel Freude gemacht. Robin Schürmann gilt mein Dank für spannende Diskussionen, insbesondere für den Hinweis auf Tris-Messungen in Lösung. Timm Schwaar and Ioana Abbas von der BAM möchte ich für die schnellen und unkomplizierten MALDI-Messungen danken. Dunkelfeld- und SEM-Messungen sind am IPHT Jena durchgeführt worden. Dafür möchte ich André Dathe, Dr. Ondra Stranik, Franka Jahn und Dr. Wolfgang Fritzsche danken. Dr. Alexandru Rotaru verdanke ich die ursprüngliche Version des schematischen Bauplans für das dreieckige DNA-Origami. Dr. Virginia Merk gilt mein Dank für die Einführung in Lumerical, Niclas S. Müller für Hilfe bei der Optimierung der Einstellungen. Yuya Kanehira möchte ich herzlich danken für den Einsatz und die vielen, während seines dreimonatigen Praktikums sauber durchgeführten Raman- und AFM-Messungen. Anna Stock danke ich fürs Korrekturlesen und viele Lieder.

Die Finanzierung dieser Forschungsarbeit erfolgte durch das DFG-Projekt GSC 1013 (SALSA), einen Marie Curie FP7 Integration Grant im Rahmen des siebten EU-Rahmenprogramms, den ERC Grant 259432 (MULTIBIOPHOT), EFRE-Mittel, die Universität of Potsdam und die Bundesanstalt für Materialforschung und -prüfung (BAM).

Erklärung

Hiermit versichere ich, dass ich die vorliegende Arbeit selbst verfasst und keine anderen Quellen und Hilfsmittel als die hier angegebenen verwendet habe. Ich versichere, dass diese Arbeit bisher nicht an anderer Stelle zur Erlangung des Doktorgrades eingereicht wurde.

Potsdam, Christian Heck